UNIVERSITETET I AGDER

Spectrogram Analysis of Non-Stationary RSE-to-Car Channels Behaviour for Braking Situations

BUDDIKA HERATH

SUPERVISOR
Prof. Matthias Pätzold

University of Agder, 2017
Faculty of Engineering and Science
Department of ICT

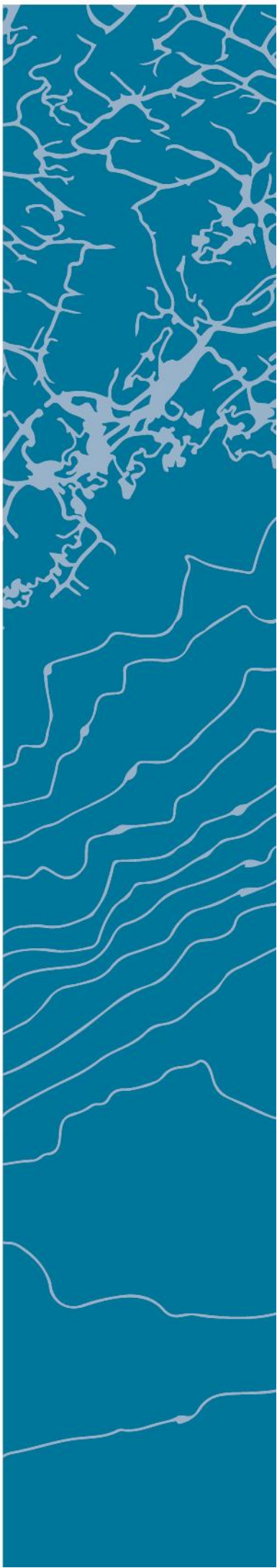

Spectrogram Analysis of Non-Stationary RSE-to-Car Channels Behaviour for Braking Situations

Buddika Herath

Spectrogram Analysis of Non-Stationary RSE-to-Car Channels Behaviour for Braking Situations

Masters Thesis for the Degree *Magister Scientiae (MSc)* in Information and Communication Technology

Supervised by Prof. Matthias Pätzold

University of Agder
Faculty of Engineering and Science
May 2017

Preface and Acknowledgements

This thesis is the result of the Master Thesis, IKT-590 to fulfil the requirements of course content of MSc ICT, at the Faculty of Engineering and Science, University of Agder (UiA) in Grimstad, Norway. The research work as been started from the second week of January 2017 and ended on 20 May 2017. The course contains 30 credits towards the degree of MSc ICT. This thesis is mainly focussed on analysing the mobile non-stationary channels for braking situations.

I would like to express my deepest gratitude to Prof. Matthias Pätzold of university of Agder, who in spite of being extraordinarily busy with his duties, took time out to hear, guide and keep me on the correct path during this research work.

Further, I express my deepest thanks to Mrs. Katharina Pätzold for taking time to help me on drafting and formatting the thesis. Her advices and guidance have substantially reduced my work load.

I would like to express my gratefulness to my parents, wife, son, and my friends for their support and blessings during the Master thesis.

Buddika Herath
University of Agder
Grimstad, Norway
21 May 2017

Abstract

Car-to-car (C2C) and car-to-infrastructure (C2I) communications promise revolutionary improvements in transportation due to its possibilities to improve the road safety and traffic management. C2C is a system designed to exchange information between vehicles, and C2I is a communication model that allows vehicles to share information with the infrastructure such as roadside equipment (RSE). These communications are considered as essential elements of the intelligent transport system (ITS). In this regard, reliability of the communication is vital to provide warning of an impending accident. Thus, the analysis of RSE-to-car channel behaviour is important and in this research work we use the concept of the spectrogram to estimate the local Doppler power spectral density (PSD) of the channel.

One of the standard assumptions of mobile radio channel modelling is that the speed of the mobile station (MS) is constant. However, in the real-world, mobile communication channels exhibit non-stationarity as the speed varies with the time. The non-stationary multipath fading channels can be modelled by a sum of SOC_h processes. If the speed is constant, the channel can be defined as a stationary channel consisting a sum of a SOC_i processes.

The Spectrogram provides an estimate of the changes to local Doppler power spectral density over time for the variations of the mobile speed. In this research work, we define the spectrogram using different window functions and show that the spectrogram can be split into an auto-term and a cross-term. The auto-term consists of relevant spectral information and the cross-term is considered as a sum of spectral interferences. Additionally, we investigate the spectrogram result optimisation by averaging over the phases and selecting an optimal window length. Furthermore, our study shows that the time-variant average Doppler shift, computed by taking the sum of all power-weighted Doppler shifts normalised to the total received power of the multipath components, is realisable by the estimated average time-variant Doppler shift computed from the spectrogram.

When the brakes are applied at a constant speed the channel's spectral characteristics convert from stationary to non-stationary state. We estimate the local Doppler PSD for braking situations and show the possibility of developing this model to detect road accidents.

keywords: auto-term, braking, cross-term, spectrogram, STFT, window function, window length, windowing

Contents

Acronyms

ACF	-	Auto Correlation Function
AOA	-	Angle of Arrival
AOM	-	Angle of Motion
C2C	-	Car-to-Car Communication
C2I	-	Car-to-Infrastructure Communication
CFO	-	Carrier Frequency Offset
EMEDS	-	Extended Method of Exact Doppler Spread
ERTICO	-	European Road Transport Telematics Implementation Co-ordination Org.
ETSI	-	European Telecommunications Standards Institute
FT	-	Fourier Transport
IEEE	-	Institute of Electrical and Electronics Engineers
ITS	-	Intelligent Transportation System
LOS	-	Line of Site
MIMO	-	Multi-Input Multi-Output
MS	-	Mobile Station
OFDM	-	Orthogonal Frequency Division Multiplexing
PSD	-	Power Spectral Density
RSE	-	Roadside Equipment
SNR	-	Signal-to-Noise Ratio
SOC_h	-	Sum-of-Chirps
SOC_i	-	Sum-of-Cisoids
STFT	-	Short-Time Fourier Transform
VII	-	Vehicle Infrastructure Integration
WLAN	-	Wireless Local Area Network

List of Tables

List of Figures

Chapter 1

Introduction

1.1 Overview of RSE-to-Car Communications

In the past few years, there has been an upsurge of research interest in car-to-car (C2C) and car-to-infrastructure (C2I) communications, which offer a variety of personalised services for passengers. In particular, traffic control and road safety applications are very comprehensive and reduce the number of traffic accidents as well as the fuel consumption. The Information provided by those applications are further improved by the inputs from internal systems such as collision avoidance, as well as external inputs, such as traffic warning information from the infrastructure. Hence, reliable communication between cars and car-to-infrastructure (C2I) is important to develop efficient safety and traffic control applications. Thus, it is important to evaluate the radio propagation channel condition in C2C communications especially in specific situations such as accelerating or braking the speed of a car.

Large numbers of research works on C2C communications are being carried out throughout the world and supported by industry-driven organisations such as C2C communication consortium (C2C-CC) [1]. Further, European Road Transport Telematics Implementation Coordination Organisation (ERTICO) is also involved in developing and promoting intelligent transport systems (ITS) and services in Europe [2]. The vehicle infrastructure integration (VII) is another joint government-industry effort which is focused on developing standardised C2C and C2I communications [3].

The recent allocation of dedicated standards IEEE 802.11P [4] and ETSI Intelligent Transportation Systems (ITS)-G5 [5], reflect the growing interest in C2C communication systems. IEEE 802.11P is based on the well-known wireless local area Network (WLAN) standard IEEE 802.11a and operate in the 5.9 GHz band.

Under the C2C and C2I concepts, vehicles would communicate with each other and with roadside transponders (or roadside equipment (RSE) in VII concept). It is widely accepted that in C2I communications, the RSE is fixed and the mobile station (MS) is in motion and equipped with antennas mostly at the same height. The buildings and trees can be considered as scatterers in RSE-to-car communications and cause multipath propagations as shown in Fig. 1.1.

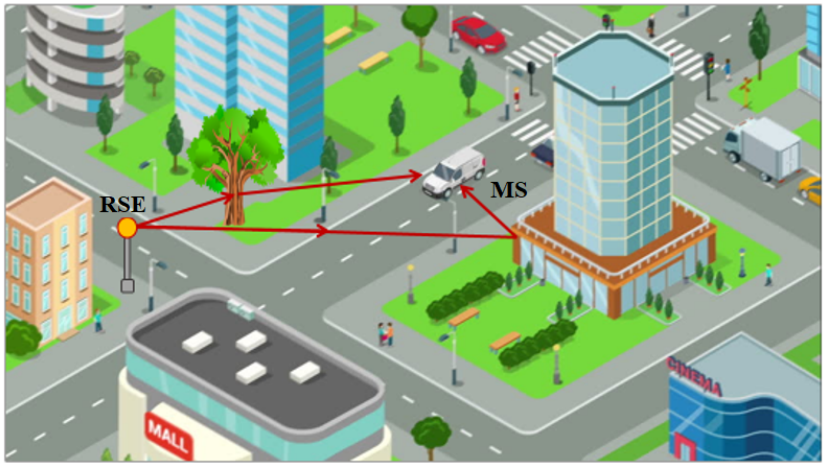

Figure 1.1: A typical RSE-to-car communication scenario.

1.2 Motivation

Over the last decade, many research works had been carried out in the areas of C2C and C2I communications. Consequently, non-stationary vehicular communication channel analysis has been acquiring considerable attention from the researchers and standardisation bodies.

In the literature [6–8], closed-form solutions were presented for the analysis of stationary and non-stationary channels using the concept of the spectrogram. The rectangle window function was used in [6] and [7] to define the spectrogram whilst Gaussian window function is used in [8]. However, there is a scarcity of literature on the definition of the spectrogram for stationary and non-stationary channel analysis using other well-known window types such as cosine windows. Motivated by the fact, we define the spectrogram using different window functions.

Braking is the most important safety feature of a vehicle. The communication channel exhibits non-stationarity when the brakes are applied. There are many good sources of literature which analyse the non-stationarity of the communication channels. The statistical channel models presented in [9–11] provide a comprehensive analysis of the non-stationary behaviour of the vehicular channels. Nevertheless, the mobile communication channel behaviour in braking situations are not adequately considered in the available literature. Therefore, we introduce the braking situation as a novel scenario for the analysis of non-stationary mobile radio channels. Thus, it is motivated to use the concept of the spectrogram for the analysis of non-stationary channels for braking situations, in which the study will be extended to select best window function for the spectrogram as well as to discuss the methods for improving the spectrogram.

1.3 Problem Statement

The spectrogram of a multipath fading channel should aim to improve the frequency and time resolution. The spectrogram can be defined using different types of window functions. Hence, the frequency and time resolution of the spectrogram will differ based on the window function. Therefore, it is important to select the best window function for a given scenario to improve the spectrogram. The appropriate window length is another

decisive factor which improves the spectrogram. The concept of the spectrogram can be used to analyse the local Doppler PSD of a non-stationary channel.

The cross-term of the spectrogram introduces noise and reduces the frequency and time resolution. Further, for braking situations of the MS, the time-variant Doppler shift affects RSE-to-car communications by creating considerable fading in the non-stationary mobile radio channel. In [7] and [8], it has been shown the influence of the window length for the reduction of the cross-term. Comparison of the spectrogram which defined using different window functions is vital to select the best window type for better frequency and time resolution. The visual observation of the spectrogram does not always provide the correct results.

The braking manoeuvres of a vehicle can be segregated as "comfort braking action", where the vehicle is brought comfortably to the standstill and in an emergency stop, so-called "emergency braking action", where the vehicle is brought to a complete standstill as quickly as possible [14]. In comfort braking, the declaration is considerably low compared to the emergency braking. Usually, emergency braking takes place at higher speeds. In either case, the mobile radio channel exhibits non-stationarity. In the first case, non-stationarity occurs due to the time-varying speed of the MS. Additionally, for the second case, we can not assume that the time-variant AOA is negligible as in the first case. Therefore, it indicates the possible impreciseness of result if a single model is used to define the time-variant Doppler shift of the MS.

Perhaps a study which investigates the spectrogram optimisation methods by selecting optimum window lengths and applying techniques to reduce the cross-terms could remedy the situation. Further, the study should adequately cover the methods to conduct the comparison of the spectrogram of different window types. Finally, use of two different models to analyse the time-variant Doppler shift would provide a scalable solution for the spectrogram analysis of non-stationary mobile channels in braking situations.

1.4 Research Questions

Based on the above discussions, several research questions are raised and addressed with our proposed solutions throughout this thesis. The research questions and the contributions made by the proposed solutions are summarized in this section.

This thesis makes efforts to answer the following research questions.

- **Question 1(Q1)** In the presence of different analytical solutions using different window functions for the definitions of the spectrogram, How can we select the best window function to define the spectrogram for a given scenario?

- **Question 2(Q2)** How to verify the correctness and the preciseness of the developed analytical solutions of the spectrogram?

- **Question 3(Q3)** What kinds of approaches can be employed in order to improve the frequency and time resolution of the spectrogram for comfort and emergency braking scenarios?

- **Question 4(Q4)** Does the approximated instantaneous Doppler shift and the approximated AOA models accurately analyse the RSE-to-car non-stationary mobile radio channels for comfortable and emergency braking situations?

1.5 Research Methodology

This research work contains a number of iterating rounds. An iteration represents a work period with a short duration, usually a week time between supervisor meetings. Each iteration contains similar phases. Firstly, it is to start with a literature review, to obtain or refresh knowledge. Secondly, in the design phase, all modules of the research work will be created. The third is the implementation phase. In this phase, the model will be implemented and the result will be validated to assure the correctness of the model. Then the result will be analysed in the fourth phase. Here the simulation results will be compared with theoretical results. The final phase will contain an evaluation of the acquired results from phase four. After all phases are completed, the iteration process is considered as completed. The gained knowledge of the previous round will be continued for the next round. This cycle will be continued until the research work is complete.

1.6 Organization of the Master Thesis

This research work concentrates on the comprehensive investigations of different RSE-to-car communication scenarios using the spectrogram. The covered topics range from analytically defining the spectrogram using different window types up to analysis of the non-stationary channels using the spectrogram for time-invariant and time-variant angle of arrival (AOA) scenarios. The thesis is organised as follows:

- **Chapter 2** presents the basic concepts of mobile radio channel modelling and introduces related works which have been presented in previous publications.

- **Chapter 3** explains the multipath propagation scenario for non-stationary channel analysis. The definition of the time-variant velocity and the Doppler shift, are introduced in the current chapter. Furthermore, the scattering scenario and the description of the trajectories are well explained. A novel scenario which is useful to analyse the spectral behaviour of a vehicular mobile radio channel when the brakes are applied at a constant speed is introduced in Chapter 2.

- **Chapter 4** caters for the definition of the Spectrogram. The analytical definition of the spectrogram is introduced in the current chapter, and afterwards, different window types are used to define the spectrogram analytically. The Gaussian, rectangle and cosine windows (Hann, Hamming, and Blackman windows) are among the most widely used window types for the spectrogram. A new analytical definition is provided for the spectrogram using said cosine windows. Furthermore, the work is extended to define the spectrogram for stationary and non-stationary mobile channels.

- **Chapter 5** is dedicated to the numerical analysis of the spectrogram for RSE-to-car communication channels. In this chapter, the spectrogram analysis is carried out for a car travels at low velocity and considered the designed braking distances. It is assumed that the AOA is time-invariant under low mobile velocities. Consequently, the methods for selecting the best window type for the spectrogram for the given scenario is discussed. Furthermore, the phase averaging and the optimal window length is discussed as the methods for optimising the spectrogram. The actual

trial data of a car when deceleration in emergency stops, is used to analyse the spectral behaviour of a vehicular mobile radio channel using the spectrogram. In this scenario, it is considered that the AOA as time-variant.

- **Chapter 6** is dedicated to discuss the numerical resultants obtained in Chapter 5.

- **Chapter 7** summarises the main contributions of this thesis. We close this chapter by highlighting some areas as topics for future works.

Each chapter comprises an overview of the chapter at the beginning. A chapter summary is presented for Chapter 2,3 and 4. Chapter summary highlights the main findings of the chapter. Various sections deals with subtopics are addressed in each chapter.

Chapter 2

Basic Concepts and Related Work

Mobile speed variations result in non-stationary channels. The spectrogram is a vital tool for the analysis of stationary and non-stationary mobile radio channels. The stationary channel is modelled by a sum-of-cisoids and a non-stationary channel is modelled by a sum-of-chirps.

2.1 Overview of the Stationary and Non-Stationary Channels

The movement of the mobile station (MS) with a constant speed along a particular direction is considered as a standard assumption in mobile radio channel modelling. This assumption is not valid in the real-world as the speed and angle of motion rapidly varies with time. Therefore, the constant speed assumption potentially hides the actual mobile radio channels characteristics.

The wide-sense stationary assumption of a mobile radio channel is only valid for very short travelling distances of a mobile station (MS) as described in [18] and [19]. In the real-world, mobile communication channels exhibit non-stationarity as the frequency of each channel varies with the time. The change of velocities of MSs causes the channel statistics to be non-stationary. In [20], it is assumed that the transmitter is stationary and the receiver station linearly increases (or decreases) its speed, while the angle of motion is kept fixed. A fixed station-to-mobile multipath channel model with both varying speed and angle of motion (AOM) is presented in [21].

In [11], the non-stationary channels are divided into two classes. The class $\mathcal{A}$ model is categorised by channels models based on the integral relationship between the path phases and the respective instantaneous Doppler frequencies. The class $\mathcal{B}$ models can be obtained by replacing the time-invariant Doppler frequencies by time-variant Doppler frequencies.

The non-stationary channel behaviour for different scattering environments such as a campus, a highway, a suburban area, and an urban area, is presented in [9] for the measured V2V channels. In [10] it is presented the simulation results obtained from an implemented non-stationary physical layer model for IEEE 802.11p standard for vehicular communication. It has been shown that the shown that the channel estimation performance is strongly influenced mainly by the diffuse components strength, and the signal-to-noise ratio (SNR).

2.2 Review of the Spectrogram

The spectrogram is a vital tool to analyse non-stationary mobile multipath channel models. The spectrogram provides a three-dimensional (frequency, time and intensity) representation based on the spatial characteristics of the considered signal. Applications of the spectrogram can be found in many areas, such as music, sonar, radar, and speech processing, seismology, etc. The spectrogram consists of two terms: the auto-term and the cross-term. The auto-term provides an estimate of the local Doppler power spectral density (PSD) and the cross-term consists of unwanted noise and interferences [22]. The auto-term is independent of the phase while cross-term of the spectrogram depends on the phase. The spectrogram of a stationary or non-stationary signal is generated by breaking the signal into overlapping short-time signals and then by taking short-time Fourier transforms (STFT) of the short-time signals. In other words, the time varying signal (or time-invariant signal) can be multiplied by a moving window function to obtain overlapping short-time signals, and later on, the squared magnitude of the STFT of the short-time signals generates the spectrogram.

The length T of the window function is a decisive factor to improve the spectrogram. In [6] the authors estimated the Doppler power spectral density (PSD) of multipath fading channels which is modelled by sum-of-cisoids SOC_i processes, by means of the spectrogram. The proposed procedure has been recently extended in [7] to spectrogram analysis of multipath fading channels under variations of the mobile speed, in which the channel can be modelled by a sum-of-chirps SOC_h processes.

The fixed size window length for the STFT can cause poor resolution in the spectrogram but does not affect the cross-terms [23]. In [24], it is explained how the instantaneous frequency and instantaneous bandwidth are used to deduce the relation between window length and deviation of the Gaussian window so that the selection of the appropriate window length for the STFT is used to get the optimal SNR (signal-to-noise ratio), which subsequently optimises the spectrogram of the signal. Further, the average spectrogram also improves the time-varying frequency resolution. In [8], it is shown that cross-term of the spectrogram can be completely removed by averaging over the random phases.

2.3 The Average Doppler Shift and Doppler Spread

The most important characteristics of the Doppler PSD are the average Doppler shift and the Doppler spread. In stationary channels, the average Doppler shift depicts the average frequency shift of the carrier signal experienced during the transmission of the multipath mobile radio channel. Similarly, the average Doppler spread defines the average frequency spread. The first moment of the Doppler PSD provides the average Doppler shift, and the square root of the second central moment provides the average Doppler spread [25]. In non-stationary channels, the time-variant average Doppler shift is obtained by computing the sum of all power-weighted Doppler shifts normalised on the sum of the received power of all multipath components. The time-variant Doppler spread can be obtained by the channel gains, time-variant Doppler frequencies, and the time-variant average Doppler shift.

2.4 Definition of Consistency

The complex channel gain $\mu_n(t)$ of the nth received path component of a frequency-nonselective mobile radio channel can be defined as

$$\mu_n(t) = c_n \exp\left(j\theta_n(t)\right) \tag{2.1}$$

where c_n represents the path gain and $\theta_n(t)$ is the random phase associated with the nth path [11]. It should also be observed that $\theta_n(t)$ is a function of $f_n(t)$, i.e., $\theta_n(t) = g\left(f_n(t)\right)$. If we select the observation period such that the path gain c_n or the position of the MS does not vary with time t, the instantaneous power of nth multipath component equals the squared path gain, i.e., $|\mu_n(t)|^2 = c_n^2$.

The time-variant average Doppler shift can be presented as shown in [11] for all c_n and for time-variant Doppler shifts $f_n(t)$, by computing the sum of all power-weighted Doppler shifts normalized onto the sum of received powers of all multipath components according to

$$B_f^{(1)}(t) = \frac{\sum\limits_{n=1}^{N} c_n^2 f_n(t)}{\sum\limits_{n=1}^{N} c_n^2}. \tag{2.2}$$

Starting with the preceding equation, we can show that time-variant Doppler spread [11] as

$$B_f^{(2)}(t) = \sqrt{\frac{\sum\limits_{n=1}^{N} c_n^2 f_n^2(t)}{\sum\limits_{n=1}^{N} c_n^2} - \left(B_f^{(1)}(t)\right)^2}. \tag{2.3}$$

Alternatively, we can define the time-variant Doppler shift $B_\mu^{(1)}(t)$ and the time-variant Doppler spread $B_\mu^{(2)}(t)$ of the complex channel gain $\mu(t)$ for all N multipath components by considering the time-variant auto correlation function (ACF)

$$\mathcal{R}_\mu(\tau, t) = E\left\{\mu\left(t + \frac{\tau}{2}\right)\mu^*\left(t - \frac{\tau}{2}\right)\right\} \tag{2.4}$$

where $E\{.\}$ is the expectation operator and the $(.)^*$ denotes the complex conjugation operator [11].

Then, we can obtain time-variant Doppler shift $B_\mu^{(1)}(t)$ and the time-variant Doppler spread $B_\mu^{(2)}(t)$ by means of

$$B_\mu^{(1)}(t) = \frac{1}{2\pi j}\frac{\dot{\mathcal{R}}_\mu(0,t)}{\mathcal{R}_\mu(0,t)} \tag{2.5}$$

and

$$B_\mu^{(2)}(t) = \frac{1}{2\pi j}\sqrt{\left(\frac{\dot{\mathcal{R}}_\mu(0,t)}{\mathcal{R}_\mu(0,t)}\right)^2 - \frac{\ddot{\mathcal{R}}_\mu(0,t)}{\mathcal{R}_\mu(0,t)}} \tag{2.6}$$

where $\dot{\mathcal{R}}_\mu(0,t)$ and $\ddot{\mathcal{R}}_\mu(0,t)$ denotes the first and second derivative of $\mathcal{R}_\mu(\tau,t)$ w.r.t the τ at $\tau = 0$ [11].

As per the analysis in [11], if $B_f^{(2)}(t) = B_\mu^{(2)}(t)$ for all t, a non-stationary channel model is said to be consistent w.r.t the Doppler spread. Furthermore, in [11] it is

showed that the non-stationary channel models of Class $\mathcal{A}$ with constant c_n and random phases θ_n are consistent w.r.t average Doppler shift and Doppler spread, whereas the non-stationary channel models of Class $\mathcal{B}$ are inconsistent.

2.5 Chapter Summary

In this chapter, we have presented the main concepts and related previous works. The said concepts will be dealing throughout in the research work. This chapter has been presented the basic definition of the spectrogram and explained that the spectrogram is consisting of an auto-term and a cross-term. The auto-term can be removed by phase averaging and the spectrogram can be improved by selecting an optimum window length. It is further explained that the change of velocity of a MS causes the channel to exhibit non-stationarity. The non-stationary channel can be modelled as a consistency model or a non-consistency model w.r.t the time-variant average Doppler shift and the Doppler spread.

Chapter 3

Multipath Propagation Scenarios for Non-Stationary Channel Analysis

The scattering from the surface objects such as buildings, trees, etc. introduces multipath fading to the mobile radio communication channels. It is not possible to visualise the actual locations of the scatters. Hence, it is important to define a propagation scenario with different scattering models such as ring, random, cylindrical, etc. for the analysis of mobile radio channels. This chapter explains the propagation scenarios for non-stationary channel analysis. The consistency of the non-stationary channel model, the exact and approximated models of time-variant AOA and the instantaneous Doppler frequency, will also be discussed. The trajectory is explained for the comfort braking situation.

3.1 Introduction

Acceleration and deceleration are among the most basic concepts encountered in physics. The acceleration refers to a rate of change of velocity while deceleration refers to a value of acceleration which is negative. The acceleration of a car that travels in a straight line at a constant speed is zero.

The multipath propagation scenario considered for this research work consists of a fixed RSE and an MS which moves with time-variant velocity $\vec{V}(t)$. It is assumed that the RSE and the MS are equipped with omnidirectional antennas and a large number of N fixed scatterers $S_n(n = 1, 2, ..., N)$ which are located around the MS. The line-of-sight (LOS) component between the RSE and the MS is ignored. Furthermore, we assume that the channel is frequency-nonselective. Thus, the flat fading channel under speed variations can be defined by a sum-of-chirps (SOC_h) processes [7] . It is assumed that the distance between the RSE and the MS is sufficiently large so that the radio propagation environment can be modelled as two-dimensional. The propagation scenario is illustrated as shown in Fig. 3.1.

With the time-variant speed $\mathrm{v}(t)$ and the time-variant AOM $\alpha_v(t)$, $\vec{V}(t)$ can be defined as $\vec{V}(t) = \mathrm{v}(t) \exp(j\alpha_v(t))$ [20]. We assume that angle of motion (AOM) of the MS is constant during the channel observation period, i.e., $\alpha_v(t) = \alpha_v$. The $\mathrm{v}(t)$ can be denoted as

$$\mathrm{v}(t) = \mathrm{v}_0 + a_0 t \tag{3.1}$$

where, v_0 denotes the initial speed at $t = 0$, and a_0 is called the acceleration (when

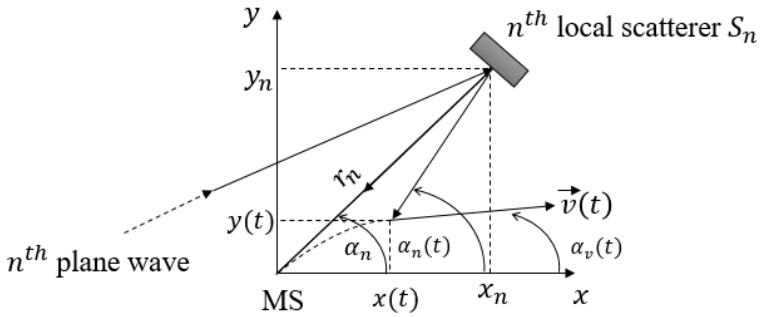

Figure 3.1: A multipath propagation scenario in which the MS travels with time-variant velocity $\vec{V}(t)$.

$a_0 > 0$) or deceleration (when $a_0 < 0$) parameter.

3.1.1 Exact and Approximated Time-Variant AOAs

The AOA $\alpha_n(t)$ is defined as the angle between the received nth incident plane wave and the x axis.

With reference to Fig. 3.1, the positions $x(t)$ and $y(t)$ of the MS at time t can be expressed as

$$x\,(t) = \int_0^t \mathrm{v}(z)\cos(\alpha_v(z))dz \tag{3.2}$$

and

$$y\,(t) = \int_0^t \mathrm{v}(z)\sin(\alpha_v(z))dz. \tag{3.3}$$

With this results in mind, for $n = 1, 2, ..., N$, we can then obtain the exact solution for the AOA $\alpha_n(t)$ as

$$\alpha_n(t) = \arctan\left(\frac{y_n - y(t)}{x_n - x(t)}\right). \tag{3.4}$$

The preceding equation can be simplified to a linear function of time t by developing the $\alpha_n(t)$ in a first-order Taylor series around time $t = 0$ and retaining only the first two terms [11]. In this case, we may write the approximated AOA $\alpha_n(t)$ as

$$\alpha_n(t) \approx \alpha_n + \gamma_n t \tag{3.5}$$

where

$$\alpha_n = \alpha_n(0) = \arctan\left(\frac{y_n}{x_n}\right) \tag{3.6}$$

$$\gamma_n = \frac{d}{dt}\alpha_n(t)|_{t=0} = \frac{\mathrm{v}_0}{r_n}\sin(\alpha_n - \alpha_v). \tag{3.7}$$

The approximation made in (3.5) influences the spectrogram and this error will be analysed in Chapter 5.

3.1.2 Time-Variant Doppler Frequency Models

When the MS changes its velocity $\vec{V}(t)$ over time t, nth received multipath component experiences a time-variant Doppler shift $f_n(t)$. The exact solution for the $f_n(t)$ can be modelled as

$$f_n(t) = f_{\max}(t) \,.\, \cos(\alpha_n(t) - \alpha_v) \tag{3.8}$$

using the exact AOA $\alpha_n(t)$ mentioned in (3.4) and the time-variant maximum Doppler frequency $f_{\max}(t)$. The $f_{\max}(t)$ is denoted as

$$f_{\max}(t) = \frac{f_0}{c_0}\mathrm{v}\,(t) = \frac{f_0}{c_0}(\mathrm{v}_0 + a_0\, t\,) \tag{3.9}$$

where f_0 is the carrier frequency and c_0 is the speed of light.

Consequently, by developing (3.8) in a Taylor series around $t = 0$ and retaining only the first two terms [11], we can simply define the time-variant Doppler shift $f_n(t)$ as

$$f_n\,(t) = f_n \,+\, k_n t \tag{3.10}$$

where

$$f_n = f_{\max}\cos(\alpha_n - \alpha_v) \tag{3.11}$$

$$k_n = \, f_{\max}\left[\frac{a_0}{\mathrm{v}_0}\cos\,(\alpha_n - \alpha_v) - \gamma_n \sin\,(\alpha_n - \alpha_v)\right] \tag{3.12}$$

and

$$\gamma_n = \, \frac{\mathrm{v}_0}{r_n}\sin(\alpha_n - \alpha_v). \tag{3.13}$$

In (3.11), $\alpha_n = \alpha_n(0)$ and $f_{\max} = f_{\max}(0)$, denotes the initial AOA at $t = 0$ and the initial maximum Doppler shift at $t = 0$, respectively. Further, in (3.12), k_n can be written as a sum of two terms. The first term takes into account the acceleration or deceleration of the MS and the second term is derived from the AOA of the MS. As a consequence of the time variant velocity and AOA of the MS, it follows that the Doppler shift $f_n(t)$ is a stochastic process. However, it should also be observed that for the stationary case, the acceleration parameter $a_0 = 0$ and $\gamma_n = 0$ will be resulted in reducing the stochastic process $f_n(t)$ to a random variable f_n and we finally obtained the conventional expression $f_n(t) = f_n = f_{\max}\cos(\alpha_n - \alpha_v)$, which is exclusively used to investigate the statistical properties of Doppler shift in stationary mobile radio channels.

3.1.3 The Consistency of the Model

Now we will turn our attention to the Class $\mathcal{A}$ channel model which is consistent w.r.t the average time-variant Doppler shift and the time-variant Doppler spread.

Considering that the random phase $\theta_n(t)$ is a function of the Doppler frequency $f_n(t)$, we can obtain the phase-frequency relationship [12, Eq. (1.3.40)] as

$$f_n(t) = \frac{1}{2\pi}\frac{d\theta_n(t)}{dt} \tag{3.14}$$

for all $n = 1, 2, ..., N$. A simple computation yields the expression

$$\theta_n(t) = \theta_n + 2\pi \int_0^t f_n(z)dz \tag{3.15}$$

where $\theta_n = \theta_n(0)$ denotes the initial phase at time t. Thereby, θ_n denotes a random phase angle which is distributed uniformly in the interval $[-\pi, \pi)$. Performing the substitution $f_n(t)$ from the linear approximated Doppler model presented in (3.10), the following expression is obtained for $\theta_n(t)$ in the form of

$$\theta_n(t) = \theta_n + 2\pi \left(f_n t + \frac{k_n}{2} t^2 \right). \tag{3.16}$$

The received complex envelope $\mu(t)$ of the Class $\mathcal{A}$ multipath non-stationary channel model which is consistent w.r.t the average time-variant Doppler shift and the time-variant Doppler spread can be defined as

$$\mu(t) = \sum_{n=1}^{N} c_n e^{j\left(\theta_n + 2\pi \int_0^t f_n(z)dz\right)}. \tag{3.17}$$

Further, by substituting (3.16) in the preceding equation we can obtain the complex channel gain of a narrowband multipath fading channel consisting of N paths and modelled by an SOC_h process with sum of n chirps as

$$\mu(t) = \sum_{n=1}^{N} c_n e^{j\left[2\pi\left(f_n t + \frac{k_n}{2} t^2\right) + \theta_n\right]}. \tag{3.18}$$

If the speed of the MS is constant, the non-stationary multipath fading channel can be treated as a stationary multipath fading channel. Therefore, the time-variant speed $\mathrm{v}(t) \longrightarrow \mathrm{v}_0$, which implies $k_n = 0$. After straightforward substitution of $k_n = 0$ in (3.18), the following equation is obtained the well-known SOC_i process

$$\mu(t) = \sum_{n=1}^{N} c_n e^{j(2\pi f_n t + \theta_n)}. \tag{3.19}$$

3.2 Description of the Scattering Scenario

We assume that scatterers are located with identical spacing on a ring of radius R centered on the MS. The extended method of exact Doppler spread (EMEDS) [13] is referred to obtain the initial AOAs α_n and the path gains c_n, which is given by

$$\alpha_n = \frac{2\pi}{N} \left(n - \frac{1}{4} \right), \quad n = 1, 2, \ldots, N \tag{3.20}$$

and

$$c_n = \sigma_0 \sqrt{\frac{2}{N}} \tag{3.21}$$

with parameter $\sigma_0 = 1$. Unless otherwise stated, the ring radius R and number of scatterers N are set to 100 m and 10, respectively. The scatterers S_n for $n = 1, 2, ..., 10$, are numbered and shown in the Fig. 3.2.

Figure 3.3 illustrates the received complex envelope $\mu(t)$ of the Class $\mathcal{A}$ multipath non-stationary channel model for the given scattering scenario.

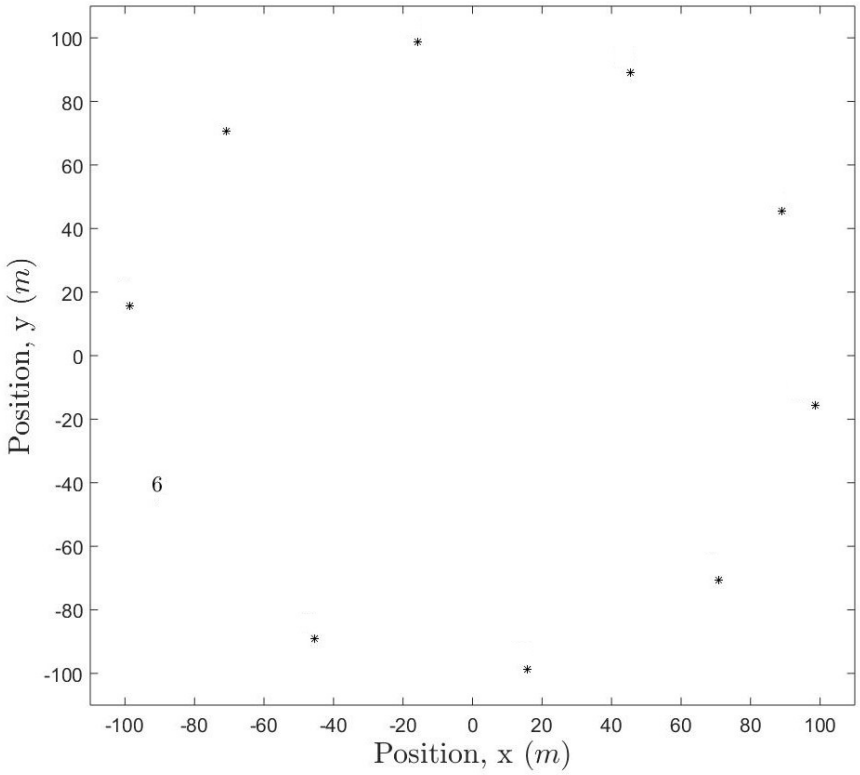

Figure 3.2: Locations of scatterers on a ring in the (x, y) plane.

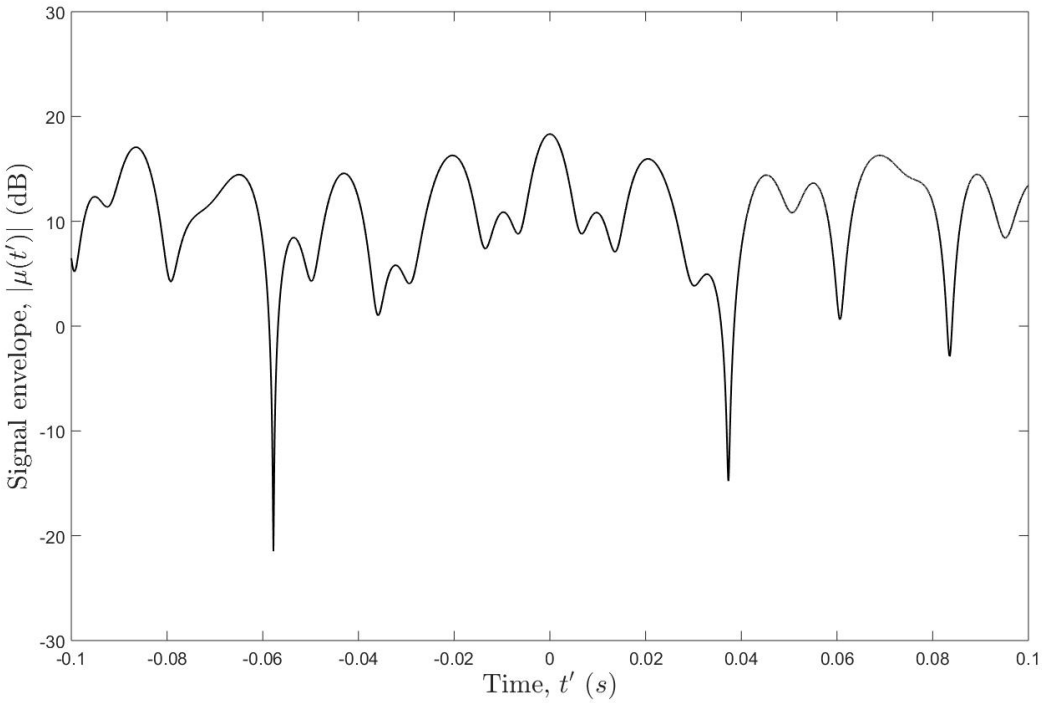

Figure 3.3: The received complex envelope $\mu(t)$ of the Class $\mathcal{A}$ multipath non-stationary channel model

3.3 Description of the Trajectory

A vehicle's braking distance depends on a number of factors such as the speed of the vehicle, road conditions (coefficient of friction and the grade of the road) and the driver's behaviour [14]. It takes time for a driver to react to a situation and start to apply the brakes. The car carries on moving during this reaction time. For our analysis, it suffices to assume that the reaction time is zero for all cases. The braking distance is the distance taken to stop the vehicle once the brakes are applied.

As a general case, we consider that the MS is moving at a constant speed on a straight road at the time the brakes are applied. Since the velocity is a vector that has both magnitude and direction, no change in either the magnitude or the direction constitutes no change in the velocity. Hence, the acceleration parameter $a_0 = 0$. When the brakes are applied, the acceleration occurs in the opposite direction as the movement of the vehicle, i.e., $a_0 = -a_0$. Finally, the MS comes to a stop.

Based on the above discussion, the multipath fading channel exhibits stationarity and nonstationarity during the observation time period.

The approximate braking distance [14] of a vehicle driving along a level road can be found by means of

$$d = 0.039\frac{\mathrm{v}(t')^2}{a_0} \tag{3.22}$$

where d and $\mathrm{v}(t')$ denote the braking distance (m) and the speed of the car (km/h) at the instant $(t = t')$ the brakes are applied.

Braking studies indicate that approximately 90% of motorists brake with a deceleration of more than 3.4 m/s^2, and this deceleration value helps motorists to control their vehicles even in wet road conditions. Thus,3.4 m/s^2 is used as recommended deceleration value [14] to use with (3.20). By applying $a_0 = 3.4$ m/s^2, we obtain the braking distances as shown in the Table 3.1.

Table 3.1: Braking distances for $a_0 = 3.4$ m/s^2.

Speed (km/h)	Braking distance (m)
20	5
30	10
40	18
50	29
60	41
70	56
80	73
90	93
100	115
110	139
120	165
130	194

We assume that the initial AOM $\alpha_v = 0$, and the MS does not change the AOM during the travel. Thereby, the trajectory can be defined as a speed profile. The speed profile of the MS is shown in Fig. 3.4 in which $\mathrm{v}(t') = 36$ km/h $= 10$ m/s.

3.4 Chapter Summary

This chapter explained the propagation scenario of RES-to-car non-stationary mobile radio communication. two models: the exact model and the approximated model, have been defined for the time-variant AOAs and the time-variant Doppler shifts. The consistency of the channel model is assured. The time-variant angle of motion (AOM) and the random locations of the scatterers are ignored for the simplicity of the non-stationary channel analysis. This could be declared as limitations of the research work covered under this chapter.

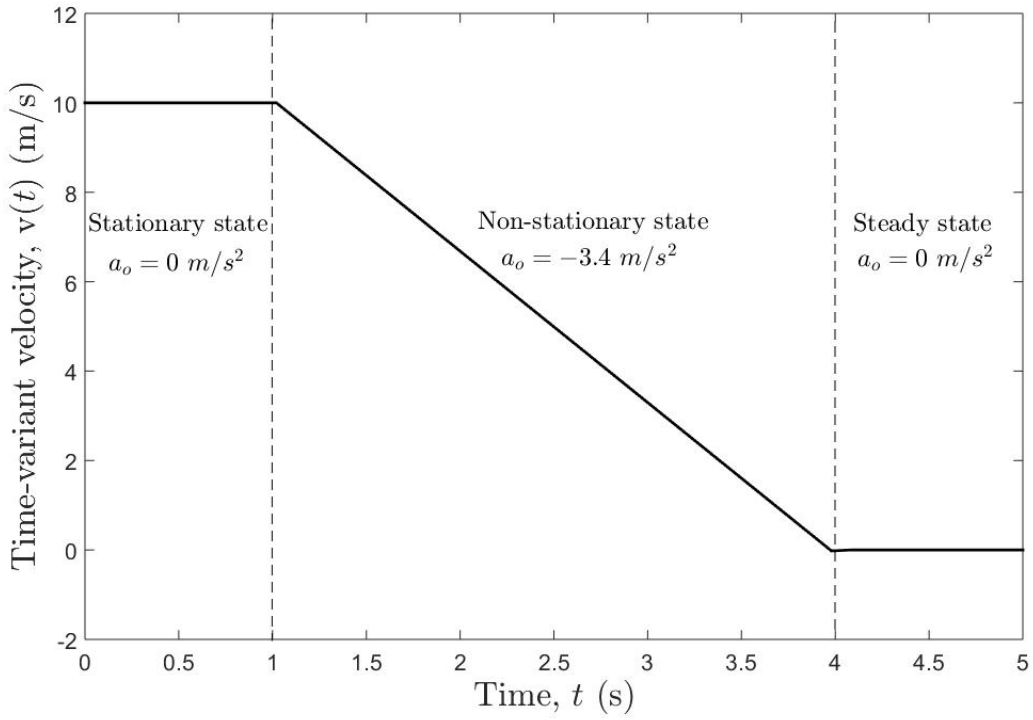

Figure 3.4: The speed profile of the MS for comfortable braking situations.

Chapter 4

Definition of the Spectrogram

The spectrogram provides visual frequency and time representation of a communication channel. This chapter defines the spectrogram using rectangle, Hann, Hamming, Blackman and Gaussian window functions. The auto-term and the cross-term are separated for the spectrogram defined by the said window types.

4.1 Basic Definition of the Spectrogram

A spectrogram displays a graphical representation of the strengths of the various component frequencies of a channel as time passes. The concept of spectrogram is widely used for the spectral analysis of stationary and non-stationary signals. The level of frequency/time resolution of the spectrogram depends on the size of the Fourier analysis window. A large window generates a narrow band spectrogram which resolves frequency at the expense of time, whilst short length window is better for the time resolution. The spectrogram windows are different kinds and each window has a specific shape, which determines the amount of energy spreads around each spectral component when the window is convolved with the signal.

We first consider the time-varying signal $\mu(t)$. The basic idea of the spectrogram is to take the time-variant signal and break it up to overlapping short-time signals. Then, the squared magnitude of the short-time Fourier transformation of short-time signals defines the spectrogram.

The short-time signal $X(f,t)$ of the time-varying signal $\mu(t)$ can be obtained by multiplying $\mu(t)$ by a a real valued window function $h(t)$ as shown in Fig. 4.1. The window $h(t)$ is real and positive function with normalized energy $\int_{-\infty}^{\infty} h^2 dt = 1$. There are many types of spectrogram window functions. However, for the simplicity now we select rectangle window function which is defined as

$$h(t) = \begin{cases} \frac{1}{\sqrt{T}}, & -\frac{T}{2} \leq t \leq \frac{T}{2} \\ 0, & \text{otherwise} \end{cases} \tag{4.1}$$

where, T denotes the window length. The short-time signal $x(t^{'},t)$ of $\mu(t)$ can be obtained by multiplying $\mu(t)$ by the window function $h(t)$ which is centered at time t according to

$$x(t^{'},t) = \mu(t')h(t'-t). \tag{4.2}$$

In the preceding eqation, t and t' can be defined as fixed and running time, respectively. Then, the short-time Fourier transform (STFT) of $X(f,t)$ with respect to the variable

t' can be defined as:

$$X(f,t) = \int_{-\infty}^{\infty} x(t',t)e^{-i2\pi ft'}dt'. \tag{4.3}$$

The squared magnitude of the STFT $X(f,t)$ defines the spectrogram $S_{xx}(f,t)$ as

$$S_{xx}(f,t) = |X(f,t)|^2. \tag{4.4}$$

Figure 4.2 illustrates the spectrogram $S_{xx}(f,t)$ for SOC_h process $\mu(t)$ for $T = 0.5$ s and $N = 10$ number of scatterers are located on a ring. The detailed method of obtaining the spectrogram is discussed in Section 4.2.

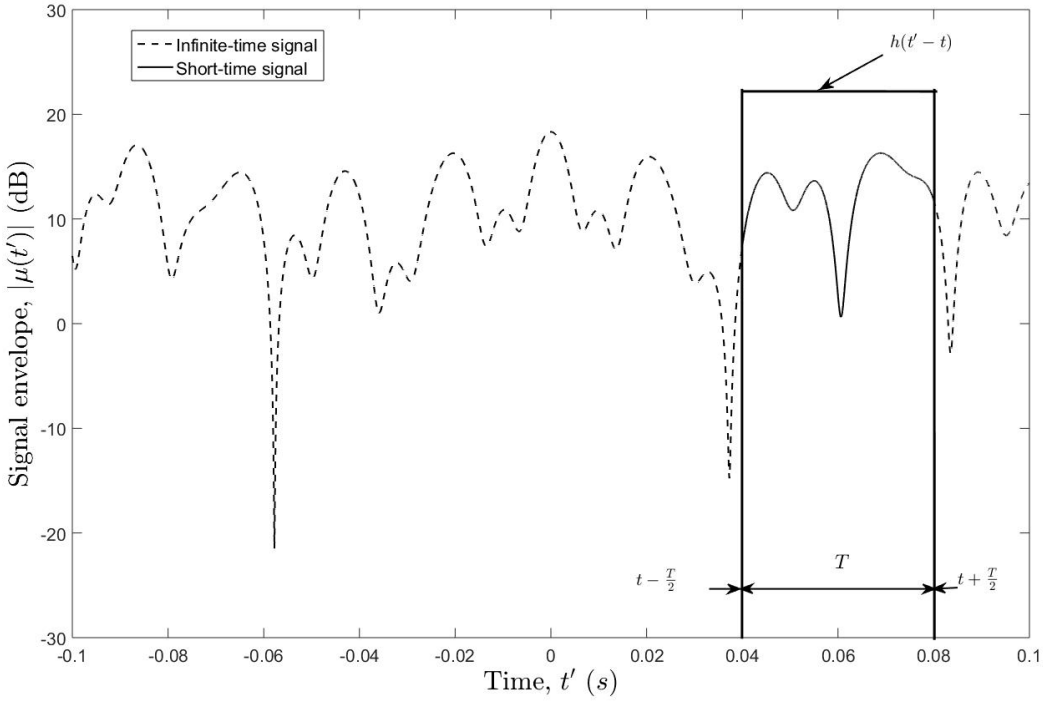

Figure 4.1: Time-varying signal $\mu(t)$ and the corresponding short-time signal $x(t',t)$ observed through a rectangular window of length T= 0.5 s centered at time t= 0.55 s.

4.2 Definition of the Spectrogram using Different Window Types

Windows are weighting functions applied to a signal to reduce the spectral leakage associated with long observation intervals [22]. The spectral leakage is known as the set of signals with frequencies other than the basis set. In another word, the spectral leakage increases the cross-term of the spectrogram. Hence, windows are used to reduce the undesirable effects related to spectral leakage. We will now discuss some well-known window types.

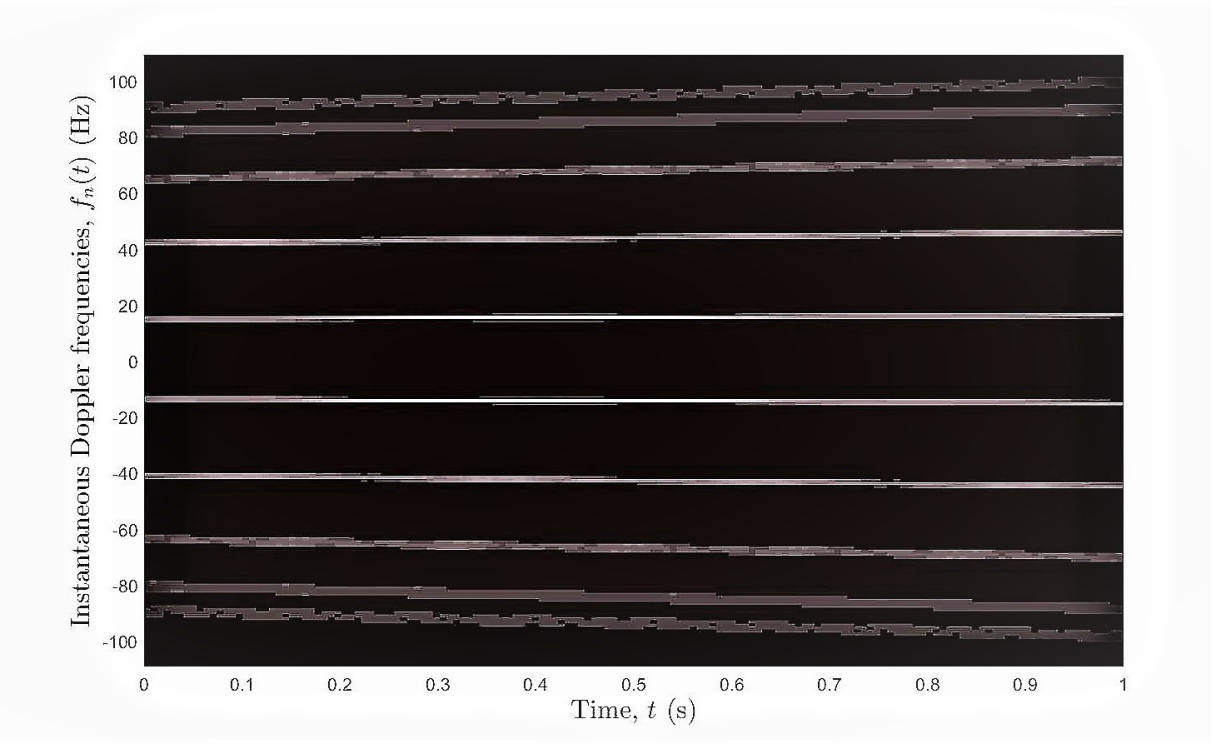

Figure 4.2: Spectrogram $S_{xx}(f,t)$ of SOC_h process $\mu(t)$ for $N = 10$, window size of $T = 0.5$ s and the scatterers are located on a ring.

4.2.1 Rectangle Window

The rectangle window is the simplest window type and it is unity over the observation interval. The Fourier transformation of a rectangle function is the sync function. Therefore, the rectangle window consists of multiple high-level side lobes which hinder the ability to distinguish different frequencies of a signal. This characteristic is sometimes described as a low dynamic range. Figures 4.3 (a) and (b) illustrate the energy normalized rectangle window and the log magnitude of the transformation.

$$h(t) = \begin{cases} \frac{1}{\sqrt{T}}, & -\frac{T}{2} \leq t \leq \frac{T}{2} \\ 0, & \text{otherwise} \end{cases} \tag{4.5}$$

The rectangle window provides the smallest bandwidth. However, because of the unacceptable spectral leakage effect, the rectangular window is not suitable for standard applications. The frequency response of the rectangle window is a sinc function, which consists non-zero values from positive infinity to negative infinity. Convolution of the sinc function with any narrow-band signal causes a spread-out spectrum. Therefore, the rectangular window is efficient for the analysis of transients with shorter duration than that of the window. The transients only exist for a very short time duration.

According to the simulation scenario which is discussed in Chapter 3, the multipath fading channel can be modelled by a combination of SOC_i and SOC_h process. In the speed profile (see Fig. 3.4), we can observe stationarity behaviour in the first part of the speed profile and non-stationarity behaviour in the second part. Thus, it is important to define the spectrogram for both the cases.

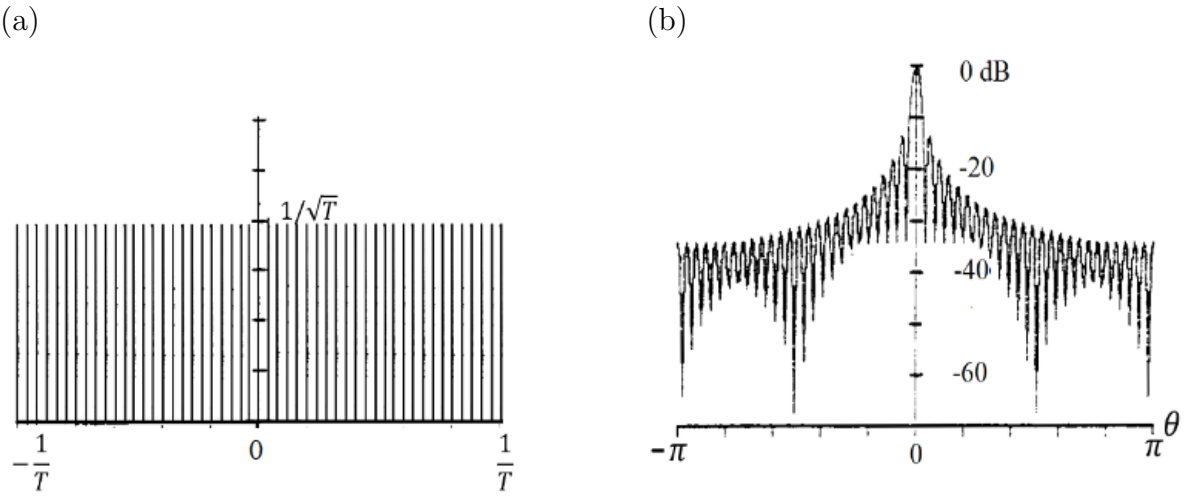

Figure 4.3: (a) rectangle window, and (b) log-magnitude of the transform [22].

The spectrogram of SOC$_i$ Processes using the Rectangle Window Function

A broad definition of the spectrogram for a stationary multipath fading channel which is modelled by a sum of SOC$_i$ processes is described in [6]. We use the same method to define the spectrogram during the stationary period of the channel.

With reference to (4.2), the stationary multipath fading channel which is modelled by a sum of SOC$_i$ processes as $\mu(t) = \sum_{n=1}^{N} c_n \exp\{j(2\pi f_n t + \theta_n)\}$ [see (3.19)]is used to obtain the STFT $X(f,t)$ w.r.t rectangle window function $h(t)$, is directly given by

$$X(f,t) = \int_{t-\frac{T}{2}}^{t+\frac{T}{2}} x(t',t) e^{-i2\pi f t'} dt' \tag{4.6}$$

where $x(t',t)$ is obtained according to (4.2) as

$$x(t',t) = \frac{1}{\sqrt{T}} \sum_{n=1}^{N} c_n e^{j(2\pi f_n t' + \theta_n)}. \tag{4.7}$$

After substituting (4.7)and using some elementary mathematical manipulations we can represent the integral in (4.6) as follows

$$X(f,t) = \frac{1}{\sqrt{T}} \int_{t-\frac{T}{2}}^{t+\frac{T}{2}} \sum_{n=1}^{N} c_n e^{-j(2\pi(f-f_n)t' - \theta_n)} dt' \tag{4.8}$$

The solution of the integral of the preceding equation can be written as

$$X(f,t) = \sqrt{T} \sum_{n=1}^{N} c_n e^{-j(2\pi(f-f_n)t - \theta_n)} \mathrm{sinc}[\pi(f-f_n)T] \tag{4.9}$$

where $\mathrm{sinc}(x) = \frac{\sin(x)}{x}$.

The spectrogram $S_{xx}(f,t) = |X(f,t)|^2$ can be further elaborated as follows [6]:

$$\begin{aligned}
S_{xx}(f,t) &= |X(f,t)|^2 = X(f,t).X^*(f,t) \\
&= \sqrt{T}\sum_{n=1}^{N} c_n e^{-j(2\pi(f-f_n)t-\theta_n)}\text{sinc}[\pi(f-f_n)T] \\
&\quad .\sqrt{T}\sum_{n=1}^{N} c_n e^{-j(2\pi(f-f_n)t-\theta_n)}\text{sinc}[\pi(f-f_n)T] \\
&= T\sum_{n=1}^{N}\sum_{m=1}^{N} \mu_n(t)\mu_m^*(t).\text{sinc}[\pi(f-f_n)T]\text{sinc}[\pi(f-f_m)T] \\
&= T\sum_{n=1}^{N} |\mu_n(t)|^2 \text{sinc}^2[\pi(f-f_n)T] + T\sum_{n=1}^{N}\sum_{\substack{m=1 \\ m\neq n}}^{N} \mu_n(t)\mu_m^*(t)\text{sinc}[\pi(f-f_m)T]
\end{aligned}$$

After using $|\mu_n(t)|^2$, $\text{Re}\{x\} = (x + x^*)$ and with some mathematical manipulations, we can define the spectrogram $S_{xx}(f,t) = |X(f,t)|^2$ as a sum of the auto-term $S_{xx}^{(a)}(f,t)$ and the cross-term $S_{xx}^{(a)}(f,t)$ as follows [6]:

$$S_{xx}(f,t) = S_{xx}^{(a)}(f,t) + S_{xx}^{(c)}(f,t) \tag{4.10}$$

where

$$S_{xx}^{(a)}(f,t) = T\sum_{n=1}^{N} c_n^2 \text{sinc}^2[\pi(f-f_n)T] \tag{4.11}$$

and

$$S_{xx}^{(c)}(f,t) = 2T\sum_{n=1}^{N}\sum_{\substack{m=1 \\ m\neq n \\ m>n}}^{N} \text{Re}\{\mu_n(t)\mu_m^*(t)\}\text{sinc}[\pi(f-f_n)T].\text{sinc}[\pi(f-f_m)T]. \tag{4.12}$$

The spectrogram of SOC$_h$ Processes using the Rectangle Window Function

The time-variant speed of the of the MS causes mobile channel to exhibit non-stationarity. Then, the channel can be modelled by a sum-of-chirps SOC$_h$ processes. In [7], a closed foam solution is presented for the spectrogram of SOC$_h$ channel model. We directly adopt the equation for STFT $X(f,t)$ and the spectrogram $S_{xx}(f,t)$ which appear as (12-19) and (20-22) in [7].

The STFT $X(f,t)$ of SOC$_h$ processes $\mu(t) = \sum_{n=1}^{N} c_n \exp\left\{j\left(2\pi\left(f_n t + \frac{k_n}{2}t^2\right) + \theta_n\right)\right\}$ can be expressed as (without proof)

$$X(f,t) = \frac{1}{\sqrt{2T}}\sum_{n=1}^{N} g_n(f)\triangle \text{Z}_n(f,t) \tag{4.13}$$

where

$$g_n(f) = \frac{c_n}{\sqrt{|k_n|}} e^{j\left[\theta_n - \frac{\pi}{k_n}(f-f_n)^2\right]} \tag{4.14}$$

$$\triangle \text{Z}_n(f,t) = \begin{cases} \text{Z}\left(u_n^{(+)}\right) - \text{Z}\left(u_n^{(-)}\right) & \text{if } k_n > 0 \\ 0 & \text{if } k_n = 0 \\ \text{Z}^*\left(u_n^{(+)}\right) - \text{Z}^*\left(u_n^{(-)}\right) & \text{if } k_n < 0 \end{cases} \tag{4.15}$$

$$u_n^{\pm} = u_n^{\pm}(f,t) = \sqrt{\pi|k_n|}\left(t \pm \frac{T}{2} - \frac{f-f_n}{k_n}\right). \tag{4.16}$$

and

$$\mathrm{Z}(u) = \mathrm{C}(u) + j\mathrm{S}(u) = \sqrt{\frac{j}{2}}\mathrm{erf}\left(\frac{u}{\sqrt{j}}\right) \tag{4.17}$$

The function $\mathrm{erf}(u)$ denotes the error function and $\mathrm{C}(u)$ and $\mathrm{S}(u)$ are the Fresnel integrals [15, Eqs. (8.250-2)-(8.250-4)].

The spectrogram can be expressed as a sum of auto and cross terms as follows (without proof)

$$S_{xx}(f,t) = S_{xx}^{(a)}(f,t) + S_{xx}^{(c)}(f,t) \tag{4.18}$$

where

$$S_{xx}^{(a)}(f,t) = \frac{1}{2T}\sum_{n=1}^{N}\frac{c_n^2}{|k_n|}\left|\triangle \mathrm{Z}_n(f,t)\right|^2 \tag{4.19}$$

and

$$S_{xx}^{(c)}(f,t) = \frac{1}{T}\sum_{n=1}^{N}\sum_{\substack{m=2\\m>n}}^{N}\mathrm{Re}\left\{g_n(f)\,g_m^*(f)\,\triangle \mathrm{Z}_n(f,t)\triangle \mathrm{Z}_m^*(f,t)\right\}. \tag{4.20}$$

The definitions of spectrogram both for the channel models defined as a sum of SOC_i and SOC_h processes are widely used to define the spectrogram using cosine windows (Hann, Hamming and, Blackman windows) which is a novelty of this research work.

4.2.2 Hann Window

The Hann window belongs to the family of $\cos^{\alpha}(X)$ windows, in which integer parameter α, decides the type of the window. The value of the $\alpha = 2$ is defines the well known Hanning window. However, the correct name of the Hanning window is "Hann" [16]. For $\alpha = 2$, we now define the Hann window with normalized energy as [16]

$$h(t) = \sqrt{\frac{2}{3T}}\left(1 + \cos\left(\frac{2\pi t}{T}\right)\right), \quad -\frac{1}{T} \le t \le \frac{1}{T}. \tag{4.21}$$

Figures 4.4 (a) and (b) illustrate the energy normalized Hann window and the log magnitude of the transformation.

(a) (b)

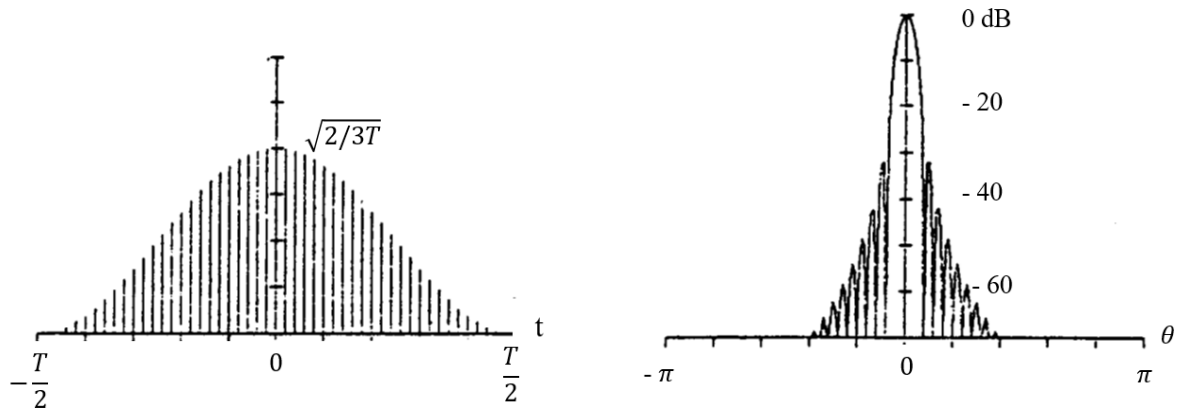

Figure 4.4: (a) Hann window, and (b) log-magnitude of the transform [22].

The fast fallout of the side lobes improves the dynamic range in the Hann window. We note from the inspection of Fig. 4.4 (b) that the power level of the side lobes is significantly suppressed. The Hann window is well known for low aliasing, however, the trade-off is slightly decreased resolution caused by widening of the main lobe. Aliasing is known as an effect that causes different signals to become indistinguishable (or aliases of one another) when sampled [17]. Therefore, if the Hann window is used to sample a signal in order to convert to frequency domain, it is complex to reconvert to the time domain without adding distortions.

The spectrogram of SOC$_i$ Processes using the Hann Window Function

By using the definition of STFT $X(f,t)$ in equations (4.2) and (4.3), now we define the STFT $X(f,t)$ using the Hann window function $h(t)$ (4.21) for the stationary multipath fading channel which is modelled by a sum of SOC$_i$ processes $\mu(t) = \sum_{n=1}^{N} c_n \exp\{j\,(2\pi f_n t + \theta_n)\}$ as given by

$$X\,(f,t) = \sqrt{\frac{2}{3T}} \int_{t-\frac{T}{2}}^{t+\frac{T}{2}} \mu(t') \left(1 + \cos\left(\frac{2\pi t}{T}\right)\right) e^{-i2\pi f t'} dt'. \tag{4.22}$$

by expanding the cosine term using complex exponentials, and with some elementary mathematical manipulations, we can expand the preceding equation as

$$\begin{aligned} X\,(f,t) = \sqrt{\frac{2}{3}} \left[\frac{1}{\sqrt{T}} \int_{t-\frac{T}{2}}^{t+\frac{T}{2}} \mu(t') e^{-i2\pi f t'} dt'\right] + \frac{1}{\sqrt{6}} \left[\frac{1}{\sqrt{T}} \int_{t-\frac{T}{2}}^{t+\frac{T}{2}} \mu(t') e^{-i2\pi \left(f-\frac{1}{T}\right) t'} dt'\right] \\ + \frac{1}{\sqrt{6}} \left[\frac{1}{\sqrt{T}} \int_{t-\frac{T}{2}}^{t+\frac{T}{2}} \mu(t') e^{-i2\pi \left(f+\frac{1}{T}\right) t'} dt'\right]. \end{aligned} \tag{4.23}$$

Inserting $\mu(t) = \sum_{n=1}^{N} c_n \exp\{j\,(2\pi f_n t + \theta_n)\}$ in (4.23) gives

$$X\,(f,t) = \sqrt{\frac{2}{3}} \left[X_1^{Rect}(f,t)\right] + \frac{1}{\sqrt{6}} \left[X_2^{Rect}(f,t)\right] + \frac{1}{\sqrt{6}} \left[X_3^{Rect}(f,t)\right] \tag{4.24}$$

which can be further reduced as

$$X\,(f,t) = \sum_{\mathcal{L}=1}^{3} \mathcal{P}_{\mathcal{L}} \left[X_{\mathcal{L}}^{Rect}(f,t)\right] \tag{4.25}$$

where $X_{\mathcal{L}}^{Rect}(f,t)$ for $\mathcal{L} = 1,2,3$ denotes three STFTs obtained for the SOC$_i$ processes using the rectangle window function and the values of $\mathcal{P}_{\mathcal{L}}$ for $\mathcal{L} = 1,2,3$ are given as $\sqrt{\frac{2}{3}}$, $\frac{1}{\sqrt{6}}$, and $\frac{1}{\sqrt{6}}$, respectively.

Therefore , the STFT $X\,(f,t)$ obtained by using Hann window function can be expanded as a sum of STFTs $X_{\mathcal{L}}^{Rect}(f,t)$ obtained by the rectangle window function.

The STFTs $X_{\mathcal{L}}^{Rect}(f,t)$ for $\mathcal{L}=1,2,3$ are given by

$$X_{\mathcal{L}}^{Rect}(f,t)=\sqrt{T}\sum_{n=1}^{N}c_n e^{-j(2\pi((f+\mathcal{D}_{\mathcal{L}})-f_n)t-(\theta_n+\mathcal{E}_{\mathcal{L}}))}\text{sinc}[\pi((f+\mathcal{D}_{\mathcal{L}})-f_n)T] \tag{4.26}$$

for $\mathcal{L}=1,2,3$, the *constant frequency parameter* $\mathcal{D}_{\mathcal{L}}=0,-\frac{1}{T},\frac{1}{T}$ and the *time-variant phase parameter* $\mathcal{E}_{\mathcal{L}}=0,-\frac{2\pi t}{T},\frac{2\pi t}{T}$, respectively.

The spectrogram $S_{xx}(f,t)$ can be derived by taking the squared magnitude of the $X(f,t)$ as follows:

$$S_{xx}\left(f,t\right)=\left|X\left(f,t\right)\right|^2=\left|\sum_{\mathcal{L}=1}^{3}\mathcal{P}_{\mathcal{L}}\left[X_{\mathcal{L}}^{Rect}(f,t)\right]\right|^2. \tag{4.27}$$

The spectrogram $S_{xx}(f,t)$ consists three auto terms $S_{xx}^{(a)}(f,t)$ and six cross terms $S_{xx}^{(c)}(f,t)$ shown as

$$S_{xx}^{(a)}(f,t)=T\sum_{\mathcal{L}=1}^{3}\sum_{n=1}^{N}\mathcal{P}_{\mathcal{L}}^2c_n^2\text{sinc}^2[\pi((f+\mathcal{D}_{\mathcal{L}})-f_n)T] \tag{4.28}$$

and

$$\begin{aligned}S_{xx}^{(c)}(f,t)=2T\sum_{\mathcal{L}=1}^{3}\sum_{n=1}^{N}\sum_{\substack{m=1\\m\neq n}}^{N}\mathcal{P}_{\mathcal{L}}^2\text{Re}\left\{\mu_n\left(t\right)\mu_m^*\left(t\right)\right\}\text{sinc}[\pi((f+\mathcal{D}_{\mathcal{L}})-f_n)T].\\ \text{sinc}[\pi((f+\mathcal{D}_{\mathcal{L}})-f_m)T]+\\ 2T\sum_{\substack{\mathcal{L}=1\\\mathcal{N}=1\\\mathcal{L}\neq\mathcal{N}}}^{3}\sum_{n=1}^{N}\sum_{\substack{m=1\\m\neq n}}^{N}\mathcal{P}_{\mathcal{L}}\mathcal{P}_{\mathcal{N}}\text{Re}\left\{\mu_n\left(t\right)\mu_m^*\left(t\right)\right\}\text{sinc}[\pi((f+\mathcal{D}_{\mathcal{L}})-f_n)T].\\ \text{sinc}[\pi((f+\mathcal{D}_{\mathcal{N}})-f_m)T].\end{aligned} \tag{4.29}$$

Finally, we can define the spectrogram $S_{xx}(f,t)$ as

$$S_{xx}\left(f,t\right)=S_{xx}^{(a)}(f,t)+S_{xx}^{(c)}(f,t) \tag{4.30}$$

The spectrogram of SOC$_h$ Processes using the Hann Window Function

Following the similar mathematical manipulations as given in (4.22-4.25), for the SOC$_h$ processes $\mu(t)=\sum_{n=1}^{N}c_n\exp\left\{j\left(2\pi\left(f_nt+\frac{k_n}{2}t^2\right)+\theta_n\right)\right\}$, the STFT $X(f,t)$ using the energy normalised Hann window function can be directly expressed as

$$X\left(f,t\right)=\sum_{\mathcal{M}=1}^{3}\mathcal{R}_{\mathcal{M}}\left[X_{\mathcal{M}}^{Rect}(f,t)\right] \tag{4.31}$$

where $X_{\mathcal{M}}^{Rect}(f,t)$ for $\mathcal{M}=1,2,3$ denotes three STFTs obtained for SOC$_h$ Processes using using the rectangle function and the values of $\mathcal{R}_{\mathcal{M}}$ for $\mathcal{M}=1,2,3$, are given as $\sqrt{\frac{2}{3}},\frac{1}{\sqrt{6}}$, and $\frac{1}{\sqrt{6}}$, respectively.

We now define $X_{\mathcal{M}}^{Rect}(f,t)$ for $\mathcal{M}=1,2,3$ in closed form as [see (4.13)]

$$X_{\mathcal{M}}^{Rect}(f,t) = \frac{1}{\sqrt{2T}} \sum_{n=1}^{N} g_n^{\mathcal{M}}(f) \triangle \mathrm{Z}_n^{\mathcal{M}}(f,t) \tag{4.32}$$

where

$$g_n^{\mathcal{M}}(f) = \frac{c_n}{\sqrt{|k_n|}} e^{j\left[(\theta_n + \mathcal{G}_{\mathcal{M}}) - \frac{\pi}{k_n}((f+\mathcal{I}_{\mathcal{M}}) - f_n)^2\right]} \tag{4.33}$$

$$\triangle \mathrm{Z}_n^{\mathcal{M}}(f,t) = \begin{cases} \mathrm{Z}\left(u_{n\mathcal{M}}^{(+)}\right) - \mathrm{Z}\left(u_{n\mathcal{M}}^{(-)}\right) & \text{if } k_n > 0 \\ 0 & \text{if } k_n = 0 \\ \mathrm{Z}^*\left(u_{n\mathcal{M}}^{(+)}\right) - \mathrm{Z}^*\left(u_{n\mathcal{M}}^{(-)}\right) & \text{if } k_n < 0 \end{cases} \tag{4.34}$$

$$u_{n\mathcal{M}}^{\pm} = u_{n\mathcal{M}}^{\pm}(f,t) = \sqrt{\pi\,|k_n|}\left(t \pm \frac{T}{2} - \frac{(f+\mathcal{I}_{\mathcal{M}}) - f_n}{k_n}\right) \tag{4.35}$$

and

$$\mathrm{Z}(u) = \mathrm{C}(u) + j\mathrm{S}(u) = \sqrt{\frac{j}{2}}\mathrm{erf}\left(\frac{u}{\sqrt{j}}\right) \tag{4.36}$$

in which, for $\mathcal{M}$ ($\mathcal{M} = 1, 2, 3$), the *constant frequency parameter* $\mathcal{I}_{\mathcal{M}} = 0, -\frac{1}{T}, \frac{1}{T}$ and the *time-variant phase parameter* $\mathcal{G}_{\mathcal{M}} = 0, -\frac{2\pi t}{T}$ and, $\frac{2\pi t}{T}$, respectively.

Now we define the spectrogram $S_{xx}(f,t)$ for the sum of SOC_h processes as follows

$$S_{xx}(f,t) = |X(f,t)|^2 = \left|\sum_{\mathcal{M}=1}^{3} \mathcal{R}_{\mathcal{M}}\left[X_{\mathcal{M}}^{Rect}(f,t)\right]\right|^2. \tag{4.37}$$

We can define the spectrogram $S_{xx}(f,t)$ consisting three auto terms $S_{xx}^{(a)}(f,t)$ and six cross terms $S_{xx}^{(c)}(f,t)$ as follows

$$S_{xx}(f,t) = S_{xx}^{(a)}(f,t) + S_{xx}^{(c)}(f,t) \tag{4.38}$$

where

$$S_{xx}^{(a)}(f,t) = \frac{1}{2T} \sum_{\mathcal{M}=1}^{3} \sum_{n=1}^{N} \mathcal{R}_{\mathcal{M}}^2 \frac{c_n^2}{|k_n|} \left|\triangle \mathrm{Z}_n^{\mathcal{M}}(f,t)\right|^2 \tag{4.39}$$

and

$$\begin{aligned} S_{xx}^{(c)}(f,t) = &\frac{1}{T} \sum_{\mathcal{M}=1}^{3} \sum_{n=1}^{N} \sum_{\substack{m=1 \\ m\neq n}}^{N} \mathcal{P}_{\mathcal{M}}^2 \mathrm{Re}\left\{g_n^{\mathcal{M}}(f) g_m^{*\mathcal{M}}(f) \triangle \mathrm{Z}_n^{\mathcal{M}}(f,t) \triangle \mathrm{Z}_m^{*\mathcal{M}}(f,t)\right\} + \\ &\frac{1}{T} \sum_{\substack{\mathcal{M}=1 \\ \mathcal{N}=1 \\ \mathcal{M}\neq\mathcal{N}}}^{3} \sum_{n=1}^{N} \sum_{\substack{m=1 \\ m\neq n}}^{N} \mathcal{R}_{\mathcal{M}} \mathcal{R}_{\mathcal{N}} \mathrm{Re}\left\{g_n^{\mathcal{M}}(f) g_m^{*\mathcal{N}}(f) \triangle \mathrm{Z}_n^{\mathcal{M}}(f,t) \triangle \mathrm{Z}_m^{*\mathcal{N}}(f,t)\right\}. \end{aligned} \tag{4.40}$$

4.2.3 Hamming Window

The hamming window function $h(t)$ is a modified version of the Hann window function with coefficient $\alpha = 25/46 \approx 0.54$ which is nearly set the minimum sidelobe levels. We now define the Hamming window function with normalized energy as

$$h(t) = \frac{1.58}{\sqrt{T}}\left(1 + \cos\left(\frac{2\pi t}{T}\right)\right), \quad -\frac{1}{T} \leq t \leq \frac{1}{T}. \tag{4.41}$$

Figure 4.5 illustrates the energy normalized Hamming window with the noticeable attenuation at missing sidelobe positions.

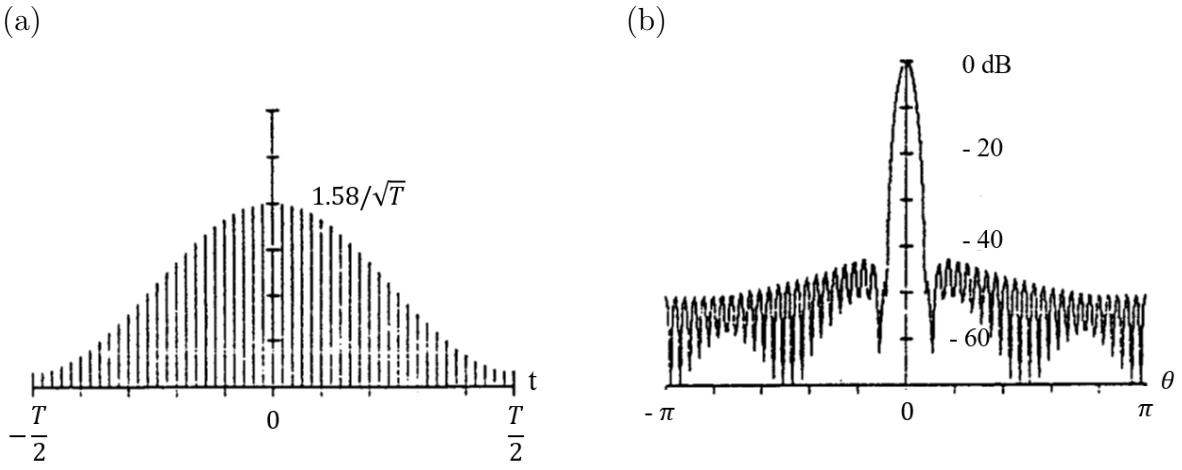

Figure 4.5: (a) Hamming window, and (b) log-magnitude of the transform [22].

The spectrogram of SOC$_i$ Processes using the Hamming Window Function

Outlining similarities with Hann window function [see (4.21)] and Hamming window function, we now directly define the STFT $X(f,t)$ and the spectrogram $f_{xx}(f,t)$ for the multipath fading channel modelled by a sum of SOC$_i$ processes as
(without proof)

$$X(f,t) = 0.85\left[X_1^{Rect}(f,t)\right] + 0.36\left[X_2^{Rect}(f,t)\right] + 0.36\left[X_3^{Rect}(f,t)\right] \tag{4.42}$$

which can be further reduced as

$$X(f,t) = \sum_{\mathcal{O}=1}^{3} \mathcal{T}_{\mathcal{O}}\left[X_{\mathcal{O}}^{Rect}(f,t)\right] \tag{4.43}$$

and we define the spectrogram $S_{xx}(f,t)$ consisting three auto terms $S_{xx}^{(a)}(f,t)$ and six cross terms $S_{xx}^{(c)}(f,t)$ directly according to

$$S_{xx}^{(a)}(f,t) = T\sum_{\mathcal{O}=1}^{3}\sum_{n=1}^{N} \mathcal{T}_{\mathcal{O}}^2 c_n^2 \mathrm{sinc}^2[\pi((f+\mathcal{B}_{\mathcal{O}}) - f_n)T] \tag{4.44}$$

and

$$\begin{aligned} S_{xx}^{(c)}(f,t) = 2T \sum_{\mathcal{O}=1}^{3} \sum_{n=1}^{N} \sum_{\substack{m=1 \\ m\neq n}}^{N} \mathcal{T}_{\mathcal{O}}^{2} \mathrm{Re}\left\{\mu_n(t)\,\mu_m^*(t)\right\} \mathrm{sinc}[\pi((f+\mathcal{B}_{\mathcal{O}})-f_n)T]. \\ \mathrm{sinc}[\pi((f+\mathcal{B}_{\mathcal{O}})-f_m)T] + \\ 2T \sum_{\substack{\mathcal{O}=1 \\ \mathcal{N}=1 \\ \mathcal{O}\neq\mathcal{N}}}^{3} \sum_{n=1}^{N} \sum_{\substack{m=1 \\ m\neq n}}^{N} \mathcal{T}_{\mathcal{O}}\mathcal{T}_{\mathcal{N}} \mathrm{Re}\left\{\mu_n(t)\,\mu_m^*(t)\right\} \mathrm{sinc}[\pi((f+\mathcal{B}_{\mathcal{O}})-f_n)T]. \\ \mathrm{sinc}[\pi((f+\mathcal{B}_{\mathcal{N}})-f_m)T]. \end{aligned} \tag{4.45}$$

where $X_{\mathcal{O}}^{Rect}(f,t)$ for $\mathcal{O}=1,2,3$ denotes three STFTs obtained for the SOC_i processes using the rectangle function and the values of $\mathcal{T}_{\mathcal{O}}$ for $\mathcal{O}=1,2,3$ are given as 0.85, 0.36, and 0.36, respectively.

The spectrogram $S_{xx}(f,t)$ is

$$S_{xx}(f,t) = S_{xx}^{(a)}(f,t) + S_{xx}^{(c)}(f,t) \tag{4.46}$$

The spectrogram of SOC_h Processes using the Hamming Window Function

We directly define $X(f,t)$ for the sum of SOC_h processes as
(without proof)

$$X(f,t) = \sum_{\mathcal{C}=1}^{3} \mathcal{H}_{\mathcal{C}} \left[X_{\mathcal{C}}^{Rect}(f,t)\right] \tag{4.47}$$

where $\mathcal{H}_{\mathcal{C}}$ for $\mathcal{C}=1,2,3$ are given as 0.85, 0.36, and 0.36, respectively.

We now define the spectrogram $S_{xx}(f,t)$ for the sum of SOC_h processes as follows

$$S_{xx}(f,t) = |X(f,t)|^2 = \left| \sum_{\mathcal{C}=1}^{3} \mathcal{H}_{\mathcal{C}} \left[X_{\mathcal{C}}^{Rect}(f,t)\right] \right|^2 \tag{4.48}$$

where

$$X_{\mathcal{C}}^{Rect}(f,t) = \frac{1}{\sqrt{2T}} \sum_{n=1}^{N} g_n^{\mathcal{C}}(f) \triangle \mathrm{Z}_n^{\mathcal{C}}(f,t). \tag{4.49}$$

We can define the spectrogram $S_{xx}(f,t)$ consisting three auto terms $S_{xx}^{(a)}(f,t)$ and six cross terms $S_{xx}^{(c)}(f,t)$ as follows

$$S_{xx}(f,t) = S_{xx}^{(a)}(f,t) + S_{xx}^{(c)}(f,t) \tag{4.50}$$

where

$$S_{xx}^{(a)}(f,t) = \frac{1}{2T} \sum_{\mathcal{C}=1}^{3} \sum_{n=1}^{N} \mathcal{H}_{\mathcal{C}}^2 \frac{c_n^2}{|k_n|} \left| \triangle \mathrm{Z}_n^{\mathcal{C}}(f,t) \right|^2 \tag{4.51}$$

and

$$S_{xx}^{(c)}(f,t) = \frac{1}{T}\sum_{\mathcal{C}=1}^{3}\sum_{n=1}^{N}\sum_{\substack{m=1\\m\neq n}}^{N}\mathcal{H}_{\mathcal{C}}^{2}\mathrm{Re}\left\{g_n^{\mathcal{C}}(f)g_m^{*\mathcal{C}}(f)\triangle \mathrm{Z}_n^{\mathcal{C}}(f,t)\triangle \mathrm{Z}_m^{*\mathcal{C}}(f,t)\right\} + \frac{1}{T}\sum_{\substack{\mathcal{C}=1\\\mathcal{N}=1\\\mathcal{C}\neq\mathcal{N}}}^{3}\sum_{n=1}^{N}\sum_{\substack{m=1\\m\neq n}}^{N}\mathcal{H}_{\mathcal{C}}\mathcal{H}_{\mathcal{N}}\mathrm{Re}\left\{g_n^{\mathcal{C}}(f)g_m^{*\mathcal{N}}(f)\triangle \mathrm{Z}_n^{\mathcal{C}}(f,t)\triangle \mathrm{Z}_m^{*\mathcal{N}}(f,t)\right\}. \tag{4.52}$$

We now define $g_n^{\mathcal{C}}(f)$ and $\triangle \mathrm{Z}_n^{\mathcal{C}}(f,t)$ for $\mathcal{C}=1,2,3$ as

$$g_n^{\mathcal{C}}(f) = \frac{c_n}{\sqrt{|k_n|}}e^{j\left[(\theta_n+\mathcal{V}_{\mathcal{C}})-\frac{\pi}{k_n}((f+\mathcal{S}_{\mathcal{C}})-f_n)^2\right]} \tag{4.53}$$

$$\triangle \mathrm{Z}_n^{\mathcal{C}}(f,t) = \begin{cases} \mathrm{Z}\left(u_{n\mathcal{C}}^{(+)}\right) - \mathrm{Z}\left(u_{n\mathcal{C}}^{(-)}\right) & \text{if } k_n > 0 \\ 0 & \text{if } k_n = 0 \\ \mathrm{Z}^*\left(u_{n\mathcal{C}}^{(+)}\right) - \mathrm{Z}^*\left(u_{n\mathcal{C}}^{(-)}\right) & \text{if } k_n < 0 \end{cases} \tag{4.54}$$

where

$$u_{n\mathcal{C}}^{\pm} = u_{n\mathcal{C}}^{\pm}(f,t) = \sqrt{\pi\,|k_n|}\left(t \pm \frac{T}{2} - \frac{(f+\mathcal{S}_{\mathcal{C}})-f_n}{k_n}\right). \tag{4.55}$$

For $\mathcal{C}$ ($\mathcal{C}=1,2,3$), the *constant frequency parameter* $\mathcal{S}_{\mathcal{C}} = 0, -\frac{1}{T}, \frac{1}{T}$ and the *time-variant phase parameter* $\mathcal{V}_{\mathcal{C}} = 0, -\frac{2\pi t}{T}$ and, $\frac{2\pi t}{T}$, respectively.

4.2.4 Blackman Window

The Blackman window function with normalised energy is defined as

$$h(t) = \sqrt{\frac{2}{2a_0^2+a_1^2+a_2^2}}\left[a_0 + a_1\cos\left(\frac{2\pi t}{T}\right) + a_2\cos\left(\frac{4\pi t}{T}\right)\right],\ -\frac{1}{T} \le t \le \frac{1}{T} \tag{4.56}$$

using three coefficients (a_0, a_1, a_2) with two place approximations. Figure 4.6 illustrates the Blackman window for the coefficients approximated as $a_0 = 0.42, a_1 = 0.5$ and $a_2 = 0.08$.

The "exact Blackman" window is designed to null out the third and fourth sidelobes, with $a_0 = 7938/18608 \approx 0.42659, a_1 = 9240/18608 \approx 0.49656$, and $a_2 = 1430/18608 \approx 0.076849$ [22]. These coefficients place zeros at the third and fourth side lobes as depicted in Fig. 4.7(b).

The spectrogram of SOC$_i$ Processes using the Blackman Window Function

According to the definition of STFT $X(f,t)$ in equations (4.2) and (4.3), now we directly define the STFT $X(f,t)$ using the Blackman window function $h(t)$ (4.53) for the stationary multipath fading channel which is modelled by a sum of SOC$_i$ processes $\mu(t) = \sum_{n=1}^{N} c_n \exp\{j\,(2\pi f_n t + \theta_n)\}$ as given by

$$X\,(f,t) = \sqrt{\frac{2}{2a_0^2+a_1^2+a_2^2}}\left\{a_0\left[X_1^{Rect}(f,t)\right] + \frac{a_1}{2}\left[X_{2A}^{Rect}(f,t) + X_{2B}^{Rect}(f,t)\right] + \frac{a_1}{2}\left[X_{3A}^{Rect}(f,t) + X_{3B}^{Rect}(f,t)\right]\right\} \tag{4.57}$$

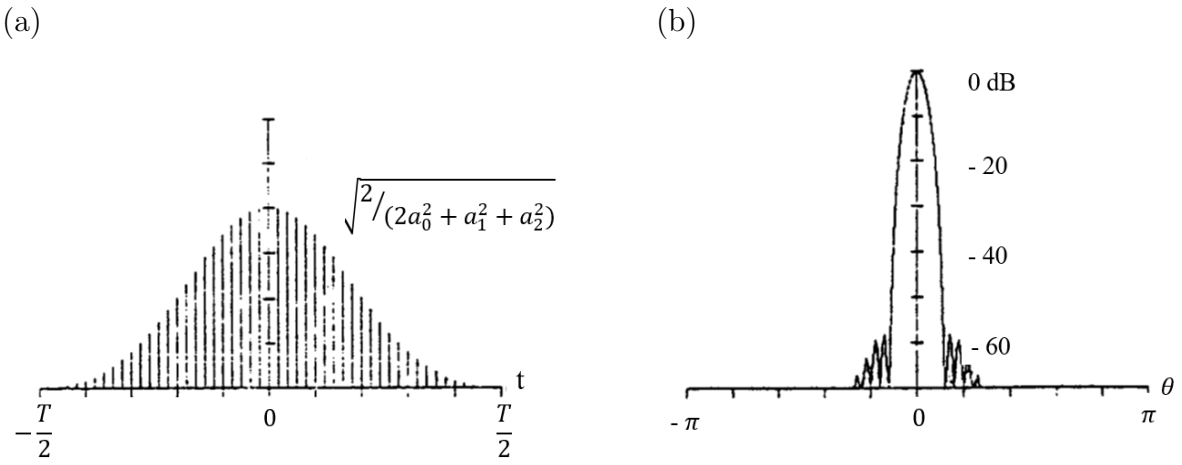

Figure 4.6: (a) Blackman window, and (b) log-magnitude of the transform [22].

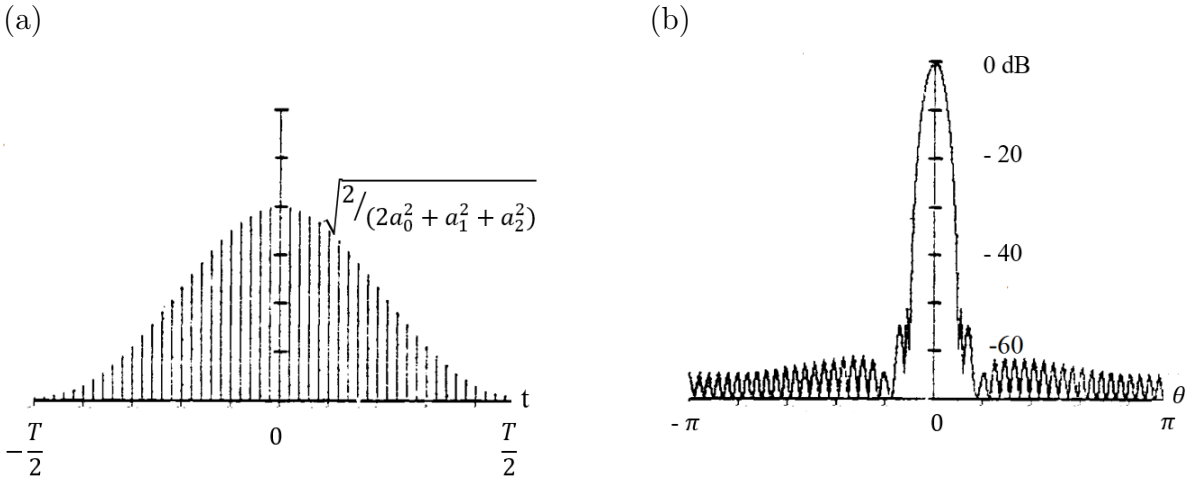

Figure 4.7: (a) Blackman window, and (b) log-magnitude of the transform [22].

The preceding equation can be further reduced as a sum of STFTs $X_{\mathcal{L}}^{Rect}(f,t)$ obtained by the rectangle window function according to

$$X\left(f,t\right)=\sum_{\mathcal{K}=1}^{5}\mathcal{V}_{\mathcal{K}}\left[X_{\mathcal{K}}^{Rect}(f,t)\right] \tag{4.58}$$

where $X_{\mathcal{K}}^{Rect}(f,t)$ for $\mathcal{K}=1,2,...,5$ denotes five STFTs obtained for the SOC_i processes using the rectangle window function and the values of $\mathcal{V}_{\mathcal{K}}$ for $\mathcal{K}=1,2,...,5$ are given as $a_0\sqrt{2/(2a_0^2+a_1^2+a_2^2)}$, $a_1/2\sqrt{2/(2a_0^2+a_1^2+a_2^2)}$, $a_1/2\sqrt{2/(2a_0^2+a_1^2+a_2^2)}$, $a_2/2\sqrt{2/(2a_0^2+a_1^2+a_2^2)}$, and $a_2/2\sqrt{2/(2a_0^2+a_1^2+a_2^2)}$, respectively.

The STFTs $X_{\mathcal{K}}^{Rect}(f,t)$ for $\mathcal{K}=1,2,...,5$ are given by

$$X_{\mathcal{K}}^{Rect}(f,t)=\sqrt{T}\sum_{n=1}^{N}c_n e^{-j(2\pi((f+\mathcal{J}_{\mathcal{K}})-f_n)t-(\theta_n+\mathcal{Y}_{\mathcal{K}}))}\mathrm{sinc}[\pi((f+\mathcal{J}_{\mathcal{K}})-f_n)T] \tag{4.59}$$

for $\mathcal{K}=1,2,...,5$, the *constant frequency parameter* $\mathcal{J}_{\mathcal{K}}=0,-\frac{1}{T},\frac{1}{T},-\frac{2}{T},\frac{2}{T}$ and the *time-variant phase parameter* $\mathcal{Y}_{\mathcal{K}}=0,-\frac{2\pi t}{T},\frac{2\pi t}{T},-\frac{4\pi t}{T},\frac{4\pi t}{T}$, respectively.

The spectrogram $S_{xx}(f,t)$ can be derived by taking the squared magnitude of the $X(f,t)$ as follows:

$$S_{xx}\left(f,t\right)=\left|X\left(f,t\right)\right|^2=\left|\sum_{\mathcal{K}=1}^{5}\mathcal{V}_{\mathcal{K}}\left[X_{\mathcal{K}}^{Rect}(f,t)\right]\right|^2. \tag{4.60}$$

The spectrogram $S_{xx}(f,t)$ consists five auto-terms $S_{xx}^{(a)}(f,t)$ and many cross-terms $S_{xx}^{(c)}(f,t)$ shown as

$$S_{xx}^{(a)}(f,t)=T\sum_{\mathcal{K}=1}^{5}\sum_{n=1}^{N}\mathcal{V}_{\mathcal{K}}^2c_n^2\mathrm{sinc}^2[\pi((f+\mathcal{J}_{\mathcal{K}})-f_n)T] \tag{4.61}$$

and

$$\begin{aligned}S_{xx}^{(c)}(f,t)=2T\sum_{\mathcal{K}=1}^{5}\sum_{n=1}^{N}\sum_{\substack{m=1\\m\neq n}}^{N}\mathcal{V}_{\mathcal{K}}^2\mathrm{Re}\left\{\mu_n\left(t\right)\mu_m^*\left(t\right)\right\}\mathrm{sinc}[\pi((f+\mathcal{J}_{\mathcal{K}})-f_n)T]\cdot\\ \mathrm{sinc}[\pi((f+\mathcal{J}_{\mathcal{K}})-f_m)T]+\\ 2T\sum_{\substack{\mathcal{K}=1\\\mathcal{N}=1\\\mathcal{K}\neq\mathcal{N}}}^{5}\sum_{n=1}^{N}\sum_{\substack{m=1\\m\neq n}}^{N}\mathcal{V}_{\mathcal{K}}\mathcal{V}_{\mathcal{N}}\mathrm{Re}\left\{\mu_n\left(t\right)\mu_m^*\left(t\right)\right\}\mathrm{sinc}[\pi((f+\mathcal{J}_{\mathcal{K}})-f_n)T]\cdot\\ \mathrm{sinc}[\pi((f+\mathcal{J}_{\mathcal{N}})-f_m)T].\end{aligned} \tag{4.62}$$

With this results, we define the spectrogram $S_{xx}(f,t)$ of sum of SOC_i processes as

$$S_{xx}\left(f,t\right)=S_{xx}^{(a)}(f,t)+S_{xx}^{(c)}(f,t). \tag{4.63}$$

The spectrogram of SOC_h Processes using the Blackman Window Function

The STFT $X(f,t)$ using the energy normalised Blackman window function for the SOC_h processes $\mu(t)=\sum_{n=1}^{N}c_n\exp\left\{j\left(2\pi\left(f_nt+\frac{k_n}{2}t^2\right)+\theta_n\right)\right\}$, can be directly expressed according to

$$X\left(f,t\right)=\sum_{\mathcal{Z}=1}^{5}\zeta_{\mathcal{Z}}\left[X_{\mathcal{Z}}^{Rect}(f,t)\right] \tag{4.64}$$

where $X_{\mathcal{Z}}^{Rect}(f,t)$ for $\mathcal{Z}=1,2,...,5$ represents three STFTs obtained for SOC_h Processes using the rectangle function and the values of $\zeta_{\mathcal{Z}}$ for $\mathcal{Z}=1,2,...,5$, are given as $a_0\sqrt{2/(2a_0^2+a_1^2+a_2^2)}$, $a_1/2\sqrt{2/(2a_0^2+a_1^2+a_2^2)}$, $a_1/2\sqrt{2/(2a_0^2+a_1^2+a_2^2)}$, $a_2/2\sqrt{2/(2a_0^2+a_1^2+a_2^2)}$, and $a_2/2\sqrt{2/(2a_0^2+a_1^2+a_2^2)}$, respectively.

We now define $X_{\mathcal{Z}}^{Rect}(f,t)$ for $\mathcal{Z}=1,2,...,5$ in closed form as [see (4.13)]

$$X_{\mathcal{Z}}^{Rect}(f,t)=\frac{1}{\sqrt{2T}}\sum_{n=1}^{N}g_n^{\mathcal{Z}}(f)\triangle\mathrm{Z}_n^{\mathcal{Z}}(f,t) \tag{4.65}$$

where

$$g_n^{\mathcal{Z}}(f)=\frac{c_n}{\sqrt{|k_n|}}e^{j\left[(\theta_n+\varphi_{\mathcal{Z}})-\frac{\pi}{k_n}((f+\varepsilon_{\mathcal{Z}})-f_n)^2\right]} \tag{4.66}$$

$$\triangle\mathrm{Z}_n^{\mathcal{Z}}(f,t)=\begin{cases}\mathrm{Z}\left(u_{n\mathcal{Z}}^{(+)}\right)-\mathrm{Z}\left(u_{n\mathcal{Z}}^{(-)}\right) & \text{if } k_n>0\\ 0 & \text{if } k_n=0\\ \mathrm{Z}^*\left(u_{n\mathcal{Z}}^{(+)}\right)-\mathrm{Z}^*\left(u_{n\mathcal{Z}}^{(-)}\right) & \text{if } k_n<0\end{cases} \tag{4.67}$$

$$u_{n\mathcal{Z}}^{\pm}=u_{n\mathcal{Z}}^{\pm}(f,t)=\sqrt{\pi\left|k_n\right|}\left(t\pm\frac{T}{2}-\frac{(f+\varepsilon_{\mathcal{Z}})-f_n}{k_n}\right). \tag{4.68}$$

For $\mathcal{Z}$ ($\mathcal{Z}=1,2,...,5$), the *constant frequency parameter* $\varepsilon_{\mathcal{Z}}=0,-\frac{1}{T},\frac{1}{T},-\frac{2}{T},\frac{2}{T}$ and the *time-variant phase parameter* $\varphi_{\mathcal{Z}}=0,-\frac{2\pi t}{T},\frac{2\pi t}{T},-\frac{4\pi t}{T},\frac{4\pi t}{T}$, respectively.

We can define the spectrogram $S_{xx}(f,t)$ consisting five auto terms $S_{xx}^{(a)}(f,t)$ and many cross terms $S_{xx}^{(c)}(f,t)$ as follows

$$S_{xx}\left(f,t\right)=S_{xx}^{(a)}(f,t)+S_{xx}^{(c)}(f,t) \tag{4.69}$$

where

$$S_{xx}^{(a)}(f,t)=\frac{1}{2T}\sum_{\mathcal{Z}=1}^{5}\sum_{n=1}^{N}\zeta_{\mathcal{Z}}^2\frac{c_n^2}{|k_n|}\left|\triangle\mathrm{Z}_n^{\mathcal{Z}}(f,t)\right|^2 \tag{4.70}$$

and

$$\begin{aligned}S_{xx}^{(c)}(f,t)=&\frac{1}{T}\sum_{\mathcal{Z}=1}^{5}\sum_{n=1}^{N}\sum_{\substack{m=1\\m\neq n}}^{N}\mathcal{P}_{\mathcal{Z}}^2\mathrm{Re}\left\{g_n^{\mathcal{Z}}(f)g_m^{*\mathcal{Z}}\left(f\right)\triangle\mathrm{Z}_n^{\mathcal{Z}}(f,t)\triangle\mathrm{Z}_m^{*\mathcal{Z}}(f,t)\right\}+\\&\frac{1}{T}\sum_{\substack{\mathcal{Z}=1\\\mathcal{N}=1\\\mathcal{Z}\neq\mathcal{N}}}^{5}\sum_{n=1}^{N}\sum_{\substack{m=1\\m\neq n}}^{N}\mathcal{R}_{\mathcal{Z}}\mathcal{R}_{\mathcal{N}}\mathrm{Re}\left\{g_n^{\mathcal{Z}}(f)g_m^{*\mathcal{N}}\left(f\right)\triangle\mathrm{Z}_n^{\mathcal{Z}}(f,t)\triangle\mathrm{Z}_m^{*\mathcal{N}}(f,t)\right\}.\end{aligned} \tag{4.71}$$

4.2.5 Gaussian Window

The Gaussian function is widely known as "bell curve" which is a smooth and non-zero function, in which the Fourier transform is also a Gaussian function. Since the Gaussian function extends to infinity, for most of applications, Gaussian function is either be truncated at the ends of the window, or windowed with another zero-ended window function.

Figure 4.8 (a) and (b) illustrates the Gaussian window and its log magnitude of the transformation.

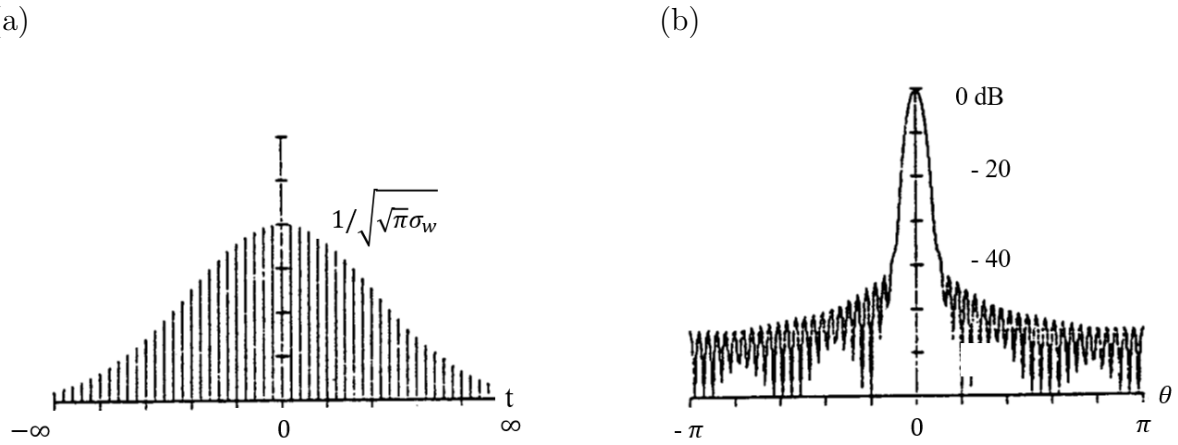

Figure 4.8: (a) Gaussian window, and (b) log-magnitude of the transform [22].

It is evident that [8] is an innovative approach of using Gaussian window function for the definition of the spectrogram of non-stationary channels by using massive MIMO techniques. As given in this paper, energy normalized positive Gaussian window function is defined as

$$h(t) = \frac{1}{\sqrt{\sqrt{\pi}\sigma_w}} e^{-\frac{t^2}{2\sigma_w^2}}, \quad -\infty \leq t \leq \infty \tag{4.72}$$

where σ_w is a real-valued constant called as the *window spread parameter* and window length $T = 2\sigma_w$. A closed form solution for the STFT is presented in [8] for MIMO channel. We directly adopt the (18) of [8] and with simple mathematical manipulations, now we redefine the STFT for single bounce, single transmitter and single receiver channel which is modelled as sum of a SOC_h process as

$$X(f,t) = \frac{e^{-j2\pi ft}}{\sqrt{\sqrt{\pi}\sigma_w}} \sum_{n=1}^{N} G\left(f, f_n(t), \sigma_x^2\right) h_n(t) \tag{4.73}$$

with the Gaussian function $G(f, f_n(t), \sigma_x^2))$ with mean $f_n(t)$ and variance σ_x^2 is given by

$$G\left(f, f_n(t), \sigma_x^2\right)) = \frac{1}{\sqrt{2\pi}\sigma_x} e^{-} \frac{\left(f - f_n(t)\right)^2}{2\sigma_x^2} \tag{4.74}$$

where

$$\sigma_x^2 = \frac{1 - j2\pi\sigma_w^2 k_n}{\left(2\pi\sigma_w\right)^2} \tag{4.75}$$

and

$$h_n(t) = c_n e^{j\left[2\pi\left(f_n t + \frac{k_n}{2}t^2\right)+\theta_n\right]}. \tag{4.76}$$

Th spectrogram $S_{xx}(f,t)$ can be written as a sum of an auto-term $S_{xx}^{(a)}(f,t)$and a cross-term $S_{xx}^{(c)}(f,t)$ as follows [8]

$$S_{xx}(f,t) = S_{xx}^{(a)}(f,t) + S_{xx}^{(c)}(f,t) \tag{4.77}$$

where

$$S_{xx}^{(a)}(f,t) = \sum_{n=1}^{N} c_n^2 G\left(f, f_n(t), \sigma_n^2\right) \tag{4.78}$$

$$S_{xx}^{(c)}(f,t) = \frac{1}{\sqrt{\pi}\sigma_w} \sum_{n=1}^{N} \sum_{\substack{m=2 \\ m>n}}^{N} \mathrm{Re}\left\{G\left(f, f_n(t), \sigma_x^2\right) G^*\left(f, f_n(t), \sigma_x^2\right) h_n(t) h_n^*(t)\right\} \tag{4.79}$$

and it denotes that the auto-term equals sum of Gaussian functions which is weighted by the squared path gain c_n^2, and the variance σ_n^2 of the Gaussian function is given as

$$\sigma_n^2 = \frac{1 + \left(2\pi\sigma_w^2 k_n\right)^2}{2\left(2\pi\sigma_w\right)^2}. \tag{4.80}$$

The optimum value of the window spread parameter σ_w is obtained by computing $d\sigma_n^2/d\sigma_w^2$ of variance σ_n^2 and setting result to zero [8]. Thus, we can now define the optimum value of the window length T_{opt} according to

$$T_{opt} = 2\sigma_{w,opt} = \frac{1}{\sqrt{2\pi\left|k_n\right|}}. \tag{4.81}$$

When the MS is moves with constant speed $\mathrm{v}(t) = \mathrm{v}_0$ i.e., $k_n = 0$, the spectrogram of SOC_h processes reduces to the spectrogram of SOC_i processes.

4.3 Chapter Summary

This chapter started with the basic definition of the spectrogram. Thereafter, the spectrogram was defined by using different window functions. The STFT obtained by multiplying the $\mu(t)$ with the rectangle window, is used to define the STFTs for Hann, Hamming and Blackman window types, which is a novel approach to this research work. The work is extended to define the spectrogram for stationary and non-stationary multipath mobile radio channels. The concept of optimum window length is introduced for the spectrogram which defined using the Gaussian window function.

Further, it has been showed that the spectrogram can be separated as an auto-term and a cross-term for all window types. For the spectrogram obtained using the rectangle, Hann, Hamming, Blackman and Gaussian windows, the auto-term $S_{xx}^{(a)}(f,t)$ of the spectrogram for a sum of SOC_i and sum of SOC_h processes are independent of the phases θ_n. However, the cross-term $S_{xx}^{(c)}(f,t)$ depends on the θ_n.

Chapter 5

Numerical Analysis of RSE-to-Car Communication Channels

This chapter presents the numerical analysis of RSE-to-car communication channels for braking situations by using the concept of the spectrogram. The braking situations are categorised as comfort and emergency braking actions.

5.1 Introduction

In this chapter, we present two types of braking manoeuvres. A normal braking action, so-called "comfort braking action", where the vehicle is brought comfortably to the standstill and in an emergency stop, so-called "emergency braking action", where the vehicle is brought to a complete standstill as quickly as possible [14].

According to the braking manoeuvres, different propagation scenarios wre defined and for each propagation scenario, it has been considered a multipath channel consisting of $N = 10$ components. The path gains c_n was computed according to the extended method of exact Doppler spread (EMEDS) as follows [26]

$$c_n = \sigma_0 \sqrt{\frac{2}{N}}. \tag{5.1}$$

The variance σ^2 was set to unity while the phases were considered as random and uniformly distributed over the interval $(0, 2\pi)$.

It has been considered a low speed $\mathrm{v}(t)$ of the MS and a comfortable deceleration parameter a_0 for the analysis of the "comfort braking action" scenario. For the "emergency braking action" scenario it has been considered higher speeds of the MS and different values for the deceleration parameter a_0.

5.2 Spectrogram Analysis Under Low Mobile Velocity and Designed Braking Distances

When the MS travelled in low speed, it has been assumed that the AOA is time-invariant. Thus, it was set $\gamma_n = 0$ in (3.7) and the time-variant AOA $\alpha_n(t) = \alpha_n$. Therefore, we only considered the first term of the k_n which is depicted in (3.12), i.e., $k_n = f_{\max}\left[(a_0/\mathrm{v}_0)\cos\left(\alpha_n - \alpha_v\right)\right]$.

The initial speed v_0 and the initial AOM α_v of the MS are considered as 36 km/h and 0 rad/s, respectively. The carrier frequency f_0 was chosen to be 5.9 GHz, which corresponds to a wave length of $\lambda_0 = 5.0812$ cm. Furthermore, it has been found the initial maximum Doppler frequency $f_{max}(0)$ as 197 Hz. Unless otherwise stated, it was assumed that the deceleration parameter $\alpha_0 = 3.4\ m/s^2$.

According to (3.22) the braking distance d was found as $d = 14.86$ m ≈ 15 m which was tallied with the result given in Table. 3.1. It was assumed that $S_n(n = 0, 1, ..., 10)$ scatterers are located on a ring with ring radius $R = 100$ m. The braking time has been set as 3 s. A complete description of the trajectory is given in Chapter 3 [see Fig. 3.4].

It is vital to recognise individual scatterers which are responsible for each multipath of the channel. Figure 5.1 illustrates the scatterers' positions and the respective narrow band signal of the multipath channel plotted in the spectrogram.

(a)

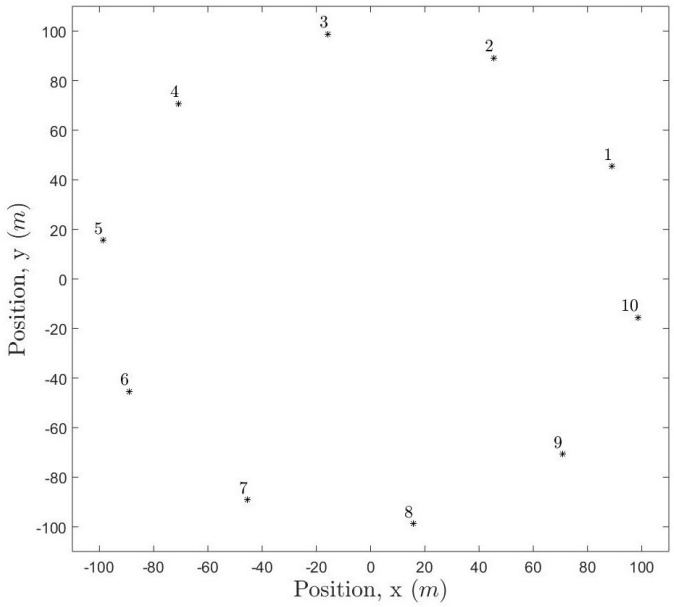

(b)

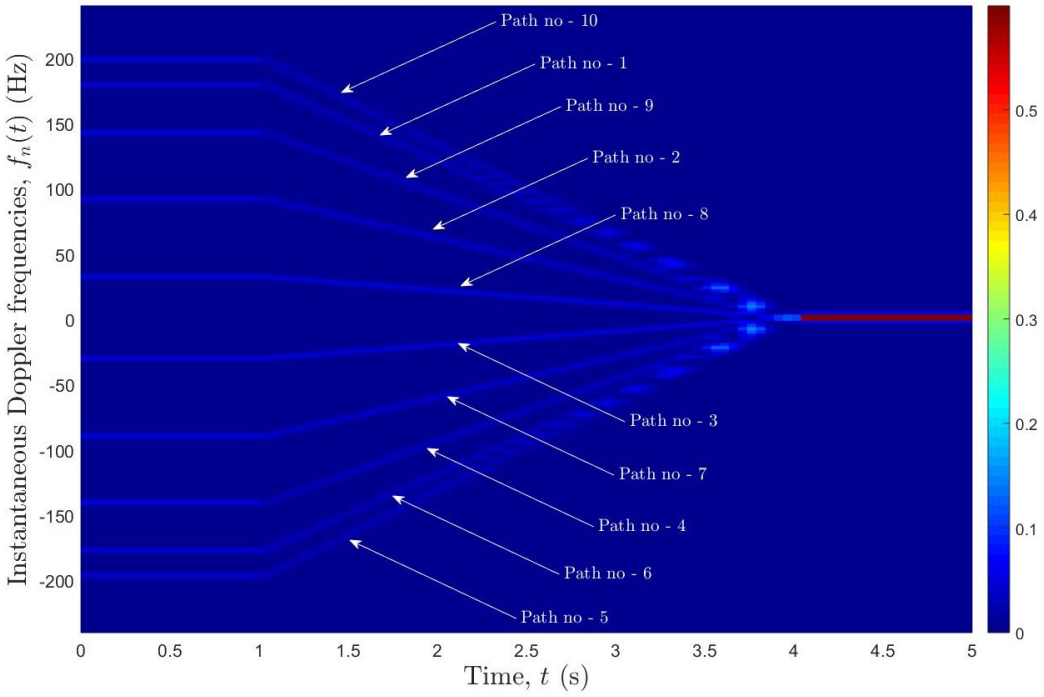

Figure 5.2: (a) Locations of the scatterers, and the named multi-paths in the spectrogram $S_{xx}(f,t)$.

The optimum window lengths T_{opt} were found by substituting the values of k_n in (4.81). The optimum window lengths are shown in Table 5.1.

Table 5.1: Optimum window lengths T_{opt}.

Path	1	2	3	4	5	6	7	8	9	10
α_n	$\frac{3\pi}{20}$	$\frac{7\pi}{20}$	$\frac{11\pi}{20}$	$\frac{15\pi}{20}$	$\frac{19\pi}{20}$	$\frac{23\pi}{20}$	$\frac{27\pi}{20}$	$\frac{31\pi}{20}$	$\frac{35\pi}{20}$	$\frac{39\pi}{20}$
k_n	-59.4	-30.3	10.4	47.1	65.8	59.4	30.3	-10.4	-47.1	-65.8
$\sigma_{opt,w}$(s)	0.05	0.07	0.12	0.06	0.05	0.05	0.07	0.12	0.06	0.05
T_{opt} (s)	0.10	0.15	0.25	0.12	0.10	0.10	0.15	0.25	0.12	0.10

The optimum window lengths given in Table. 5.1 are optimised for Gaussian window function. However, for rectangle window functions, very small window lengths results in large cross-terms of the spectrogram [6]. Hence, $T_{opt} = 0.15$ (s) and $T_{opt} = 0.25$ (s) were used to define the spectrogram $S_{xx}(f,t)$ for different types of window functions considered in Chapter 4 and the result is illustrated in Fig. 5.3.

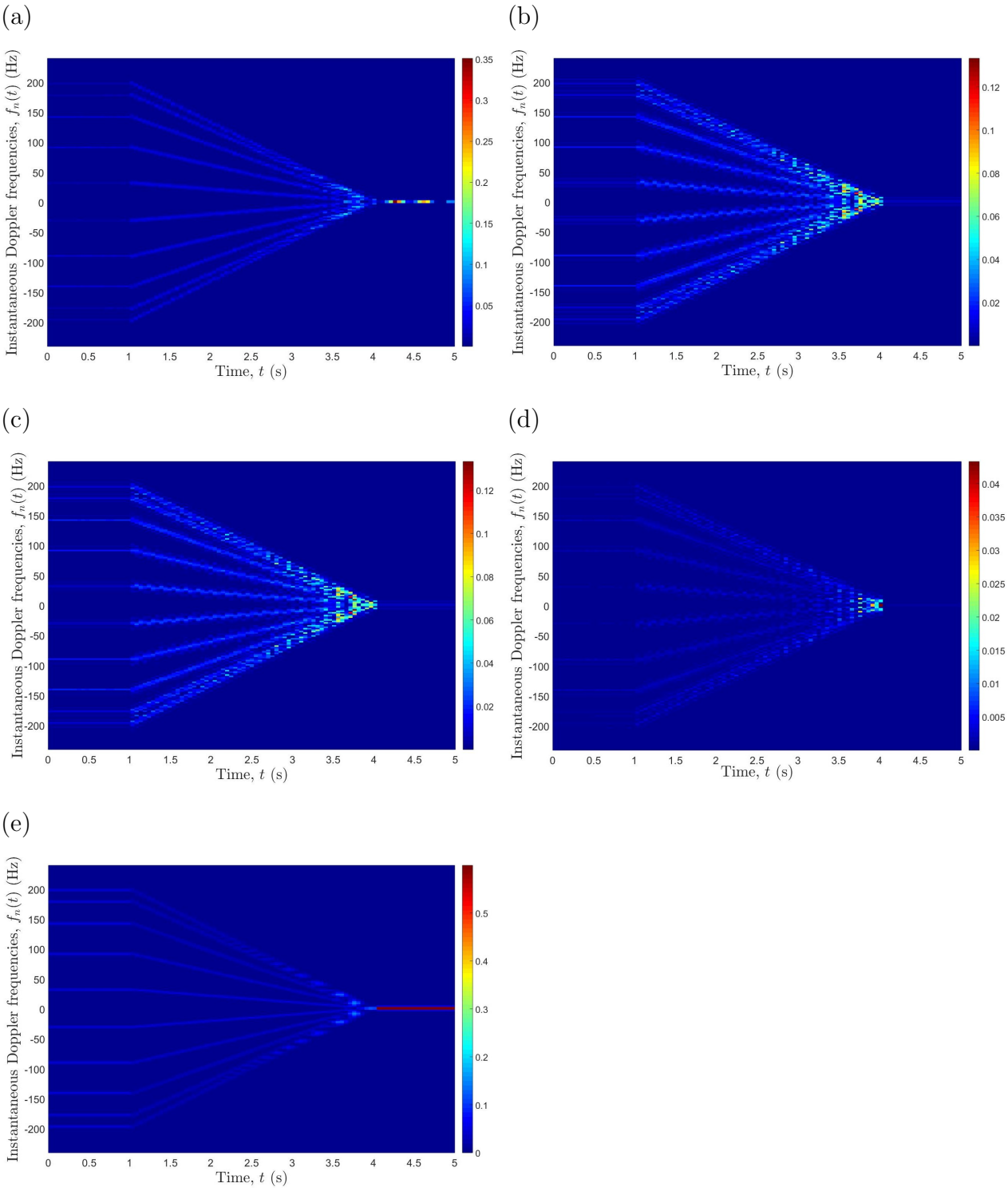

Figure 5.3: Spectrogram $S_{xx}(f,t)$ of $\mu(t)$ using (a) Rectangle window, (b) Hann window, (c) Hamming window, (d) Blackman window, and (e) Gaussian window for $T = 0.15$ s.

The analytical results are shown in the Fig. 5.3 has been verified by the simulation results as shown in the Fig. 5.4.

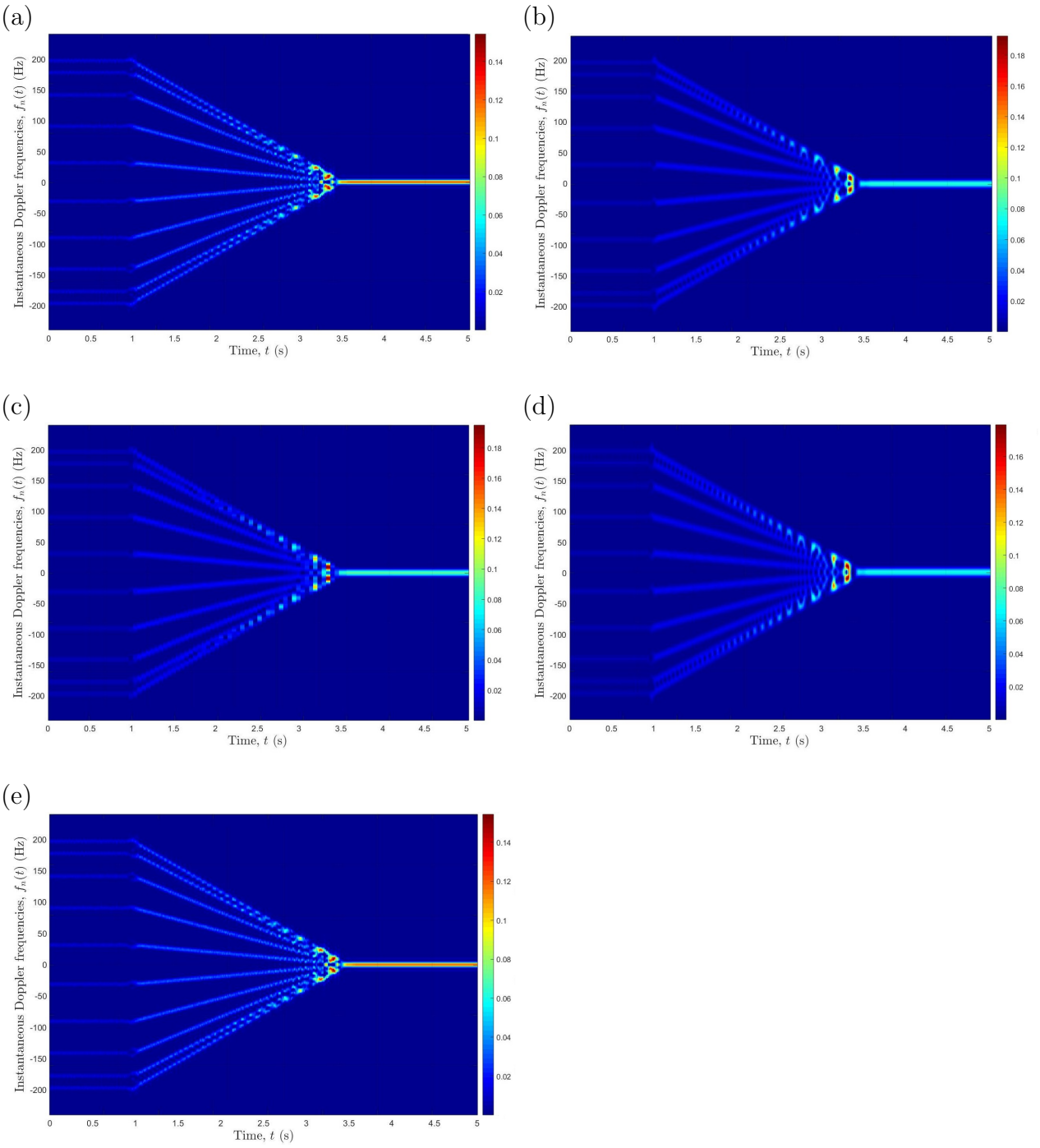

Figure 5.4: Simulation result of the spectrogram $S_{xx}(f,t)$ of $\mu(t)$ using (a) Rectangle window, (b) Hann window, (c) Hamming window, (d) Blackman window, and (e) Gaussian window for $T = 0.15$ s.

Analogously, Fig. 5.5 illustrates the analytical solution of the spectrogram $S_{xx}(f,t)$ of $\mu(t)$ using different window types with window length $T = 0.25$ s.

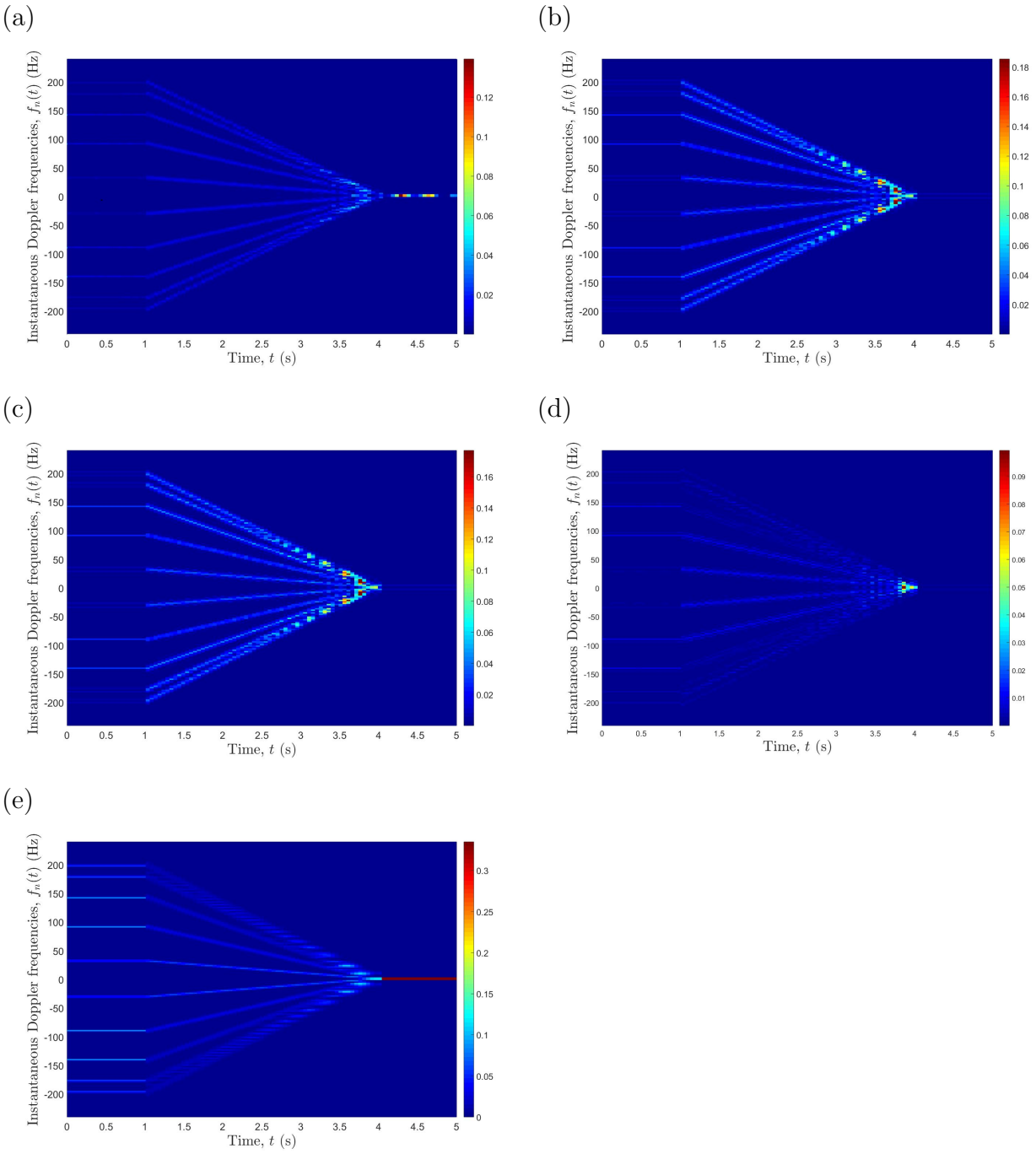

Figure 5.5: Spectrogram $S_{xx}(f,t)$ of $\mu(t)$ using (a) Rectangle window, (b) Hann window, (c) Hamming window, (d) Blackman window, and (e) Gaussian window for $T = 0.25$ s.

5.2.1 Selection of the Best Spectrogram Window Type

For the comparison of the window types, firstly, we consider the instantaneous power $P_n(t)$ of the spectrogram at a fixed time t. Figure 5.6 plots the instantaneous power $P_n(t)$ against instantaneous Doppler frequency $f_n(t)$ for the auto-term of spectrogram $S_{xx}(f,t)$. Without the cross-terms, Fig. 5.6 impressively shows a clear separation between instantaneous Doppler frequency lobes and almost negligible distortions at the forming-up places of the lobes. Hence, this method is well suitable for the comparison of

the spectrogram of different window types, where we expect the window function used to generate the spectrogram which proves a good agreement with Fig. 5.6, is the best window type for the given scenario.

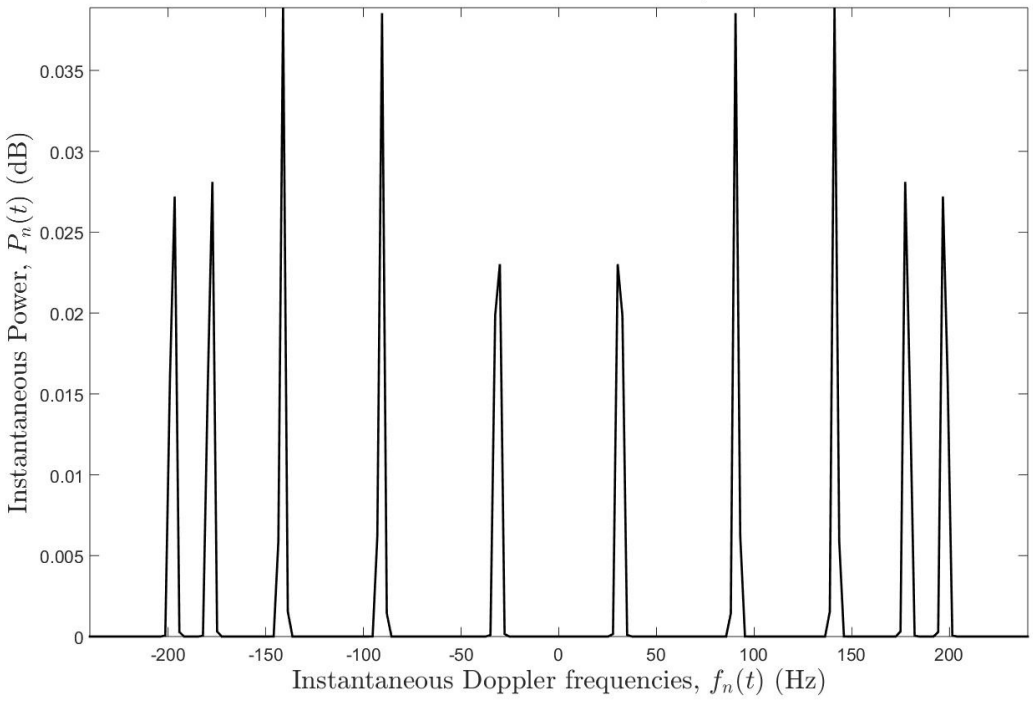

Figure 5.6: Instantaneous power $P_n(t)$ vs instantaneous Doppler frequencies $f_n(t)$ of the auto-term of the spectrogram $S_{xx}^{(a)}(f,t)$.

Figure 5.7 illustrates the instantaneous power $P_n(t)$ vs instantaneous Doppler frequencies $f_n(t)$ for the spectrogram $S_{xx}(f,t)$ (consisting the auto-term $S_{xx}^{(a)}(f,t)$ and the cross-term $S_{xx}^{(c)}(f,t)$) generated using different window types for the stationary and non-stationary motion period of the MS and for the window length $T = 0.15$ s.

(a) Rectangle Window: Stationary

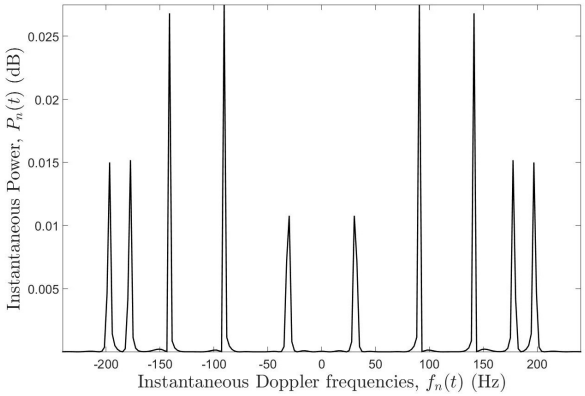

(b) Rectangle Window: Non-Stationary

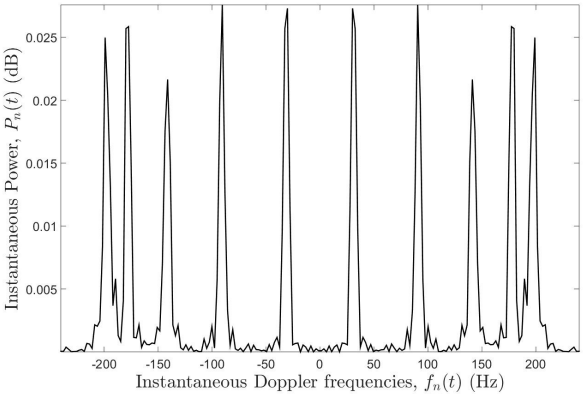

(c) Hann Window: Stationary

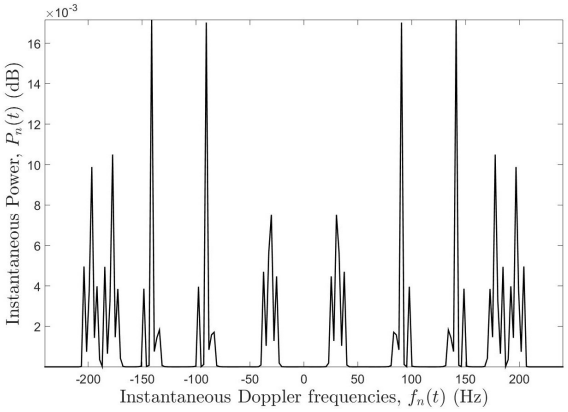

(d) Hann Window: Non-Stationary

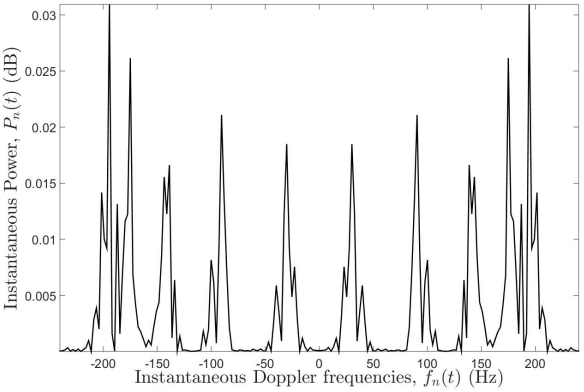

(e)Hamming Window: Stationary

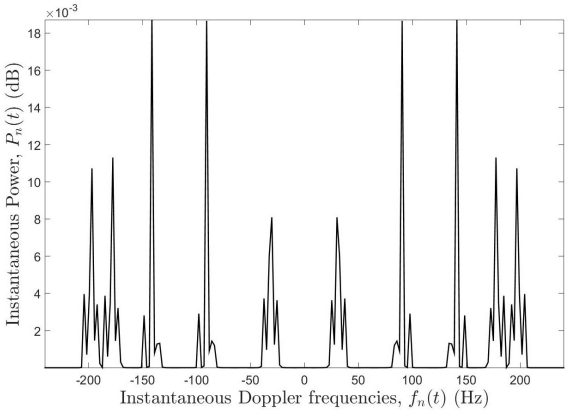

(f) Hamming Window: Non-Stationary

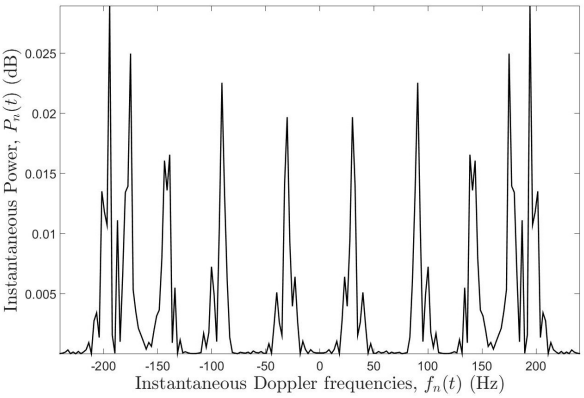

(g) Blackman Window: Stationary

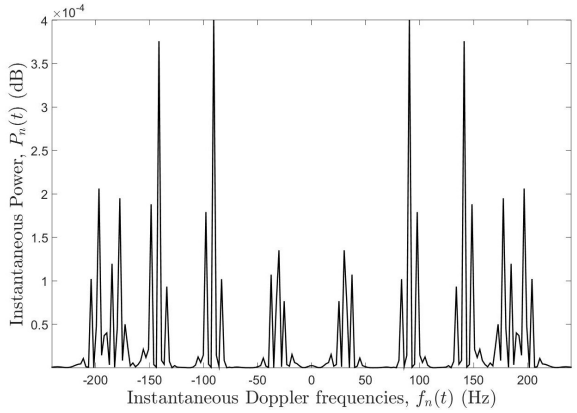

(h) Blackman Window: Non-Stationary

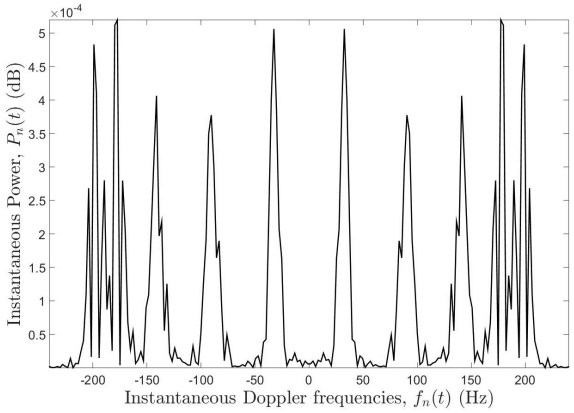

(i) Gaussian Window: Stationary

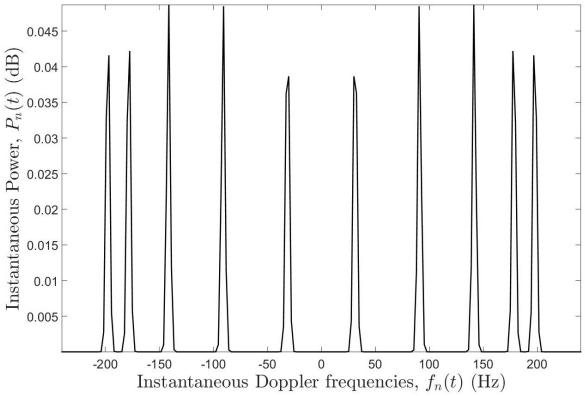

(j) Gaussian Window: Non-Stationary

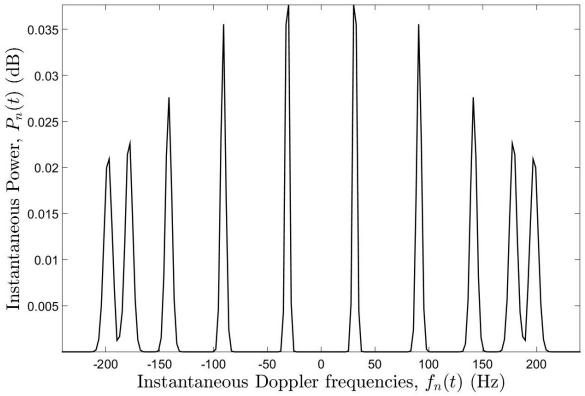

Figure 5.7: Instantaneous power $P_n(t)$ vs instantaneous Doppler frequency $f_n(t)$ for the spectrogram $S_{xx}(f,t)$ generated using different window types for the stationary and non-stationary period and for $T = 0.15$ s.

Figure 5.8 illustrates the instantaneous power $P_n(t)$ vs instantaneous Doppler frequencies $f_n(t)$ for the spectrogram $S_{xx}(f,t)$ generated using different window types for the stationary and non-stationary motion period and for $T = 0.25$ s.

(a) Rectangle Window: Stationary

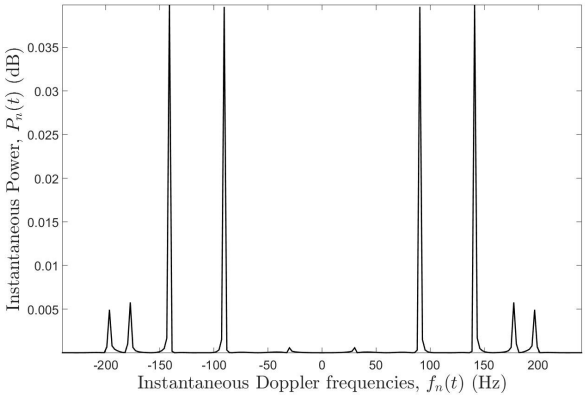

(b) Rectangle Window: Non-Stationary

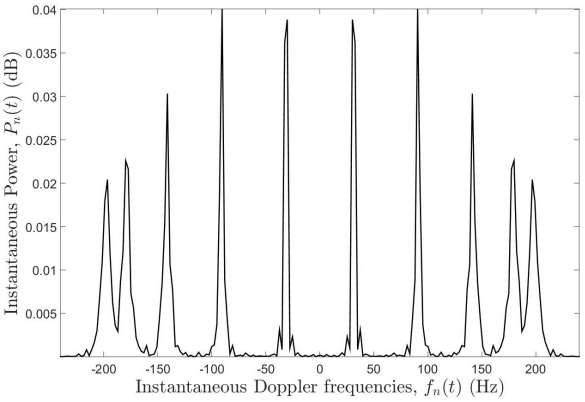

(c) Hann Window: Stationary

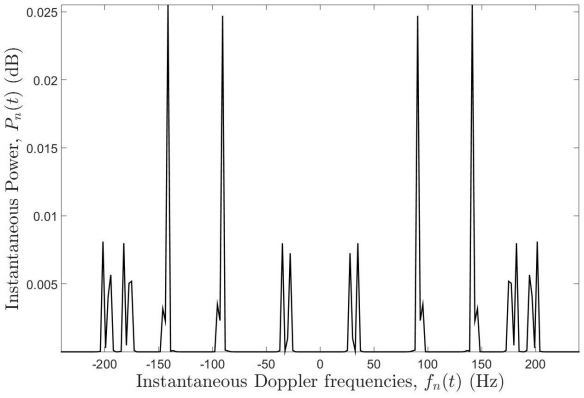

(d) Hann Window: Non-Stationary

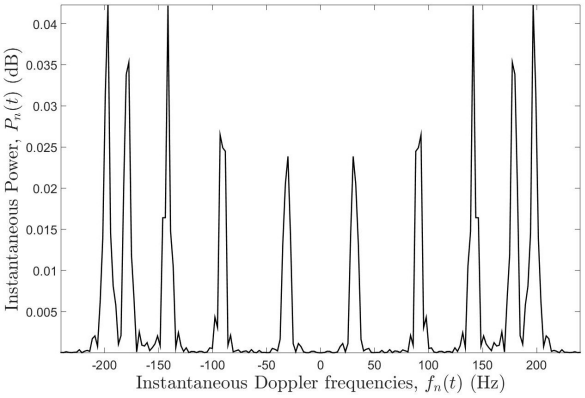

(e)Hamming Window: Stationary

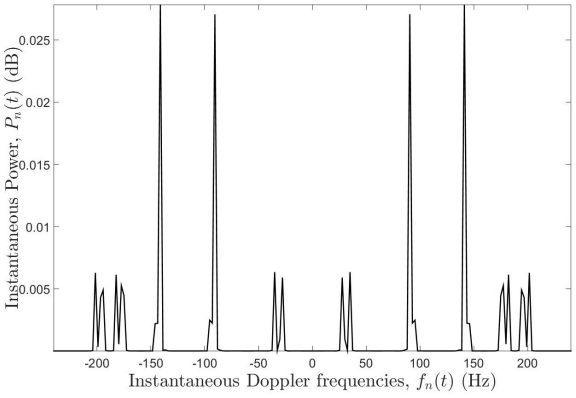

(f) Hamming Window: Non-Stationary

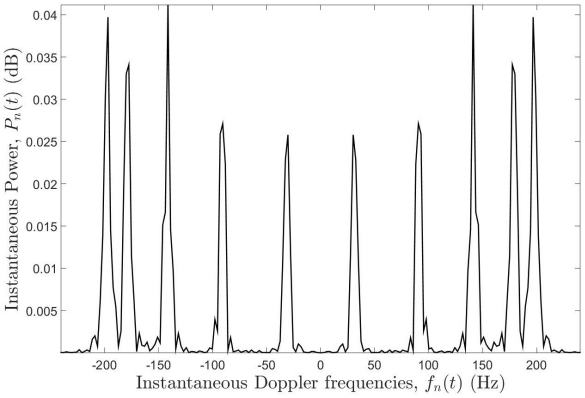

(g) Blackman Window: Stationary

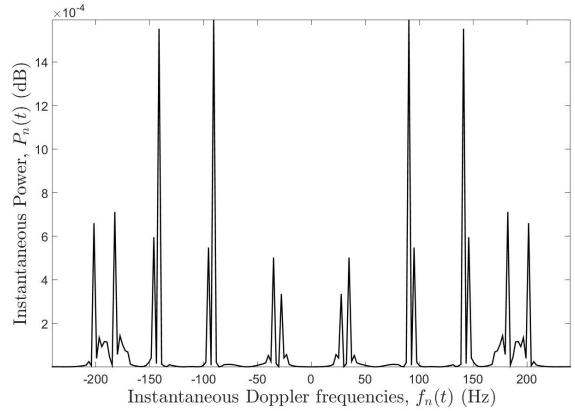

(h) Blackman Window: Non-Stationary

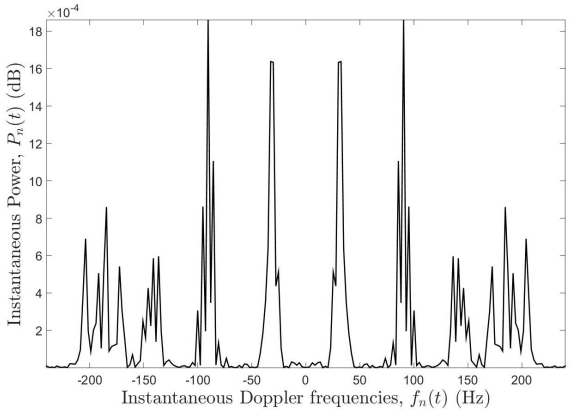

(i) Gaussian Window: Stationary

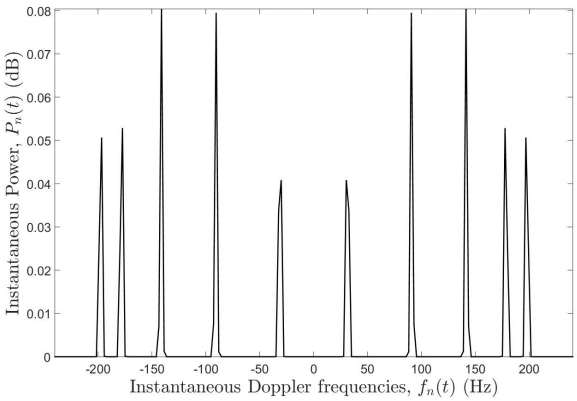

(j) Gaussian Window: Non-Stationary

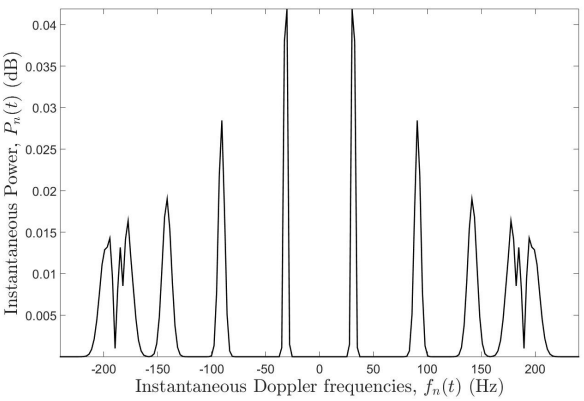

Figure 5.8: Instantaneous power $P_n(t)$ vs instantaneous Doppler frequency $f_n(t)$ for the spectrogram $S_{xx}(f,t)$ generated using different window types for the stationary and non-stationary period and $T = 0.25$ s.

We note from the visual inspection of Figs. 5.7 and 5.8 that the Gaussian window function improved the spectrogram. This result has been further strengthened by analysing the time-variant average Doppler shift and the time-variant Doppler spread.

From the theory developed before, it is seen that the time-variant Doppler shift $f_n(t)$ is defined as a linear Doppler frequency model as stated in (3.8) and the time-variant average Doppler shift $B_f^{(1)}(t)$ and time-variant Doppler spread $B_f^{(2)}(t)$ are obtained according to [see (2.2)]

$$B_f^{(1)}(t) = \frac{\sum_{n=1}^{N} c_n^2 f_n(t)}{\sum_{n=1}^{N} c_n^2} \tag{5.2}$$

and

$$B_f^{(2)}(t) = \sqrt{\frac{\sum_{n=1}^{N} c_n^2 f_n^2(t)}{\sum_{n=1}^{N} c_n^2} - \left(B_f^{(1)}(t)\right)^2}. \tag{5.3}$$

Alternatively, we can compute the estimated time-variant average Doppler shift

$B_\mu^{(1)}(t)$ and the estimated time-variant Doppler spread $B_\mu^{(2)}(t)$ of the time-variant signal $\mu(t)$ by means of the spectrogram $S_{xx}(f,t)$. The first moment of the spectrogram $S_{xx}(f,t)$ defines the estimated time-variant average Doppler shift $B_\mu^{(1)}(t)$, and the square root of the second central moment of the spectrogram $S_{xx}(f,t)$ defines the estimated time-variant Doppler spread $B_\mu^{(2)}(t)$. This alternate approach leads to

$$B_\mu^{(1)}(t) = \frac{\int_{-\infty}^{\infty} f S_{xx}(f,t) df}{\int_{-\infty}^{\infty} S_{xx}(f,t) df} \tag{5.4}$$

and

$$B_\mu^{(2)}(t) = \sqrt{\frac{\int_{-\infty}^{\infty} \left(f - B_\mu^{(1)}(t)\right)^2 S_{xx}(f,t) df}{\int_{-\infty}^{\infty} S_{xx}(f,t) df}}. \tag{5.5}$$

A similar approach has presented in [25] for a stationary channel.

In this case, the reference model consists of (5.2) and (5.3) whereas the estimated model consists of (5.4) and (5.5).

Figure 5.9 shows the time-variant Doppler spread of the reference and estimated model for $T = 0.15$ s as described in (5.3) and (5.5), respectively.

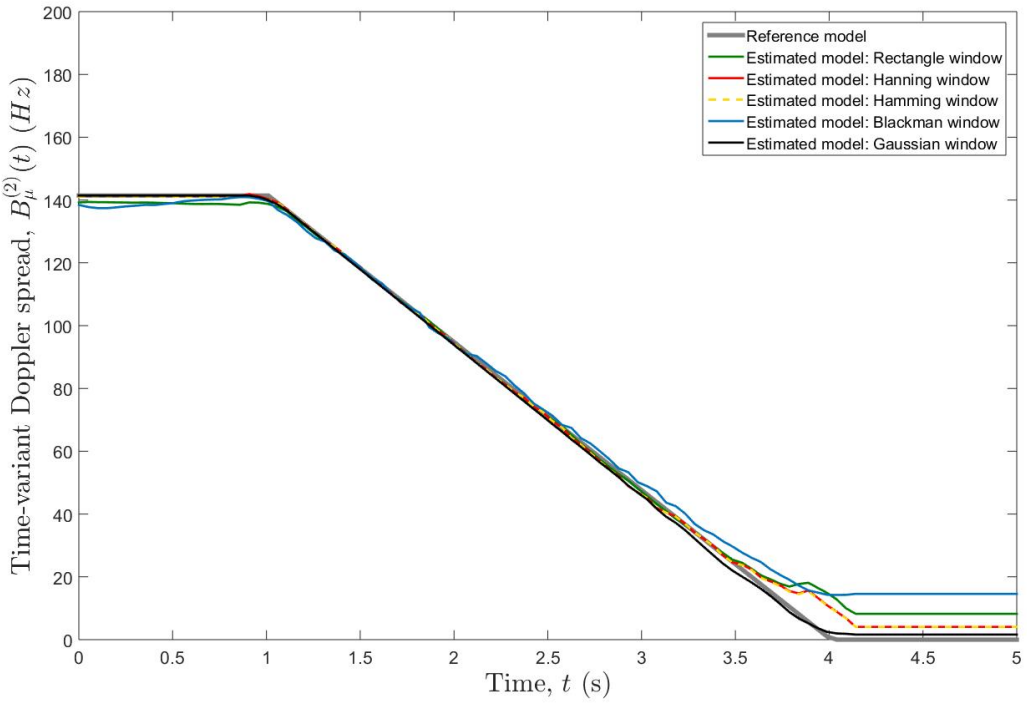

Figure 5.9: Time-variant Doppler spread $B_\mu^{(2)}(t)$ for process $\mu(t)$ obtained by the reference model and the estimated model for $T = 0.15$ s.

Analogously, Fig. 5.10 illustrates the time-variant Doppler spread of reference and simulation model for $T = 0.25$ s.

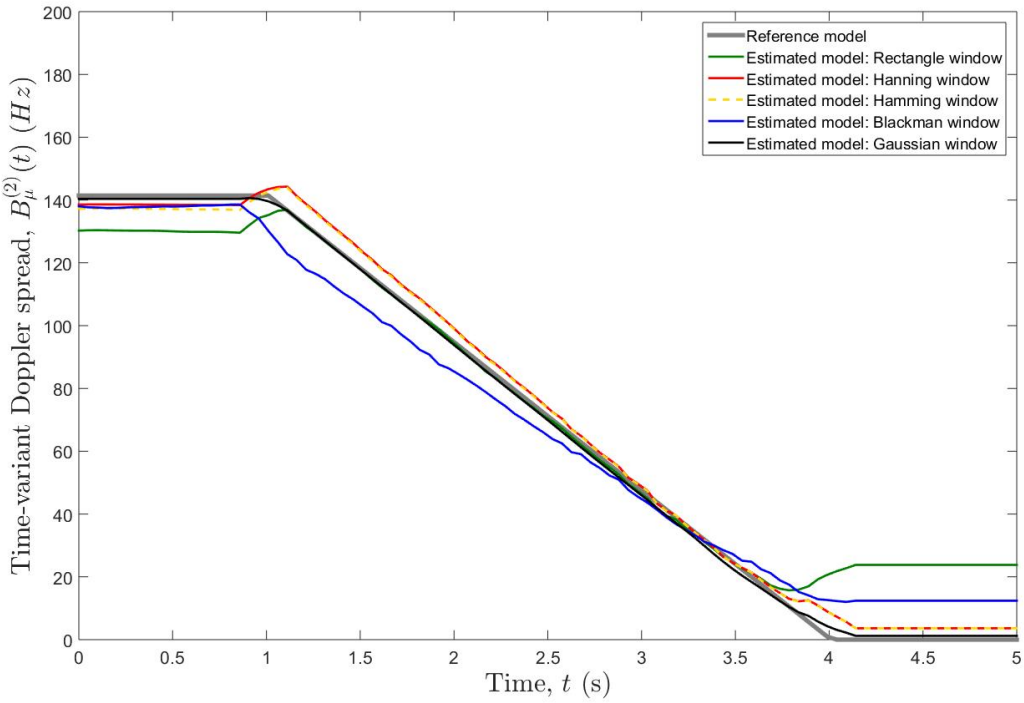

Figure 5.10: Time-variant Doppler spread $B_\mu^{(2)}(t)$ for process $\mu(t)$ obtained by the reference model and the estimated model.

We note from the inspection of Fig. 5.9 and 5.10 that our analytical models with different window types line up sufficiently with the reference model. Again, the best agreement between the reference model and the estimated model of time-variant Doppler spread is observed for the Gaussian window.

With reference to the observations made for instantaneous power $P_n(t)$ against Doppler frequency $f_n(t)$ and time-variant Doppler spread $B_\mu^{(2)}(t)$, we now decide that the Gaussian window function is as the best window type to generate the spectrogram w.r.t the given scenario.

Hence, we have strictly considered the Gaussian window function as the window function to generate the spectrogram for the analysis hereafter in this chapter.

5.2.2 Spectrogram Optimization

The spectrogram $S_{xx}(f,t)$ can be optimised by reducing the cross-term $S_{xx}^{(c)}(f,t)$ of the spectrogram. We now consider different methods which help to reduce the cross-term $S_{xx}^{(c)}(f,t)$.

Phase Averaging

The first method uses the phase average technique to reduce the spectral interferences caused by the cross-term by averaging the spectrogram over random phases $(\theta)_n$.

if the phases $(\theta)_n$ are uniformly distributed $(0, 2\pi]$ independent and identically distributed (i.i.d.) random variables, then phase average causes the expected value of the cross-term to vanish i.e., $E\left\{S_{xx}^{(c)}(f,t)\right\}\big|_{\theta_n} = 0$.

Figure 5.11 illustrates the Spectrogram$S_{xx}(f,t)$, auto-term $S_{xx}^{(c)}(f,t)$, cross-term $S_{xx}^{(c)}(f,t)$ and the averaged (100 rounds) spectrogram, auto and cross-terms of SOC_h process $\mu(t)$ for Gaussian window with window size of $T = 0.15$ s.

(a) Spectrogram $S_{xx}(f,t)$

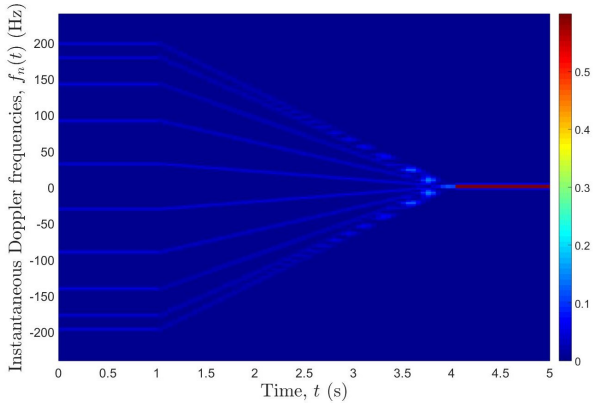

(b) Averaged $S_{xx}(f,t)$

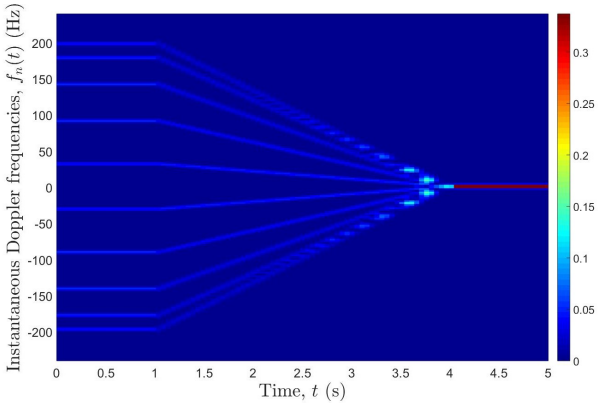

(c) Auto-Term $S_{xx}^{(a)}(f,t)$

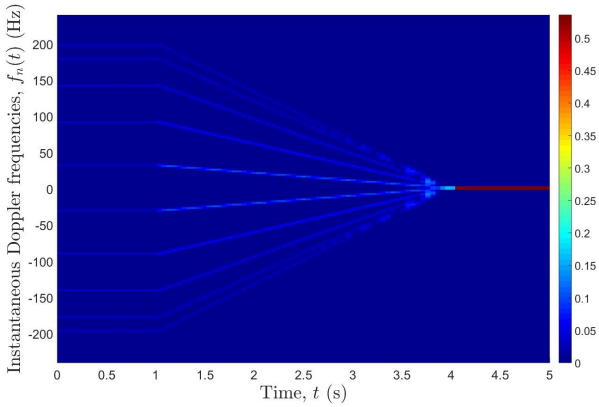

(d) Averaged Auto-Term $S_{xx}^{(a)}(f,t)$

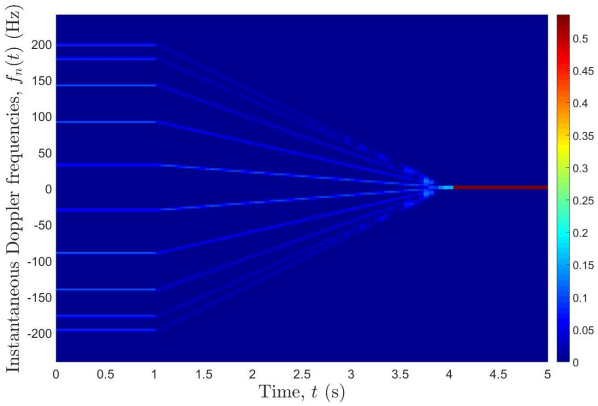

(e) Cross-Term $S_{xx}^{(c)}(f,t)$

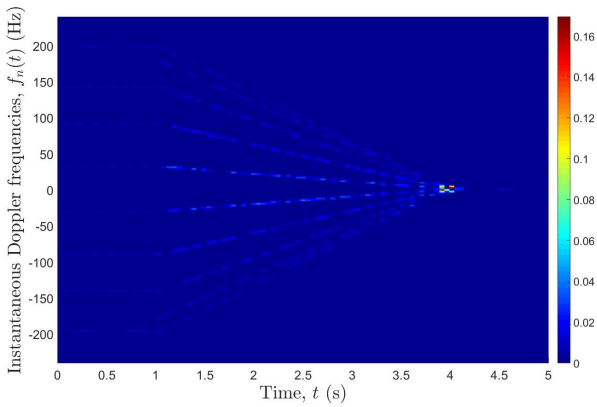

(f) Averaged Cross-Term $S_{xx}^{(c)}(f,t)$

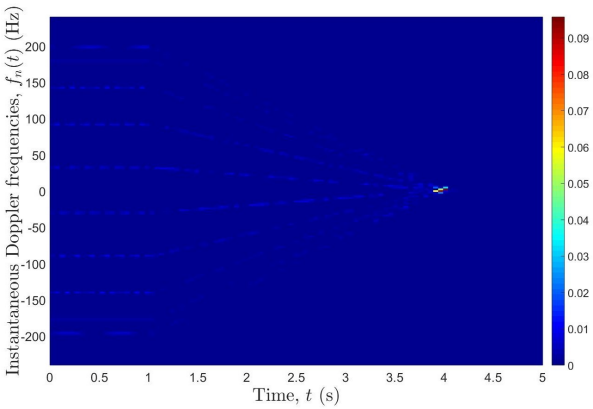

Figure 5.11: (a) Spectrogram $S_{xx}(f,t)$, (b) averaged $S_{xx}(f,t)$, (c) auto-term $S_{xx}^{(a)}(f,t)$, (d) averaged $S_{xx}^{(a)}(f,t)$, (e)cross-term $S_{xx}^{(c)}(f,t)$, and (f) averaged $S_{xx}^{(c)}(f,t)$ of process $\mu(t)$ for $N = 10$, Gaussian window size of $T = 0.15$ s and the scatterers are located on a ring.

Figure 5.11 impressively shows that the phase averaging has reduced the cross-term

significantly whilst apparently improved the spectrogram $S_{xx}(f,t)$ and the auto-term of the spectrogram $S_{xx}^{(a)}(f,t)$.

Finding the Optimum window length

The spectrogram $S_{xx}(f,t)$ is highly sensitive to the window length T. The span of the side lobes increases with a large window length, while a smaller window length reduces the number of samples required for a better frequency/time resolution. Thus, a large value of the window length increases the frequency resolution, however, reduces the resolution in time and vice versa. Hence, it is vital to select the optimum window length for a better optical resolution of the spectrogram of the time-variant signal $\mu(t)$.

With reference to the different values of k_n, optimised window lengths T_{opt} of Gaussian window function were found according to the (4.81) and as shown in Table 5.1. For the selection of best optimum window length, the estimated Doppler power spread was computed for each optimum window length and compared it with the reference model [see (5.3)] as shown in Fig. 5.13. As it is readily apparent in the graph, time-variant Doppler spread obtained by the Gaussian window function with optimum window length $T_{opt} = 0.25$ s provides excellent accordance between the reference model and the estimated model.

(a)

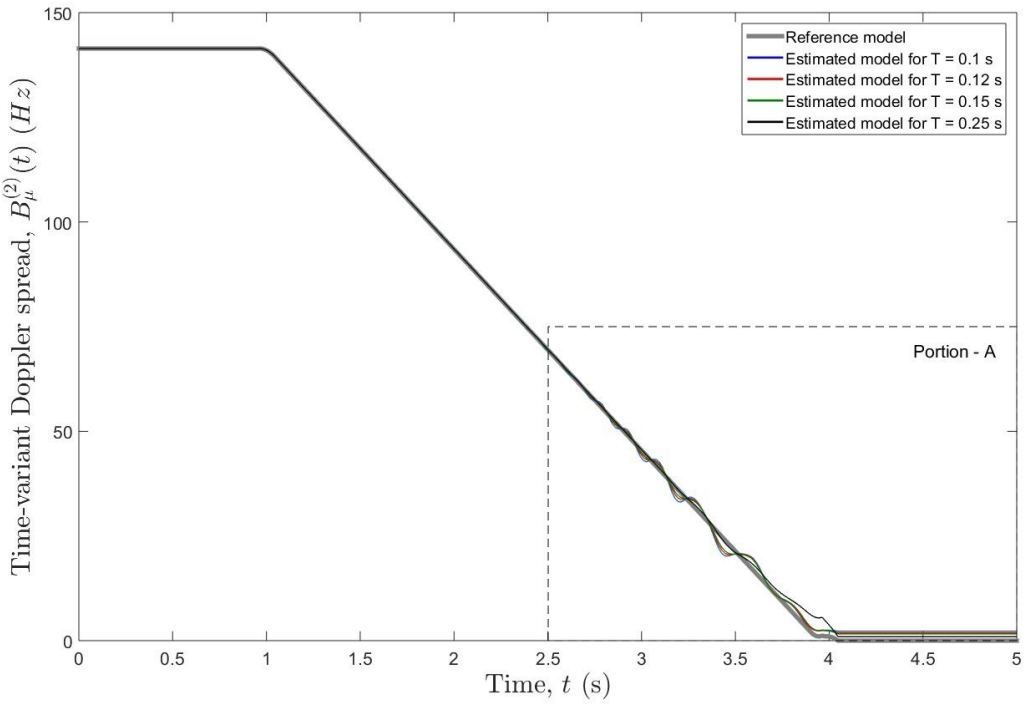

(b) Enlarged view of portion A

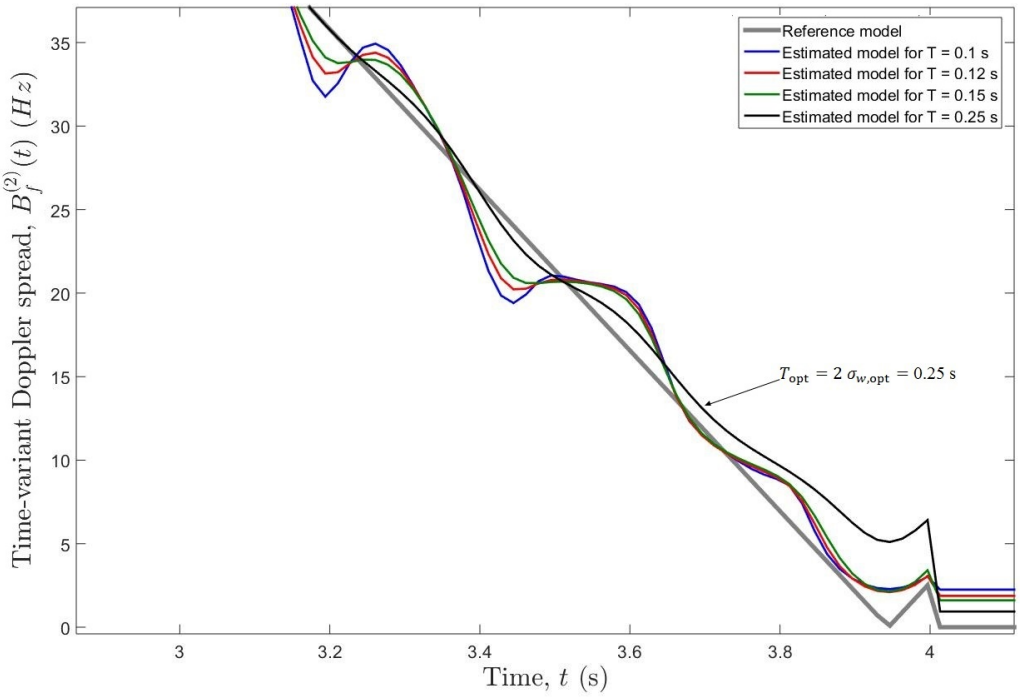

Figure 5.13: (a) Time-variant Doppler spread $B_{\mu}^{(2)}(t)$, and (b) enlarged view of $B_{\mu}^{(2)}(t)$ for process $\mu(t)$ obtained by the reference model and the estimated model for different values of optimum window lengths T_{opt} of the Gaussian window function.

5.3 Spectrogram Analysis for Emergency Braking Situations

Higher deceleration values are obvious at higher speeds which is due to the fact that braking is more effective in high speeds [14]. Therefore, for the analysis of the scenario of deceleration in emergency stops we now consider higher speeds of the MS as shown in Table 5.2. The data shown in Table 5.2 is based on the actual trials conducted by the Trafitec, Denmark [14]. The trials were conducted under different conditions of roads (wet or dry), speeds, car sizes, tyre types (summer or winter) and with different braking behaviour of drivers (professional or non-professional drivers). However, for our analysis, it suffices to consider the average deceleration when at different speeds (80 km/h, 110 km/h and, 130 km/h) of a small car (Fiat and Opel) with summer tyres on dry roads driven by a professional driver. Further, we assumed that the vehicle was driven at a constant speed for 1 s before applying the brakes.

The higher speeds of the MS result in considerable change in the AOA as shown in Fig. 5.14. Therefore, we have considered that the AOA is a time-variant. The time-variant AOA $\alpha_n(t)$ has two definitions, the exact model and approximated model as shown in (3.4) and (3.5), respectively. By considering the total travelling distance of the MS, the ring radius of the scatterers was set to 150 m.

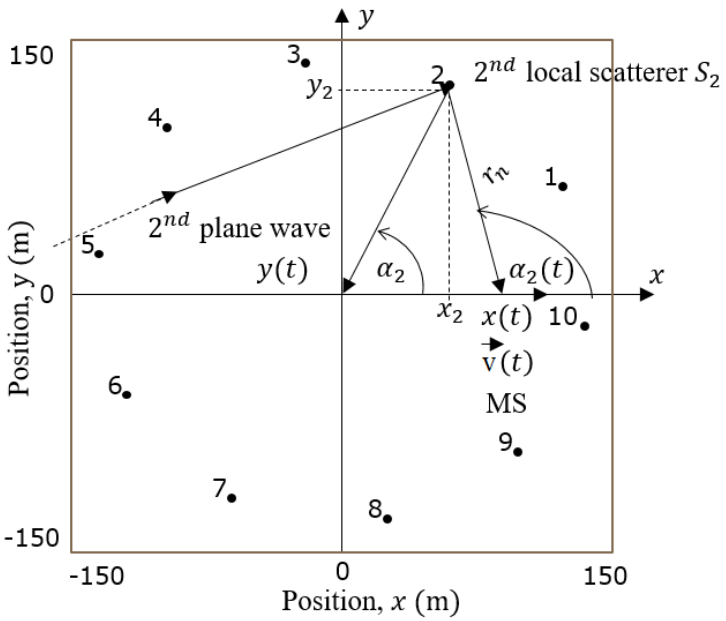

Figure 5.14: A multipath propagation scenario in which the MS travels with time-variant velocity $\vec{V}(t)$.

Table 5.2: Average deceleration, braking distances, and braking time for emergency braking situations.

Speed (km/h)	Speed (m/s)	Deceleration (m/s^2)	Braking distance (m)	Braking time (s)	f_{max} (Hz)
80	22.2	8.1	30	2.7	444
110	30.5	8.3	56.8	3.7	610
130	36.1	8.6	76.6	4.2	722

Table 5.3 illustrates the optimum window lengths of the Gaussian window function for the new scenario.

Table 5.3: Optimum window lengths T_{opt} for emergency braking situations.

Ini. speed	80 km/h									
k_n	-158.62	-116.06	-10.04	102.37	159.53	140.01	50.16	-68.77	-145.68	-161.80
T_{opt} (s)	0.06	0.07	0.25	0.08	0.06	0.07	0.11	0.10	0.07	0.06
Ini. speed	110 km/h									
k_n	-181.81	-170.11	-45.94	94.78	163.12	140.14	30.05	-118.57	-189.37	-168.27
T_{opt} (s)	0.06	0.06	0.12	0.08	0.06	0.07	0.15	0.07	0.06	0.06
Ini. speed	130 km/h									
k_n	-206.61	-220.23	-73.54	92.37	168.85	143.50	17.21	-161.21	-232.69	-176.74
T_{opt} (s)	0.06	0.05	0.09	0.08	0.06	0.07	0.19	0.06	0.05	0.06

The window length of the Gaussian window function was set to 0.06 s. The initial AOM α_v was chosen to be 0 rad/s.

Firstly, it has been considered the approximated model of the time-variant AOA $\alpha_n(t)$ and the resulted approximated time-variant Doppler frequencies given as [see Eq.(3.5)-(3.13)]

$$\alpha_n(t) \approx \alpha_n + \gamma_n t \tag{5.6}$$

$$f_n(t) = f_n + k_n t \tag{5.7}$$

and

$$k_n = f_{\max}\left[\frac{a_0}{\mathrm{v}_0}\cos(\alpha_n - \alpha_v) - \gamma_n \sin(\alpha_n - \alpha_v)\right]. \tag{5.8}$$

When the MS travels at a constant speed, the acceleration parameter $a_0 = 0$, and large changes in time-variant AOA results in $\gamma_n \neq 0$ and $k_n \neq 0$. Hence, the channel exhibits non-stationarity when in a constant speed of the MS. The new speed profile is shown in the Fig. 5.15 for the initial speed of v(t) = 80 km/h.

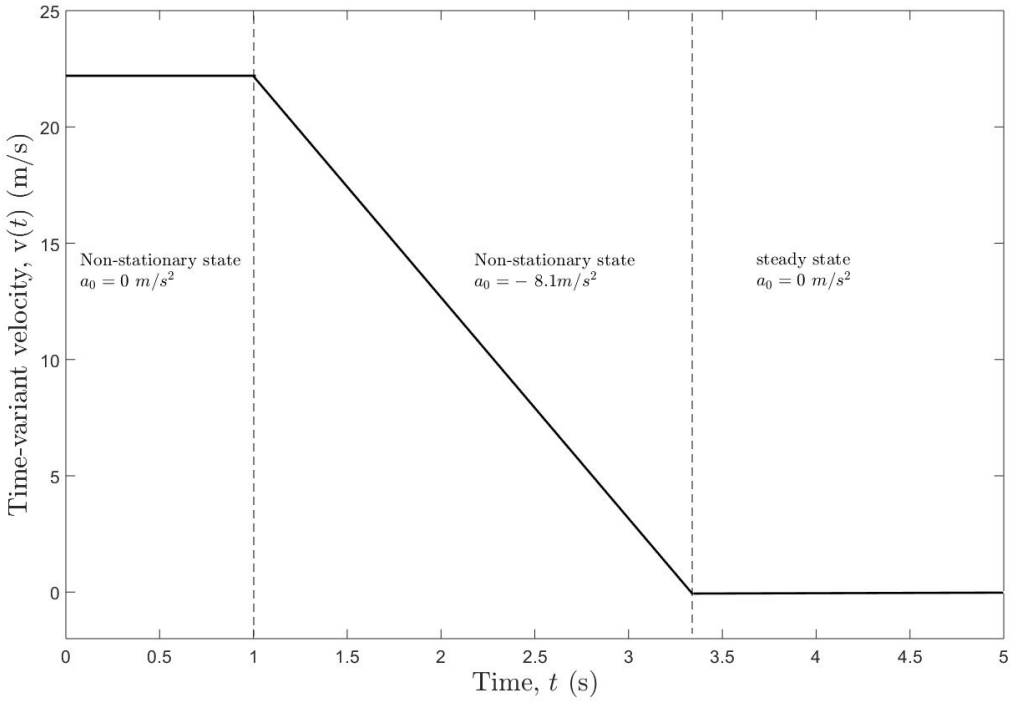

Figure 5.15: The speed profile of the MS for emergency braking situations.

Figure 5.16 illustrates the spectrogram for emergency braking conditions w.r.t. Table 5.2.

(a) v(t) = 80 km/h

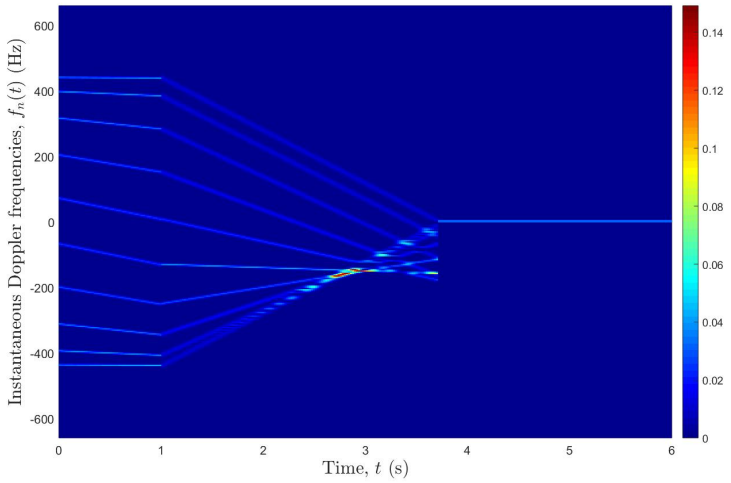

(b) v(t) = 110 km/h

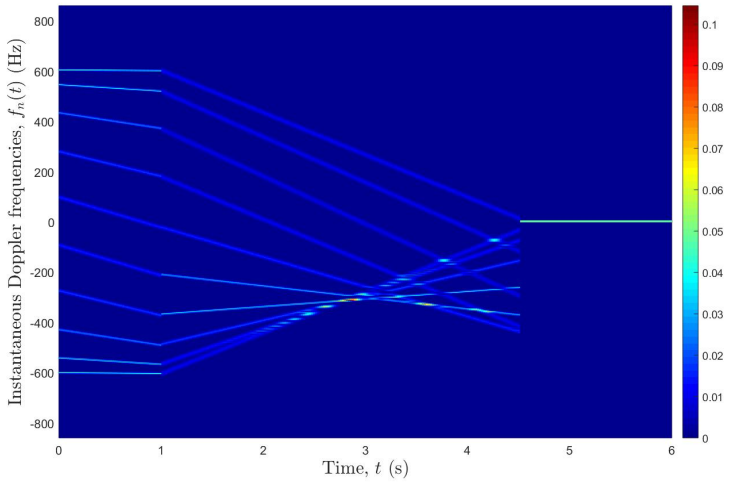

(c) v(t) = 130 km/h

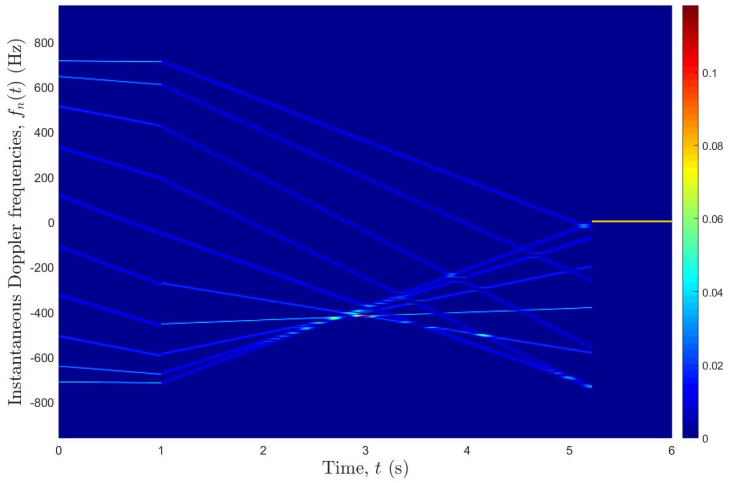

Figure 5.16: Spectrogram $S_{xx}(f,t)$ of process $\mu(t)$ for (a) v(t) = 80 km/h (b) v(t) = 110 km/h and, (c) v(t) = 130 km/h, using the approximated model for AOA and Gaussian window size of $T = 0.06$ s.

As a consequence of the approximation made in (5.6), it is readily apparent in Fig. 5.16, the approximated time-variant AOA $\alpha_n(t)$ and the approximated time-variant Doppler frequency $f_n(t)$ models caused an error in the spectrogram for given MS speeds. Further, it is evident that the error is huge for higher speeds of the MS. Hence, the approximated Doppler frequency model is not suitable for the analysis of this scenario.

Now we consider the exact time-variant AOA $\alpha_n(t)$ and exact time-variant Doppler frequency $f_n(t)$ models. The exact model for time-variant AOA $\alpha_n(t)$ is defined as [see (3.4)]

$$\alpha_n(t) = \arctan\left(\frac{y_n - y(t)}{x_n - x(t)}\right) \tag{5.9}$$

and the exact model of the time-variant Doppler frequency $f_n(t)$ is given as [see (3.4)]

$$f_n(t) = f_{\max}(t) \,.\, \cos(\alpha_n(t) - \alpha_v). \tag{5.10}$$

Figure 5.17 illustrates the spectrogram for data given in Table 5.2, using the exact models of $\alpha_n(t)$ and $f_n(t)$.

Further, it is important to analyse the time-variant Doppler spread using the spectrogram of exact model of $\alpha_n(t)$ and $f_n(t)$. Figure 5.18 shows the time-variant Doppler spread of the reference and estimated model for $T = 0.06$ s, $T = 0.07$ s, and $T = 0.08$ s for the above explained scenario [see (5.3) and (5.5)]. With reference to this figure, the time-variant Doppler spread of the estimated model follows closely that of the reference model for the lowest speed of the MS. A deviation from the reference model is observed for the higher speeds of the MS.

(a) v(t) = 80 km/h

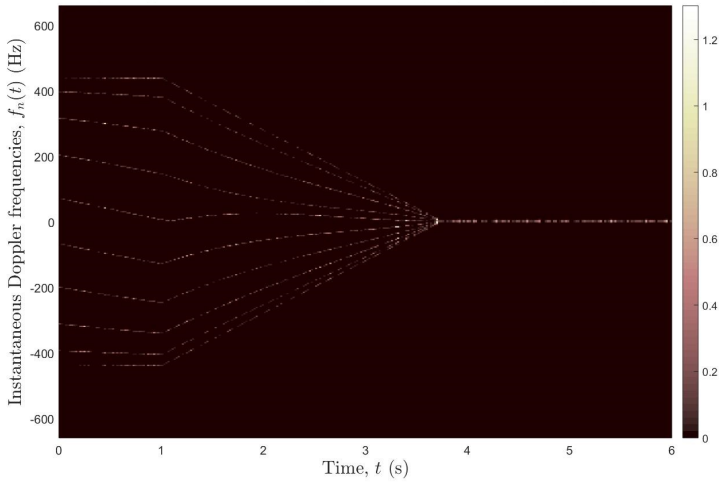

(b) v(t) = 110 km/h

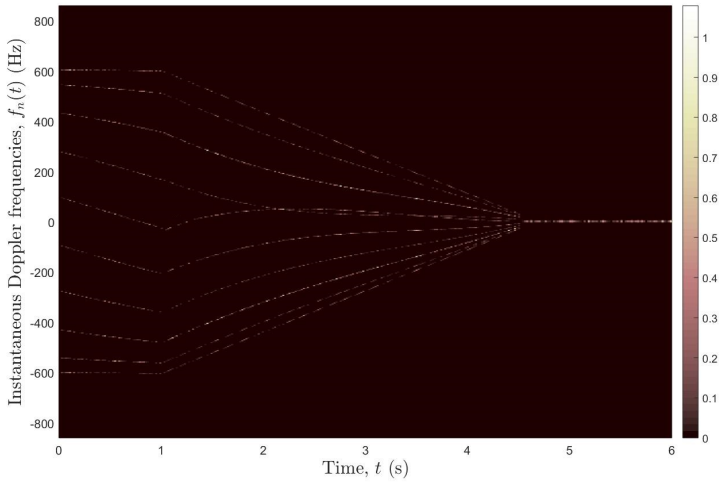

(c) v(t) = 130 km/h

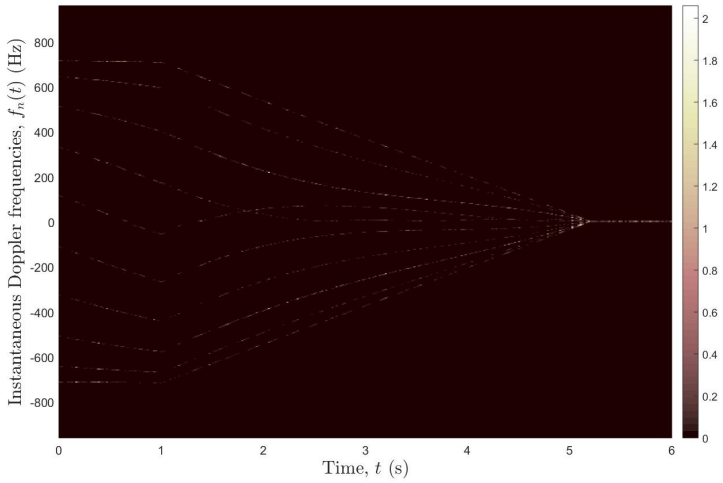

Figure 5.17: Spectrogram $S_{xx}(f,t)$ of process $\mu(t)$ for (a) v(t) = 80 km/h (b) v(t) = 110 km/h and, (c) v(t) = 130 km/h, using the exact model for AOA and Gaussian window size of $T = 0.25$ s.

(a) $T = 0.06$ s

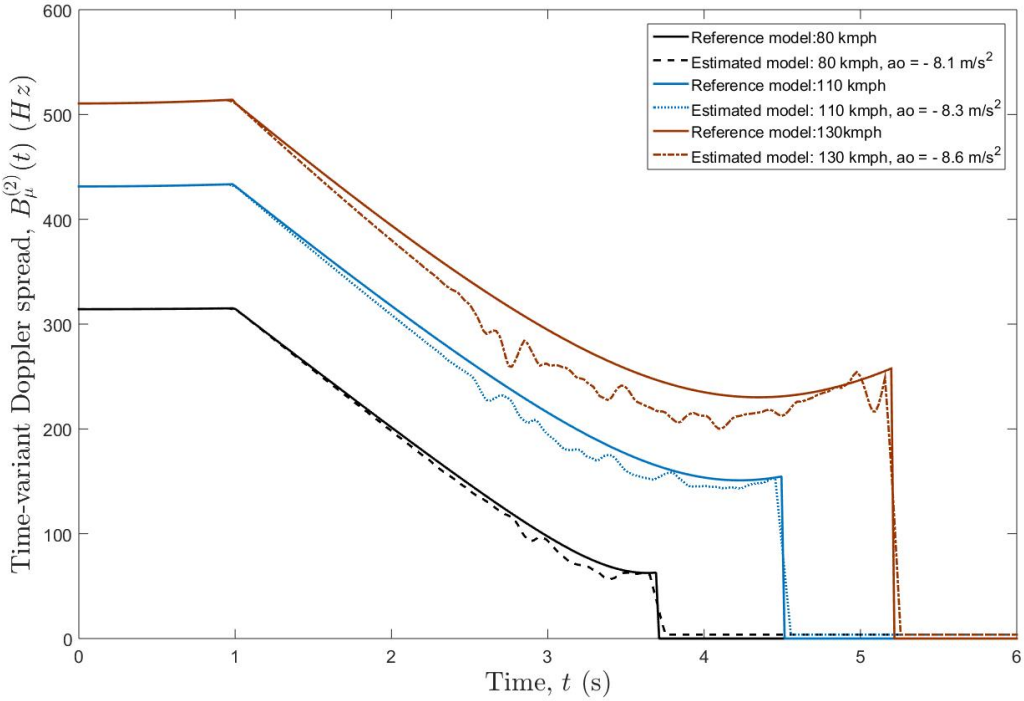

(b) $T = 0.07$ s

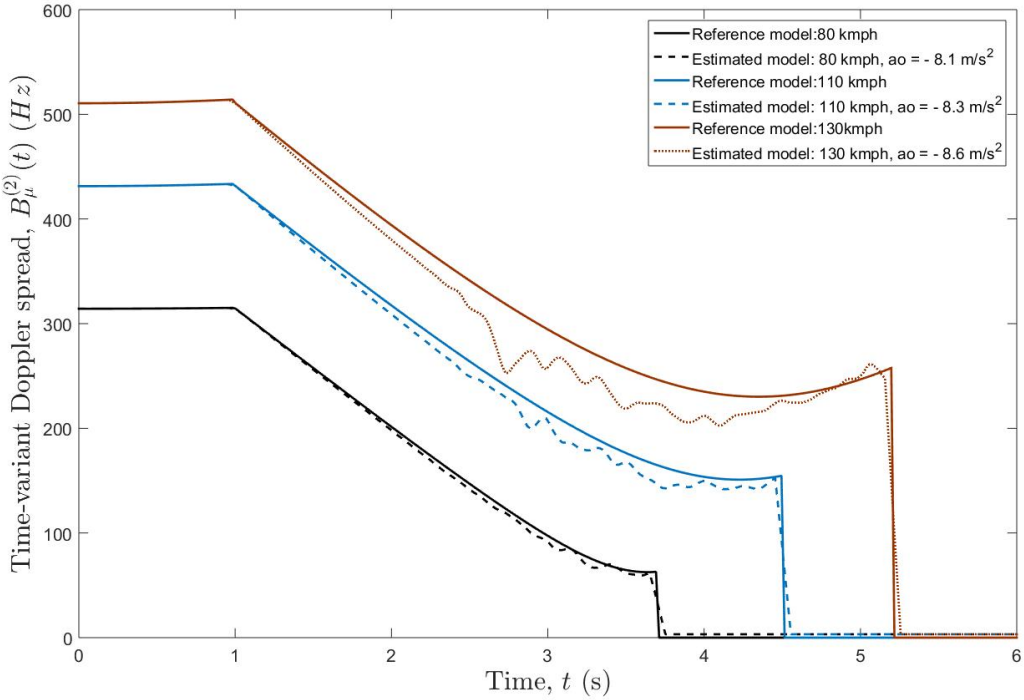

(c) $T = 0.08$ s

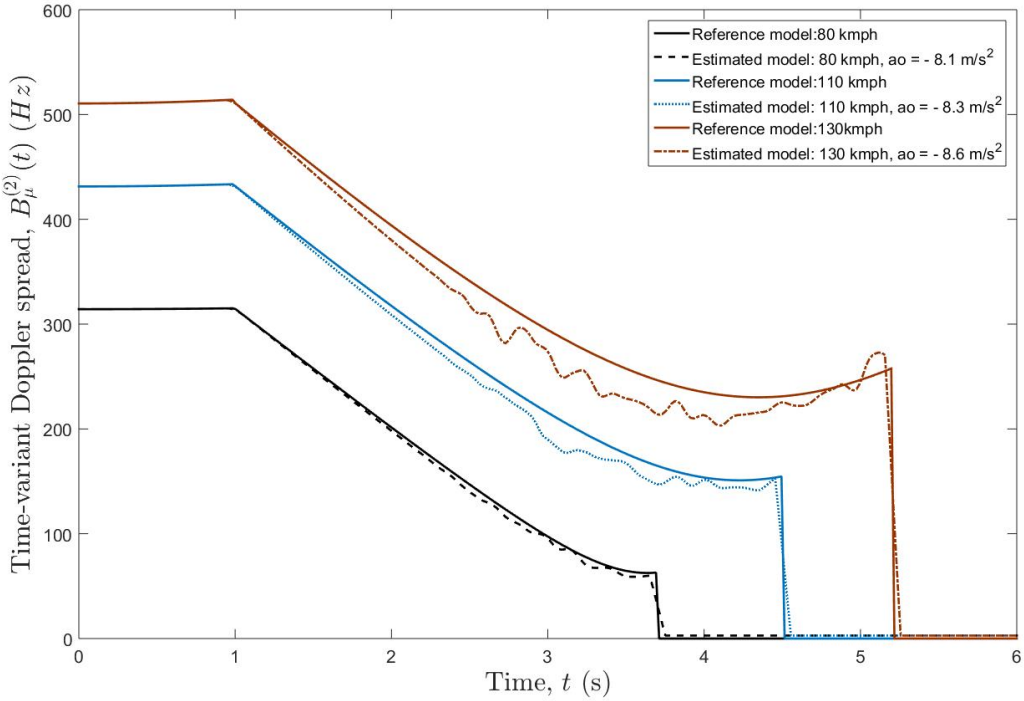

Figure 5.19: Time-variant Doppler spread $B_\mu^{(2)}(t)$ for process $\mu(t)$ obtained by the reference model and the estimated model by the spectrogram for (a) $T = 0.06$ s, (b) $T = 0.07$ s and, (c) $T = 0.08$ s.

Chapter 6

Discussions

This chapter is dedicated to discuss several important properties of non-stationary RSE-to-car channels for braking situations. Further, the certain limitations of the existing methods will also be discussed.

6.1 Analysis on Numerical Results

This thesis began by highlighting the need for a model to analyse the mobile radio channel as a combination of a sum of SOC_i processes and a sum of SOC_h processes. In [6], the Doppler PSD of multipath fading channel modelled by a sum of SOC_i processes was estimated by the concept of the spectrogram. The research work in [7] introduced the spectrogram to analyse the Doppler PSD of multipath fading channel modelled by a sum of SOC_h processes. Our work has combined the two concepts of these papers by combining to a single model to analyse the spectral behaviour of multipath mobile radio channel during the stationary and non-stationary period which occurred in braking situations. The numerical analysis conducted in [7] and [8] was limited to the moderate speeds of the MS, where the AOAs of multipath signals were not changed significantly. Further, in [7] and [8], the approximated model of time-variant Doppler shift was used and it is not well suited to analyse the spectral behaviour at higher speeds of the MS, where it shows a significant and conspicuous change in the AOAs. Our study has been extended to address said limitations of the previous research works by introducing a novel scenario in which higher initial speeds and higher declaration rates were introduced and exact models were considered for the time-variant AOA and the time-variant Doppler shift.

6.1.1 Spectrogram Analysis Under Low Mobile Velocity and Designed Braking Distances

The Fourier transform (FT)of the rectangle function results in oscillating sinc function and, the FT of the Gaussian window function is another Gaussian function in the frequency domain. In this thesis, the STFT of Hann, Hamming and Blackman windows were reduced to a sum of STFTs of rectangle window function. Hence, the effect of the oscillating sinc function is apparent in the frequency domain for the spectrogram defined using the cosine window functions (Hann, Hamming and Blackman windows). The Gaussian window function has improved the spectrogram compared with other window types. Further, the instantaneous power of the of the spectrogram of Blackman window

was greatly reduced both for stationary and non-stationary states, due to the enormous numbers of cross-terms.

The concept of random phase averaging is presented in [7] and the advantages and usage of phase averaging are discussed in [8]. Our results impressively show that the cross-term can be fully removed by the phase averaging accordance with the theory mentioned in [8].

The window length directly affects the time resolution and the frequency resolution of the STFT. It is not possible to obtain a better resolution in time and frequency domain simultaneously. A narrow size of window length T results in a better time resolution but worsens the resolution in frequency due to the fact that narrow windows have a short time duration but a wide bandwidth. A large window length T results in a better frequency resolution but a coarse time resolution because wide windows have a long time duration but a narrow frequency bandwidth. This phenomenon is known as the *window effect*. We have obtained different values for the optimum window length for each path of the multipath mobile radio channel based on the different values of k_n. It clearly means that the optimum window length improves the overall spectrogram whilst extensively optimise the frequency and time resolution of some propagation paths depicted in the spectrogram. Therefore, selection of an optimum window length is problematic for the improvement of the whole spectrogram. In this regard, the comparison between the estimated model and the reference model of time-variant Doppler spread has identified as a better approach for selecting the optimum window length of the window function.

6.1.2 Spectrogram Analysis for Emergency Braking Situations

In actual trials conducted for the emergency braking situations, test driver was required to bring the vehicle to a complete standstill from a higher speed as quickly as possible [14]. Therefore, higher initial speeds and higher deceleration rates were selected for the channel analysis in emergency braking situations.

The braking distance increase as the initial speed of the MS increases. Thus, high speeds of the MS caused a significant change in time-variant AOA. Therefore, for the time periods in which the MS travelled at a constant speed as well as for the braking period, the multipath mobile fading channel was considered as non-stationary. Compared with the approximated model, the exact model consisting time-variant AOA and the time-variant Doppler shift has shown an inevitable result for the spectrogram. However, the frequency resolution of the spectrogram had been greatly affected by the quick spectral variations occurred due to higher speeds and the higher decelerations. The highest speed i.e., 130 km/h of the MS worsened the resolution compared to lower speeds i.e., 80 km/h and 110 km/h. The poor frequency resolution has directly affected the estimated time-variant Doppler spread, and it was evident a large deviation from the reference model for higher speeds of the MS.

The carrier frequency offset (CFO) is one of the most known disturbances found in a communication system. It is due to the mismatch between the carrier frequency used by the transmitter and the receiver. The Doppler shift affects the frequencies of the RF carrier. Thus, large Doppler shifts may result in carrier frequency offset. In RSE-to-car multipath propagation scenario, when the brakes are applied at i.e., 130 km/h, the time-variant Doppler frequency varies from 722 Hz to 0 Hz within 4.2 s. The rapid change in the spread of the carrier frequency could be caused synchronisation failure between the local oscillation signal of the receiver and the carrier signal contained in the

received signal. It has implied the possibility of carrier frequency offset (CFO) at the receiver [27].

Chapter 7

Conclusion and Future Work

7.1 Conclusion

In this thesis, we have analysed the spectrogram of non-stationary RSE-to-car channels behaviour for the braking situation of the MS. Starting from the basic definition of the spectrogram, closed-form solutions were presented for the spectrogram using cosine window functions (Hann, Hamming and Blackman windows). Further, it has been showed that the STFT of cosine window functions can be found as a sum of STFTs of the rectangle window function. Later, the spectrogram was separated into auto-term and cross-term for all window types including rectangle, Gaussian and cosine windows. The auto-term consists of desired spectral information and the cross-term represents undesired interferences.

It has been demonstrated that the effect of the mobile velocity variations results in a non-stationary multipath channel. Based on the time-variant speed profile of the MS, it has been showed that the multipath fading channel can be modelled by the combinations of SOC_i and SOC_h processes for low speed of the MS under comfortable braking situations. The multipath fading channel was modelled by a sum of SOC_h processes for higher speed of the MS for the emergency braking situations. Two time-variant AOA models have been presented with the different degree of complexity; as exact and approximated models. Based on it an exact and, an approximated models were presented for the time-variant Doppler frequency.

The analysis was extended to observe the changes in the spectrogram with different types of window functions. It has been shown that the spectrogram defined by different types of window functions, can be compared by observing the instantaneous Doppler power vs frequency behaviour of the spectrogram. Further, the result has been verified by plotting and comparing the estimated time-variant Doppler spread. With both these tests, we have found that the Gaussian window function has improved the spectrogram.

Further, it has been demonstrated that the spectrogram can be improved by taking the average over the phases and selecting an optimal window length. The cross-term was completely removed by averaging multiple samples of the spectrogram with different phases. The average spectrogram implies the use of multiple antennas to reduce unwanted frequency interferences.

It has been shown that the reference model of time-variant average Doppler shift and time-variant Doppler spread, is realisable by the estimated model. Hence, it is shown that the window length is a decisive factor to improve the agreement between the reference model and the estimated model. Thus, it is proved this method is more useful to find the best optimum window length for the window functions.

For the higher speeds of the MS in emergency braking situations, it has been shown that the exact model of the time-variant AOA and the Doppler frequency has given a better result for the spectrogram with compared to approximated models. for the higher speeds of the MS, the estimated time-variant Doppler spread caused significant deviation from the reference model for emergency braking situations. It implied that the preciseness of the estimated time-variant Doppler spread model was limited to analyse the braking situations for the moderate speeds of the MS.

When the brakes are applied in an emergency situation at a higher speed of the car, the spectrogram showed a rapid decrement of time-variant Doppler shift within a very short time interval. This implies a possibility of carrier frequency offset in emergency braking situations, especially in future vehicular communications, where moderate vehicles may allow to reach higher safety speeds on better road conditions, and *mm*-waves ($30 - 300$ GHz) will be used for the communication.

The findings of this thesis give a deep insight into the performance improvement of the spectrogram analysis of non-stationary RSE-to-car multipath fading channel in braking situations.

7.2 Major Contributions

The topic of this thesis covered a range from the defining of the spectrogram using different window functions to the analysis of RSE-to-car channel behaviour for the braking situations of the MS. The main contributions of this thesis are summarised as follows.

• New definitions for the spectrogram was proposed using the cosine windows (Hann, Hamming and Blackman) as the window function.

• A new method was proposed for the comparison of the spectrogram using the instantaneous power of the spectrogram.

• The spectrogram was used to analyse the spectral behaviour of multipath mobile radio channel consisting a sum of SOC_i processes during the stationary state and a sum of SOC_h processes during the non-stationary state of the channel.

• We have modelled the time-variant AOA and the time-variant Doppler frequency using the exact and approximated methods. And later showed the limitation of the approximated model for the analysis of the local Doppler PSD of SOC_h processes, for the braking situations at higher speeds of the MS.

• The estimated time-variant Doppler spread is used for the comparison of the spectrogram and to find the optimum window length for the spectrogram to get good estimation of Doppler PSD.

• It has been shown that the spectrogram has been improved by random phase averaging and by optimising the window length. The optimum window length predominantly improved the instantaneous power of some paths of the multipath fading mobile radio channel depend on the locations of the scatterers. The result showed that the flat improvement is unachievable.

7.3 Recommendations for Future Work

The results of this thesis point to several interesting directions for future work.

This study can be extended by incorporating a car-to-car time-variant channel model for the analysis of braking situations.

The proposed method can be used to detect emergency braking situations by analysing the spectral behaviour of the channel. An another topic for research could be to develop road accident detection systems in which the spectral information of the MS could be used to detect road accidents possibly with the location, and it would be helpful for the quick evacuation of the victims.

Orthogonal frequency division multiplexing (OFDM) is widely used for data transmission applications in 4G wireless communications.The OFDM data transmission is very sensitive to frequency errors caused by frequency differences between the transmitter and receiver local oscillators. The analysis of methods of reducing the interference due to carrier frequency offset in OFDM in emergency braking situations could be another research interest for future work.

Bibliography

[1] Car-to-car Communication Consortium (C2C-CC) [Online]. Available: https://www.car-2-car.org.

[2] European Road Transport Telematics Implementation Co-ordination Organisation (ERTICO) [Online]. Available: http://ertico.com.

[3] Final report: Vehicle infrastructure integration proof of concept executive summaryVehicle, Res. Innovative Technol. Admin., U.S. Dept. Trans., Washington, DC, May 2009.

[4] IEEE Standard for Information Technology Telecommunications and information exchange between systems Local and metropolitan area networks Specific requirements Part 11: Wireless LAN Medium Access Control (MAC) and Physical Layer (PHY) Specifications Amendment 6: Wireless Access in Vehicular Environments, *IEEE Std 802.11p-2010*, pp. 1-51, July 2010.

[5] Intelligent Transport Systems (ITS); European profile standard for the physical and medium access control layer of Intelligent Transport Systems operating in the 5 GHz frequency band, *ETSI ES 202 663 V1.1.0 (2010- 01)*, 2010.

[6] M. Pätzold and N. Youssef, "Spectrogram analysis of multipath fading channels," *in IEEE 26th Annual International Symposium on Personal, Indoor, and Mobile Radio Communications (PIMRC)*, pp. 2214-2219, Sept.2015.

[7] M. Pätzold and C. A. Gutierrez, "Spectrogram analysis of multipath fading channels under variations of the mobile speed," *in Vehicular Technology Conference (VTC-Fall)*, pp. 1-6, Sept. 2016.

[8] M. Pätzold, C. A. Gutierrez and, N. Youssef, "Enchancing the resolution of the spectrogram of non-stationary mobile radio channels by using massive MIMO techniques," *in Vehicular Technology Conference (VTC-Fall)*, 2017, submitted.

[9] O. Renaudin, V. Kolmonen, P. Vainikainen, and C. Oestges, "Non-stationary narrowband MIMO inter-vehicle channel characterization in the 5-GHz band," *IEEE Transactions on Vehicular Technology*, pp. 2007-2015, May 2010.

[10] L. Bernad, N. Czink, T. Zemen, and P. Belanovic, "Physical layer simulation results for IEEE 802.11p using vehicular non-stationary channel model," *In IEEE Communications Workshops (ICC), IEEE International Conference*, pp. 1-5, May 2010.

[11] M. Pätzold, C. A. Gutierrez and, N. Youssef, "On the consistency of non-stationary multipath fading channels with respect to the average Doppler shift and the Doppler spread," *in IEEE Trans. Wireless Commun.*, to be published.

[12] B. Boashash, Ed.*Time-Frequency Signal Analysis and Processing:*,2nd ed. Elsevier Academic Press 2015.

[13] M. Pätzold, B. O. Hogstand and N. Youssef, "Modelling, analysis, and simulation of MIMO mobile-to-mobile fading channels," *in IEEE Trans. Wireless Commun.*, vol 7, no. 2, pp. 510-520, Feb. 2008.

[14] P. Greibe, "Braking distance, friction and behaviour. Findings, analyses and recommendations based on braking trials.", Trafitec Report,pp. 5-8, 41-43, 2007.

[15] P. S. Gradshteyn and I. M. Ryzhik, "*Table of Integrals, Series, and Products.*"7th ed. Elsevier Academic Press,2007.

[16] J. F. Harris, "On the use of windows for harmonic analysis with the discrete Fourier transform", *Proceedings of the IEEE*,vol. 66, no. 1, pp. 51-83, 1978.

[17] D. Mitchell and A. Netravali, "Reconstruction filters in computer-graphics", *ACM SIGGRAPH Computer Graphics*, vol. 22, no. 4, pp. 221-228, 1988.

[18] A. Paier, J. Karedal, N. Czink, C. Dumard, T. Zemen, F. Tufvesson, A. Molisch, and C. Mecklenbräuker, "Characterization of Vehicle-to-Vehicle radio channels from measurements at 5.2 GHz", *Wireless Personal Communications*, vol. 50, no. 1, pp. 19-32, 2008.

[19] A. Borhani and M. Pätzold, "A novel non-stationary channel model utilizing Brownian random paths", *REV Journal on Electronics and Communications*, vol. 4, no. 1-2, 2014.

[20] M. Pätzold and A. Borhani, "A non-stationary multipath fading channel model incorporating the effect of velocity variations of the mobile station," *2014 IEEE Wireless Communications and Networking Conference (WCNC), Istanbul*, 2014, pp. 182-187.

[21] R. Iqbal and TD. Abhayapala. "Impact of mobile acceleration on the statistics of Rayleigh fading channel." *Proc. 8th Australian Communication Theory Workshop, AusCTW*, 2007.

[22] F. J. Harris, "On the use of windows for harmonic analysis with the discrete Fourier transform," *in Proceedings of the IEEE*, vol. 66, no. 1, pp. 51-83, Jan. 1978.

[23] L. Stankovic, "Auto-term representation by the reduced interference distributions: a procedure for kernel design," *in IEEE Transactions on Signal Processing*, vol.44, no. 6, pp. 1557-1563, Jun 1996.

[24] Q. Yin, L. Shen, M. Lu, X. Wang and Z. Liu, "Selection of optimal window size using STFT for quantitative SNR analysis of LFM signal," *Journal of Systems Engineering and Electronics*, vol. 24, no. 1, pp. 26-35, Feb. 2013.

[25] M. Pätzold, Mobile Radio Channels, 2nd ed. Chichester, West Sussex, U.K.: Wiley, 2012, pp. 62-65,439-440.

[26] M. Pätzold, B. O. Hogstad and N. Youssef, "Modelling, analysis, and simulation of MIMO mobile-to-mobile fading channels," *in IEEE Transactions on Wireless Communications*, vol. 7, no. 2, pp. 510-520, February 2008.

[27] K.Sathananthan and C. Tellambura, "Performance analysis of an OFDM system with carrier frequency offset and phase noise," *IEEE Vehicular Technology Conference, 2001*,vol. 4,pp. 2329-2332, 2001.

Appendix A

Attached Publications

Title: Spectrogram Analysis of Non-Stationary Base Station-to-Mobile Channels Under Variations of the Mobile Velocity

---

Affiliation: University of Agder, Faculty of Engineering and Science,
P.O. Box 509, 4898 Grimstad, Norway

Submission status: Draft

Spectrogram Analysis of Non-Stationary Base Station-to-Mobile Channels Under Variations of the Mobile Velocity

Buddika Herath, *Member, IEEE*

***Abstract*—One of the standard assumptions of mobile radio channel modelling is that the speed of the mobile station (MS) is constant. However, in the real-world, mobile communication channels exhibit non-stationarity as the frequencies vary with the time. In this paper, we analyse the spatial characteristics of the mobile radio channel under variations of the mobile velocity using the concept of the spectrogram. The Spectrogram provides an estimate of the changes to local Doppler power spectral density over time for the variations of the velocity. The term velocity includes the variation of mobile speed and the change of direction. In addition, we investigate the spectrogram result optimisation by averaging over the phases and selecting an optimal window length. Furthermore, our study shows that the time-variant average Doppler shift, computed by taking the sum of all power-weighted Doppler shifts normalised to the total received power of the multipath components, is realisable by the average Doppler shift computed from the spectrogram.**

I. Introduction

THE movement of the mobile station (MS) with a constant speed along a particular direction is considered as a standard assumption in mobile radio channel modelling. This assumption is not valid in the real-world as the speed and angle of motion rapidly varies with time. Therefore, the constant speed assumption potentially hides the actual mobile radio channels characteristics. Hence, the study of time-variant characteristics of wireless mobile channels has acquired a wide space in research domain in the recent years.

The wide-sense stationary assumption of a mobile radio channel is only valid for very short travelling distances of a mobile station (MS) as described in [1] and [2]. In the real-world, mobile communication channels exhibit non-stationarity as the frequency of each channel varies with the time. The change of velocities of MSs cause the channel statistics to be non-stationary. In [3], it is assumed that the transmitter is stationary and the receiver station linearly increases (or decreases) its speed, while the angle of motion is kept fixed. A fixed station-to-mobile multipath channel model with both varying speed and angle of motion (AOM) is presented in [4]. In Section II of this research work, the channel model stipulated in [3] is extended to analyse the base station-to-mobile channel model with varying MS velocity and AOM using different MS trajectories and scattering scenarios. The standard assumption: fixed transmitter, is used in modelling all the scenarios in this report. The work in Section II explains the mobile multipath channel model when scatterers are on a ring (with identical spacing) as well as randomly inside a rectangle, with time-varying velocity and AOM. Further, the work is extended to analyse the path distance travelled by the MS with different AOM and velocities. A trajectory path along the x-axis is considered as a special case. The spectral behaviour of a vehicular mobile radio channel when the brakes are applied at a constant speed is included as a novel case in Section II.

The spectrogram is a vital tool to analyse non-stationary mobile multipath channel models. The spectrogram provides a three-dimensional (frequency, time and intensity) representation based on the spatial characteristics of the considered signal. The spectrogram consists of two terms: the auto-term and the cross-term. The auto-term provides an estimate of the local Doppler power spectral density (PSD) and the cross-term consists of unwanted noise and interferences [5]. The spectrogram of a non-stationary signal is generated by breaking the signal into overlapping short-time signals and then by taking short-time Fourier transforms (STFT) of the short-time signals. In other words, the time varying signal can be multiplied by a moving window function to obtain overlapping short-time signals, and later on the squared magnitude of the STFT of the short-time signals generates the spectrogram. The length T of the window function is a decisive factor to improve the spectrogram. The fixed size window length for the STFT can cause poor resolution in the spectrogram but does not affect the cross-terms [6]. In [7], it is explained how the instantaneous frequency and instantaneous bandwidth are used to deduce the relation between window length and deviation of the Gaussian window so that the selection of the appropriate window length for the STFT is used to get the optimal SNR(signal-to-noise ratio), which subsequently optimises the spectrogram of the signal. Further, the average spectrogram also improves the time-varying frequency resolution. Section III is dedicated to the analysis of the spectrogram for non-stationary signals. The spectrogram is used to cover all widely-explained scenarios. The average spectrogram is also improves the optical resolution.

The most important characteristics of the Doppler PSD are the average Doppler shift and the Doppler spread. In stationary channels, the average Doppler shift depicts the average frequency shift of the carrier signal experienced during the transmission of the multipath mobile radio channel. Similarly, the average Doppler spread defines the average frequency spread. The first moment of the Doppler PSD provides the average Doppler shift, and the square root of the second central moment provides the average Doppler spread [8]. In non-stationary channels, the time-variant average Doppler shift

is obtained by computing the sum of all power-weighted Doppler shifts normalised on the sum of the received power of all multipath components. The time-variant Doppler spread can be obtained by the channel gains, time-variant Doppler frequencies, and the time-variant average Doppler shift. An analysis on the time-variant average Doppler shift and time-variant average Doppler spread is included in Section IV of this report.

Section V presents the numerical results and finally, Section VI draws the conclusion of this report.

II. Multipath Propagation Scenarios for Non-Stationary Channel Analysis

The multipath propagation scenario considered for this paper consists of a fixed base station (BS) and an MS which moves with time-variant velocity $\vec{V}(t)$. It is assumed that the BS and the MS are equipped with omnidirectional antennas and a large number of N fixed scatterers $S_n(n = 1, 2, ..., N)$ are located around the MS. The line-of-sight (LOS) component between the BS and the MS is ignored. The propagation scenario is illustrated in Fig.1. With the time-variant speed $v(t)$ and the time-variant AOM $\alpha_v(t)$, $\vec{V}(t)$ can be defined as $\vec{V}(t) = v(t)\exp(j\alpha_v(t))$. We adopt the following expressions from [3]

$$v\,(t) = v_0 + a_0 t \tag{1}$$

$$\alpha_v(t) = \alpha_v + b_0 t\,. \tag{2}$$

In (1), v_0 denotes the initial speed at t = 0, and a_0 is called the acceleration (when $a_0 > 0$) or deceleration (when $a_0 < 0$) parameter. The acceleration parameter α_0 in (2) denotes the initial AOM at t = 0, and b_0 is called the angular speed. Now, we will turn our attention to the time-variant maximum Doppler frequency $f_{\max}(t)$.

$$f_{\max}(t) = \frac{f_0}{c_0} v\,(t) = \frac{f_0}{c_0}(v_0 + a_0\,t\,) \tag{3}$$

where f_0 is the carrier frequency and c_0 is the speed of light. With this in mind we can write the time-variant Doppler shift of the nth received multipath component $f_n(t)$ as

$$f_n(t) = f_{\max}(t)\,.\cos(\alpha_n(t) - \alpha_v(t)) \tag{4}$$

where $\alpha_n(t)$ is the time-variant angle of arrival (AOA) of the nth plane wave.

Consequently, by developing (4) in a Taylor series around $t = 0$ and retaining only the first two terms, we can simplify the time-variant Doppler shift $f_n(t)$ as

$$f_n\,(t) = f_n + k_n t \tag{5}$$

where

$$f_n = f_{\max}.\cos(\alpha_n - \alpha_v), \tag{6}$$

$$k_n = f_{\max}\left[\frac{a_0}{v_0}\cos\left(\alpha_n - \alpha_v\right) + (b_0 - \gamma_n)\sin\left(\alpha_n - \alpha_v\right)\right] \tag{7}$$

and

$$\gamma_n = \frac{v_0}{r_n}\sin(\alpha_n - \alpha_v). \tag{8}$$

In (6), $\alpha_n = \alpha_n(0)$ and $f_{\max} = f_{\max}(0)$, denotes the initial AOA at $t = 0$ and the initial maximum Doppler shift at $t = 0$, respectively. Further, in (7) k_n can be written as a sum of three terms. The first term takes into account the acceleration or deceleration of the MS. Second term is due to the change of direction of motion and the third term is derived from the AOA of the MS.

By referring to the above discussion, the received complex envelope $\mu(t)$ of the multipath non-stationary channel can be defined as

$$\mu(t) = \sum_{n=1}^{N} c_n e^{j(2\pi f_n(t)t + \theta_n)} \tag{9}$$

where, θ_n and c_n denotes the random phases and gains.

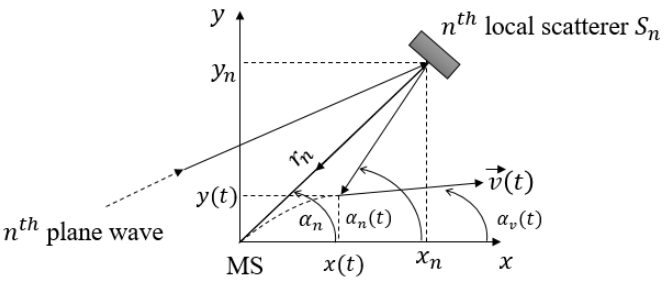

Fig. 1: A multipath propagation scenario in which the MS travels with time-variant velocity $\vec{V}(t)$.

A. Description of the Trajectories

Starting with (1) and (2), and taking different values mentioned in Table I for a_0 and b_0, we can define three main trajectories for the MS as shown in Fig. 2. Path III is considered as a special case in which $b_0 = 0$. Further, the work is extended to introduce a new trajectory for a vehicular MS: brakes are applied at a constant speed.

B. Description of the Scattering Scenarios

We now consider two different scattering scenarios in which scatterers are either located on a ring or randomly located inside a rectangle.

1) Distribution of scatterers on a ring: In the considered scenario, we assume that scatterers are located with identical spacing on a ring of radius R centered on the MS as shown in Fig. 3. The ring radius R and number of scatterers N are set to 100 m and 10, respectively. The AOA is given by

$$\alpha_n = \frac{2\pi}{N}\left(n - \frac{1}{4}\right), \quad n = 1, 2, \ldots, N. \tag{10}$$

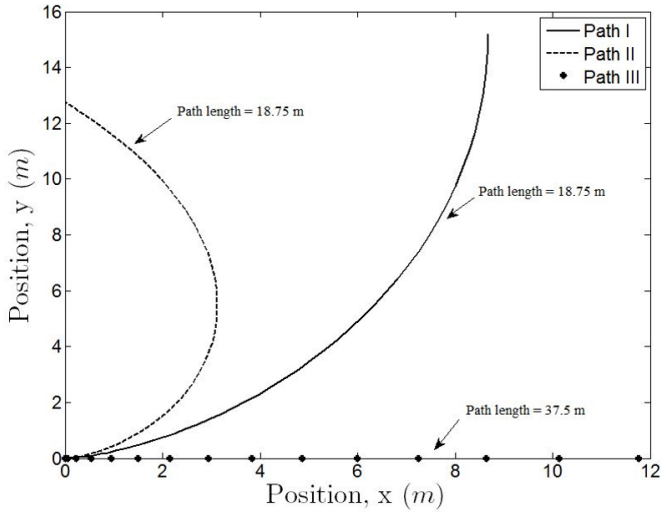

Fig. 2: Different trajectories along which the MSs can travel in the (x, y) plane.

TABLE I: Parameters of the trajectories taken by T_x and R_x in different propagation scenarios.

Paths	Speed Acceleration	Angular Speed	Maximum Speed
I	$a_0 = 1.5\ m/s^2$	$b_0 = \frac{\pi}{10} s^{-1}$	$V_T(t) = 27\ km/h$
II	$a_0 = 1.5\ m/s^2$	$b_0 = \frac{\pi}{6} s^{-1}$	$V_T(t) = 27\ km/h$
III	$a_0 = 1.5\ m/s^2$	$b_0 = 0\ s^{-1}$	$V_T(t) = 27\ km/h$

2) Random distribution of scatterers inside a rectangle: We assume that scatterers are randomly and independently distributed within a rectangle and the MS is at the centroid point. Fig. 4 represents uniformly distributed random scatterers ($N = 10$). The locations of the scatterers are uniformly distributed as

$$x_n = u(x_1, x_2),\ y_n = u(y_1, y_2) \tag{11}$$

$$\alpha_n = \arctan\left(\frac{y_n}{x_n}\right), \quad n = 1, 2, \ldots, N. \tag{12}$$

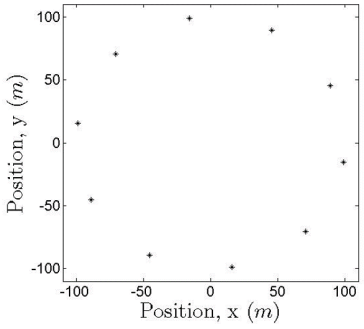

Fig. 3: Locations of scatterers on a ring in the (x, y) plane.

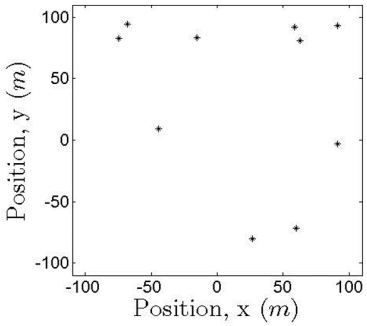

Fig. 4: Locations of scatterers on a rectangle in the (x, y) plane.

The parameters x_1, y_1 are set to -100 m and x_2, y_2 are set to 100 m.

III. Spectrogram Analysis of Non-Stationary Mobile-to-Base Station Channels

A. Definition of the Spectrogram

We first consider the time-varying signal $\mu(t)$. The basic idea of the spectrogram is to take the time-variant signal and break it up to overlapping short-time signals. Then, the squared magnitude of the short-time Fourier transformation of short-time signals defines the spectrogram.

The short-time signal $X(f, t)$ of the time-varying signal $\mu(t)$ can be obtained by multiplying $\mu(t)$ by a rectangle function $h(t)$ as shown in Fig. 5 where

$$h(t) = \begin{cases} \frac{1}{\sqrt{T}}, & -\frac{T}{2} \le t \le \frac{T}{2} \\ 0, & \text{otherwise} \end{cases} \tag{13}$$

and T is the window length.

The short-time Fourier transform (STFT) of $X(f, t)$ with respect to the variable t' can be defined as:

$$X(f, t) = \int_{-\infty}^{\infty} x(t', t) e^{-i2\pi f t'} dt'. \tag{14}$$

The squared magnitude of the STFT $X(f, t)$ defines the spectrogram $S_{xx}(f, t)$ as

$$S_{xx}(f, t) = |X(f, t)|^2. \tag{15}$$

B. Different Spectrogram Window Types

Windows are weighting functions applied to a signal to reduce the spectral leakage associated with long observation intervals [5]. The spectral leakage is known as the set of signals with frequencies other than the basis set. In another word, the spectral leakage increases the cross-term of the spectrogram. Hence, windows are used to reduce the undesirable effects related to spectral leakage. We will now discuss some well-known window types.

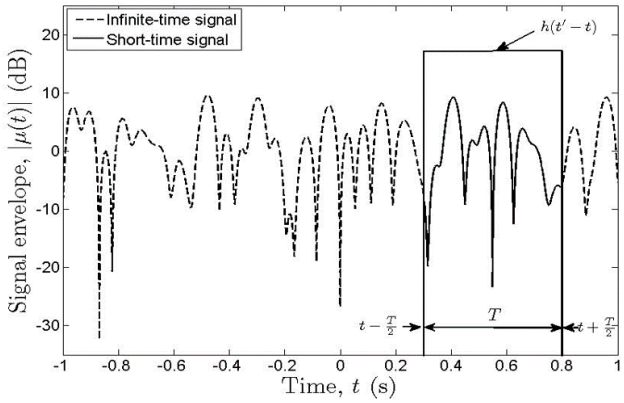

Fig. 5: Time-varying signal $\mu(t)$ and the corresponding short-time signal $x(t^{'},t)$ observed through a rectangular window of length T= 0.5 s centered at time t= 0.55 s.

1) Rectangle window: The rectangle window is the simplest window type and it is unity over the observation interval. The Fourier transformation of a rectangle function is the sync function. Therefore, the rectangle window consists of multiple high-level side lobes which hinder the ability to distinguish different frequencies of a signal. This characteristic is sometimes described as a low dynamic range. Figures 6(a) and (b) illustrate the rectangle window and the log magnitude of the transformation.

$$w(n) = 1, \qquad 0 \leq n \leq 1 \tag{16}$$

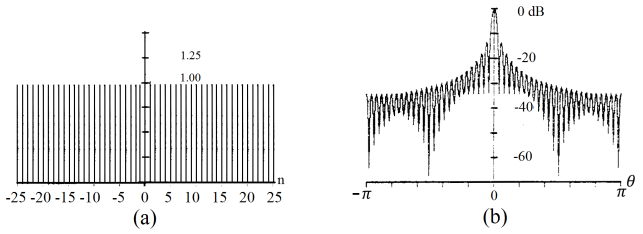

Fig. 6: (a) rectangle window, and (b) log-magnitude of the transform [5].

2) Hann window: The fast fallout of the side lobes improves the dynamic range in the Hann window. We note from the inspection of Fig. 7 (b) that the power level of the side lobes is significantly suppressed.

The Hann window is defined as

$$w(n) = 0.5\left(1 - \cos\left(\frac{2\pi n}{N-1}\right)\right), \qquad 0 \leq n \leq N-1. \tag{17}$$

3) Blackman window: The Blackman window is defined as

$$w(n) = a_0 - a_1\cos\left(\frac{2\pi n}{N-1}\right) + a_2\cos\left(\frac{4\pi n}{N-1}\right), \quad 0 \leq n \leq N-1. \tag{18}$$

The Blackman window uses three coefficients (a_0, a_1, a_2) with two place approximations. The values of the coefficients can be

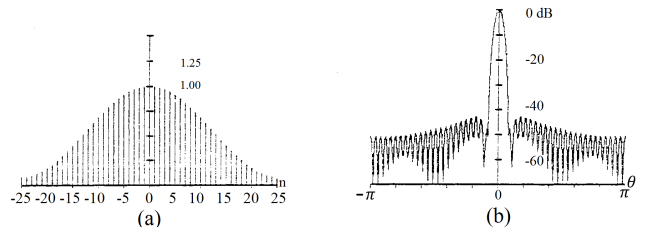

Fig. 7: (a) Hann window, and (b) log magnitude of the transformation [5].

listed as $a_0 = 0.42, a_1 = 0.5$ and $a_2 = 0.08$.These coefficients place zeros at the third and fourth side lobes as depicted in Fig. 8(b). The Blackman window closely approximates the "exact Blackman" with $a_0 = 7938/18608 \approx 0.42659, a_1 = 9240/18608 \approx 0.49656$, and $a_2 = 1430/18608 \approx 0.076849$ [5].

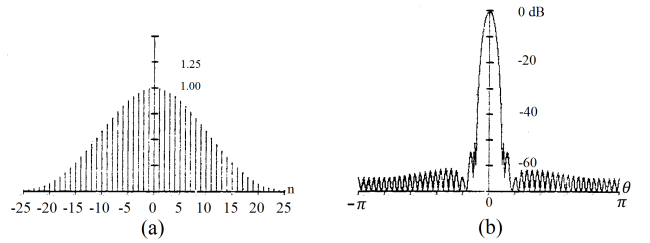

Fig. 8: (a) Blackman window, and (b) log-magnitude of the transformation [5].

4) Kaiser window: The Kaiser or Kaiser-Bessel window is a simple approximation of the discrete prolate spheroidal sequence (DPSS) or Slepian window using Bessel functions.

The Kaiser window is defined as

$$w(n) = \frac{I_0\left(\pi\alpha\sqrt{1-(\frac{2N}{N-1}-1)^2}\right)}{I_0(\pi\alpha)}, \qquad 0 \leq n \leq N-1 \tag{19}$$

where, I_0 is the zeroth-order modified Bessel function of the first kind.

The variable parameter α determines the trade-off between the main lobe width and side lobe levels. The main lobe width, in between the nulls is defined as $2\sqrt{(1+\alpha^2)}$ and the typical value of α is 3. Figures 9 (a) and (b) illustrate the Kaiser window and the log magnitude of the transformation.

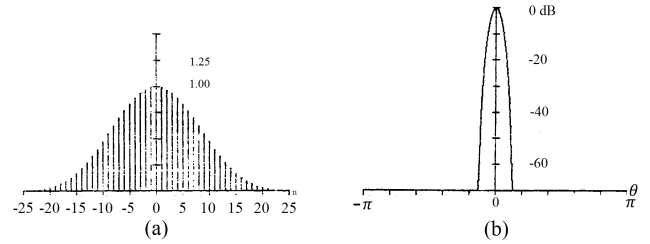

Fig. 9: (a) Kaiser window, and (b) log magnitude of the transformation [5].

5) Gaussian window: The Fourier transform of a Gaussian function is also a Gaussian function. Since the Gaussian function extends to infinity, it must either be truncated at the ends of the window, or it need to be windowed with another zero-ended window function. Figure 10 (a) and (b) illustrates the Gaussian window and its log magnitude of the transformation.

The Gaussian window is defined as

$$w(n) = e^{-\frac{1}{2}\left(\frac{n-(N-1)/2}{\sigma(N-1)/2}\right)^2}, \quad 0 \le n \le N-1. \tag{20}$$

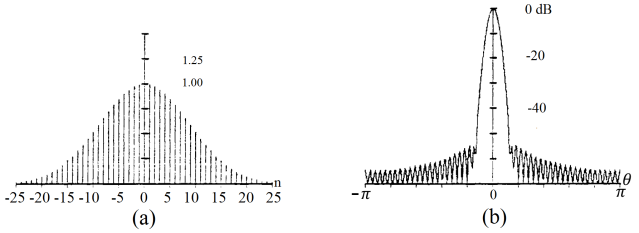

Fig. 10: (a) Gaussian window, and (b) log-magnitude of the transformation [5].

For comparison, we also include the spectrogram of the time-varying signal using the above mentioned window types.

C. Optimal Window Length and Average Spectrogram

The spectrogram $S_{xx}(f,t)$ is highly sensitive to the window length T. The span of the side lobes increases with a large window length, while a smaller window length reduces the number of samples required for a better optical resolution. Hence, it is vital to select the optimal window length for a better optical resolution of the spectrogram of the time-variant signal $\mu(t)$. For our analysis, it will suffice to select the optimal window lengths by visual inspection. Furthermore, the spectrogram $S_{xx}(f,t)$ can be improved by averaging over the random phases θ_n.

IV. Time-Variant Average Doppler Shift and Doppler Spread

From the theory developed before, it is seen that the time-variant Doppler shift $f_n(t)$ is defined as a linear Doppler frequency model as stated in (5).

Then, the time-variant average Doppler shift $B_f^{(1)}(t)$ can be obtained by computing the sum of all power-weighted Doppler shifts normalized to the total received power of all multipath components according to

$$B_f^{(1)}(t) = \frac{\sum\limits_{n=1}^{N} c_n^2 f_n(t)}{\sum\limits_{n=1}^{N} c_n^2}. \tag{21}$$

The time-variant average Doppler shift $B_f^{(1)}(t)$ can be used to compute the time-variant average Doppler spread $B_f^{(2)}(t)$ of a time-variant signal as

$$B_f^{(2)}(t) = \sqrt{\frac{\sum\limits_{n=1}^{N} c_n^2 f_n^2(t)}{\sum\limits_{n=1}^{N} c_n^2} - \left(B_f^{(1)}(t)\right)^2}. \tag{22}$$

Alternatively, we can compute the time-variant average Doppler shift $B_\mu^{(1)}(t)$ and the time-variant Doppler spread $B_\mu^{(2)}(t)$ of the time-variant signal $\mu(t)$ by means of the spectrogram $S_{xx}(f,t)$. The first moment of the spectrogram $S_{xx}(f,t)$ defines the time-variant average Doppler shift $B_\mu^{(1)}(t)$, and the square root of the second central moment of the spectrogram $S_{xx}(f,t)$ defines the time-variant average Doppler spread $B_\mu^{(2)}(t)$. This alternate approach leads to

$$B_\mu^{(1)}(t) = \frac{\int_{-\infty}^{\infty} f S_{xx}(f,t)df}{\int_{-\infty}^{\infty} S_{xx}(f,t)df} \tag{23}$$

and

$$B_\mu^{(2)}(t) = \sqrt{\frac{\int_{-\infty}^{\infty} \left(f - B_\mu^{(1)}(t)\right)^2 S_{xx}(f,t)df}{\int_{-\infty}^{\infty} S_{xx}(f,t)df}}. \tag{24}$$

A similar approach has presented in [8] for a stationary channel.

In this case, the reference model consists of (21) and (22) whereas the simulation model consists of (23) and (24).

V. Numerical Results

This section presents some numerical examples to illustrate the obtained analytical results for different propagation scenarios.

For each propagation scenario, it is considered a multipath channel consisting of $N = 10$ components. The path gains c_n is computed according to the extended method of exact Doppler spread (EMEDS) as follows [9]

$$c_n = \sigma_0 \sqrt{\frac{2}{N}}. \tag{25}$$

The variance σ^2 is set to unity while the phases are considered as random and uniformly distributed over the interval $(0, 2\pi)$. The initial speed v_0 and the initial AOM α_v of the MS are considered as 110 km/h and 0, respectively. Furthermore, the maximum Doppler frequency is assumed as 91 Hz. Unless otherwise stated, it is assumed that the acceleration parameter α_0 is 1.5 m/s^2. We will consider other parameters in respective subsections.

A. Comparison of Spectrogram Window Types

We have considered only the acceleration term of k_n and the scattering scenario in which it is assumed that scatterers are located on a ring. Figure 11 illustrates the spectrogram $S_{xx}(f,t)$ for different types of window functions considered

in Section III-B. We note from the inspection of Fig. 11 that the Gaussian window function improved the spectrogram.

However, for our analysis of the spectrogram, it will suffice to consider the rectangle window function.

B. Spectrogram Analysis Under Variations of Mobile Velocity

1) Spectrogram Analysis Under Variations of Mobile Speed: We considered only the acceleration term of k_n, and for comparative purposes, we have also plotted the spectrogram $S_{xx}(f,t)$ under both scattering scenarios mentioned in Section II-B. Further, different window lengths from 0.5 s to 5 s are used and we have noted from visual inspection that 1.2 s of window length optimise the spectrogram.

Figures 12, 13 and 14 illustrates the spectrogram $S_{xx}(f,t)$ and the average spectrogram for the window lengths 0.5 s, 1.2 s (optimal), and 5 s considering the first scattering scenario in which scatterers are located on a ring. Similarly, Fig. 15-17 illustrate the spectrogram $S_{xx}(f,t)$ and the average spectrogram for the second scattering scenario (scatterers are randomly located inside a rectangle) for the said window lengths.

2) Spectrogram Analysis Under Variations of Mobile Speed, Direction of Motion and Angle of Arrival: Here, we consider that the MS is allowed to move along one of three different trajectories illustrated in Fig. 2. We note from Table I that the angular speed parameter $b_0 = \pi/10$ s^{-1} for the Path I, $b_0 = \pi/6$ s^{-1} for Path II and, $b_0 = 0$ for Path III.

Further, we consider all terms (acceleration, change of direction and change of AOA) of k_n. For our analysis, it will suffice to consider the first scattering scenario in which scatterers are located on a ring. Figure 18 illustrates the spectrogram $S_{xx}(f,t)$ for trajectory Path I, II and III. Considering the higher Doppler shift, the optimal window size is selected as 0.3 s.

C. Spectrogram Analysis Under the Condition that the Vehicle Brakes.

Here, we assume that the MS was moving at a constant speed (110 km/h) at the time the brakes are applied. For the simplicity, we only consider the acceleration term of k_n. If we eliminate the reaction distance, then the time spent for the braking distance can be computed by taking the deceleration parameter a_0. We set deceleration parameter a_0 to -1.5m/s^2 and assume that the braking distance is 75 m. Then, the approximate stopping time is computed as 20 s. Hence, we set the observation period to 20 s. The spectrogram shown in Fig. 19 illustrates the spatial characteristics of the vehicular MS when and after applying the brakes.

D. Time-Variant Average Doppler Shift and Doppler Spread

In our numerical study on time-variant average Doppler shift $B_f^{(1)}(t)$ and time-variant average Doppler spread $B_f^{(2)}(t)$, we have considered all terms of k_n and the ring scattering scenario. Furthermore, three trajectory paths, according to the value given in Table I for a_0 and b_0, were considered for the numerical analysis. For the simulation model, we

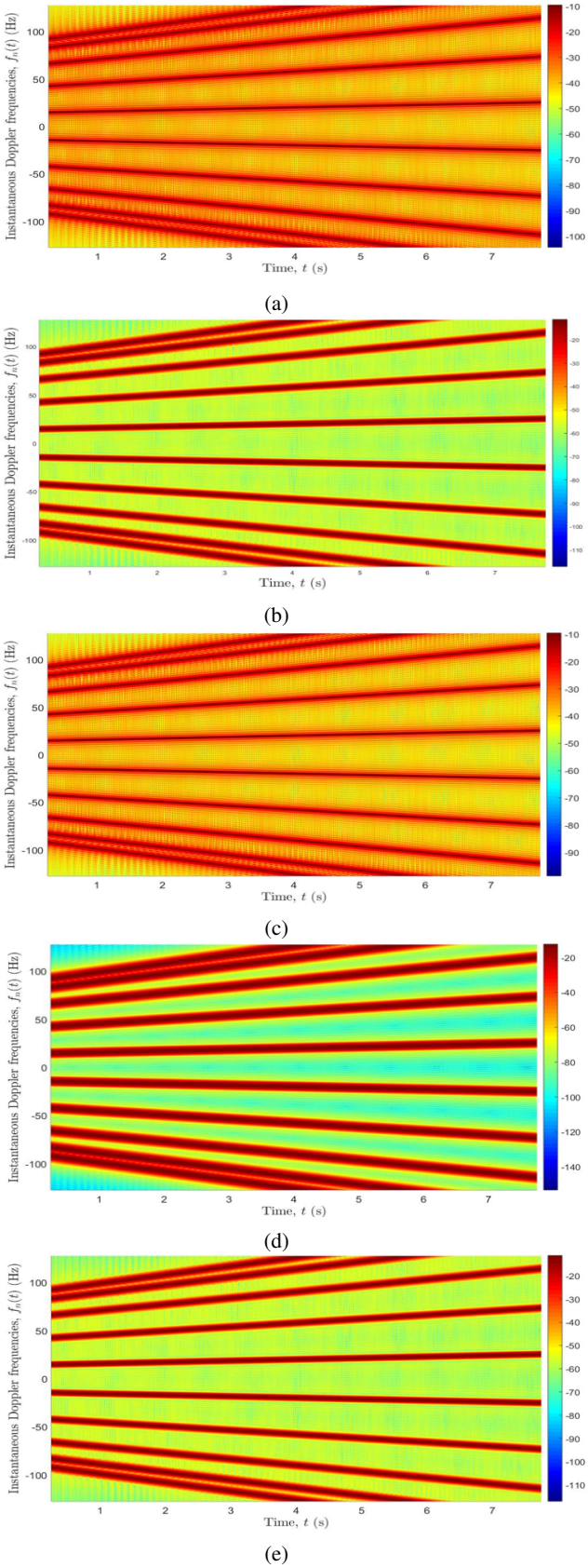

Fig. 11: (a) Rectangle window. (b) Hann window. (c) Kaiser window. (d) Blackman window. (e) Gaussian window.

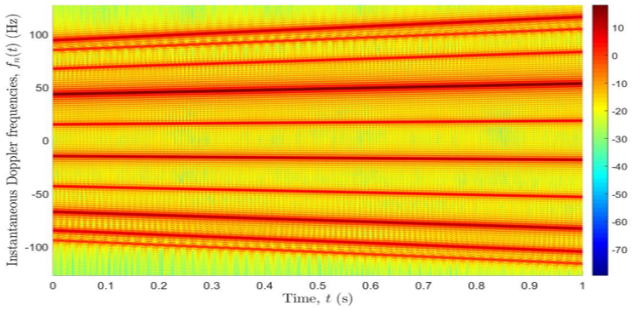

(a)

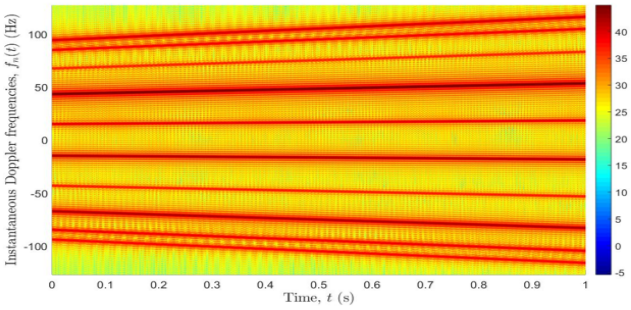

(b)

Fig. 12: (a) Spectrogram $S_{xx}(f,t)$, and (b) average spectrogram of process $\mu(t)$ for $N = 10$,window size of $T = 0.5$ s and the scatterers are located on a ring.

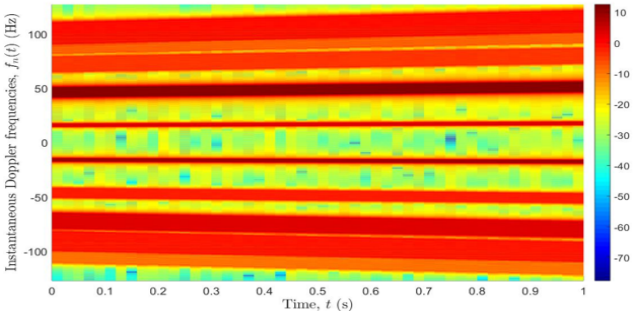

(a)

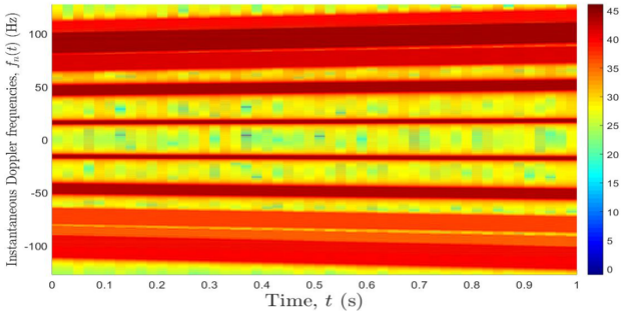

(b)

Fig. 14: (a) Spectrogram $S_{xx}(f,t)$, and (b) average spectrogram of process $\mu(t)$ for $N = 10$, window size of $T = 5$ s and the scatterers are located on a ring.

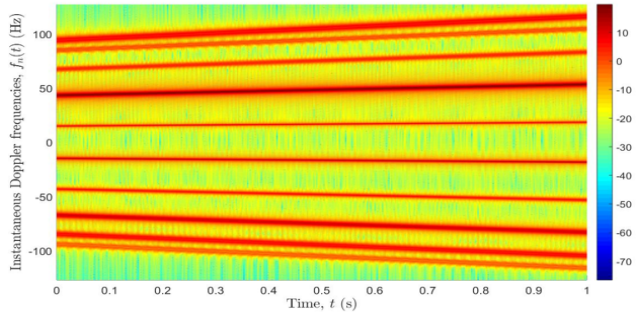

(a)

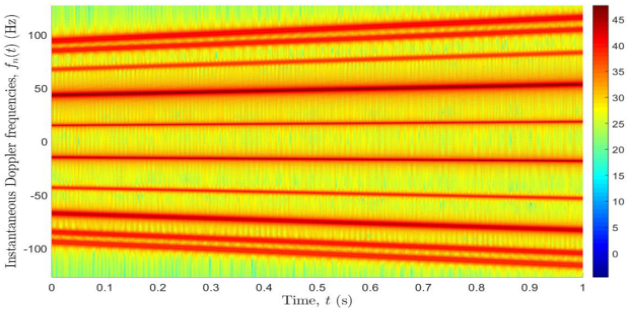

(b)

Fig. 13: (a) Spectrogram $S_{xx}(f,t)$, and (b) average spectrogram of process $\mu(t)$ for $N = 10$, optimal window size of $T = 1.2$ s and the scatterers are located on a ring.

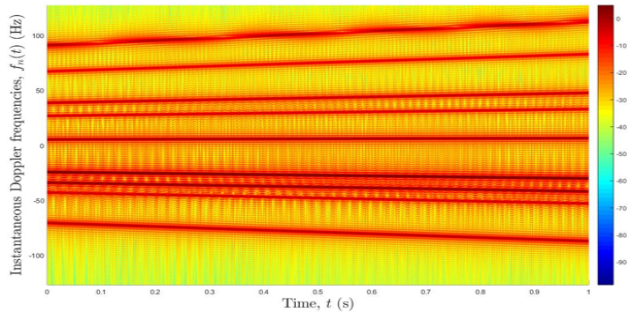

(a)

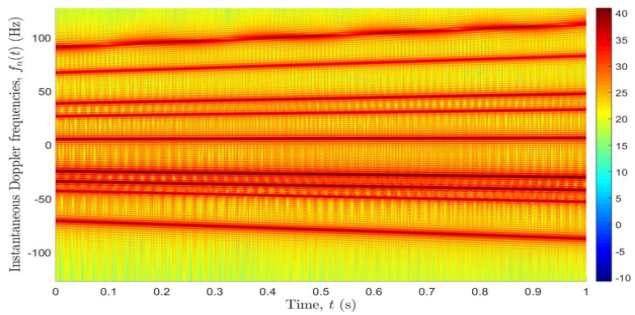

(b)

Fig. 15: (a) Spectrogram $S_{xx}(f,t)$, and (b) average spectrogram of process $\mu(t)$ for $N = 10$,window size of $T = 0.5$ s and the scatterers are randomly located inside a rectangle.

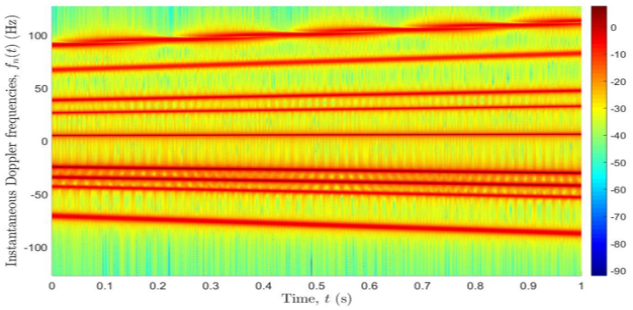

(a)

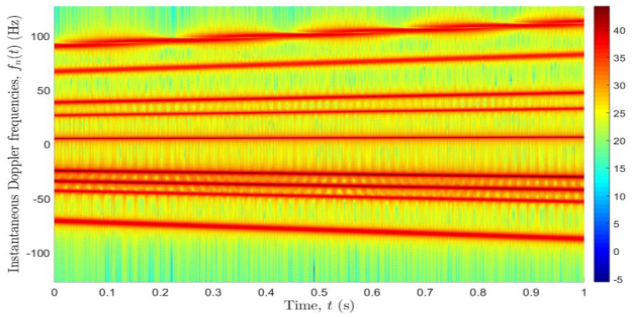

(b)

Fig. 16: (a) Spectrogram $S_{xx}(f,t)$, and (b) average spectrogram of process $\mu(t)$ for $N = 10$, optimal window size of $T = 1.2$ s and the scatterers are randomly located inside a rectangle.

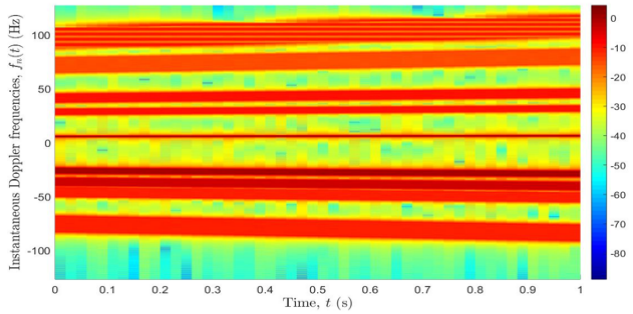

(a)

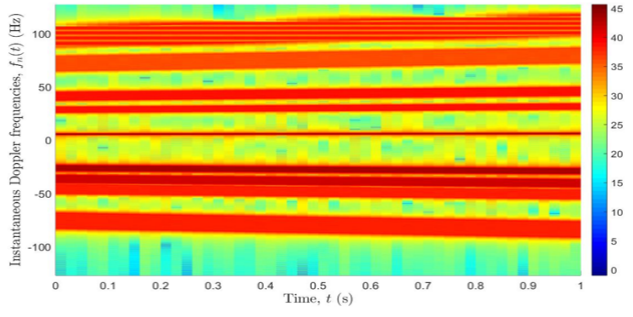

(b)

Fig. 17: (a) Spectrogram $S_{xx}(f,t)$, and (b) average spectrogram of process $\mu(t)$ for $N = 10$, window size of $T = 5$ s and the scatterers are randomly located inside a rectangle.

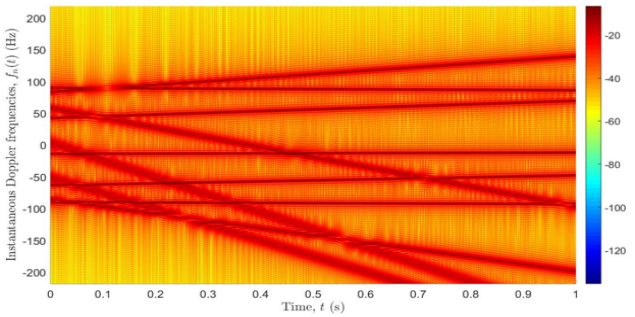

(a)

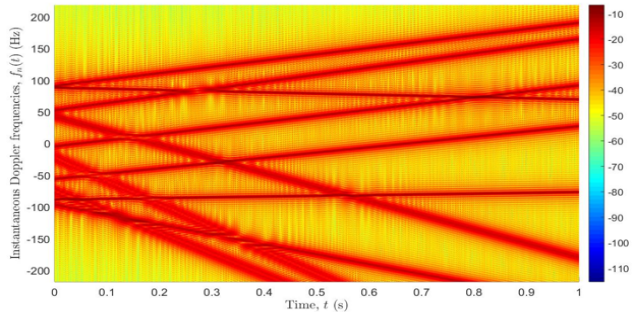

(b)

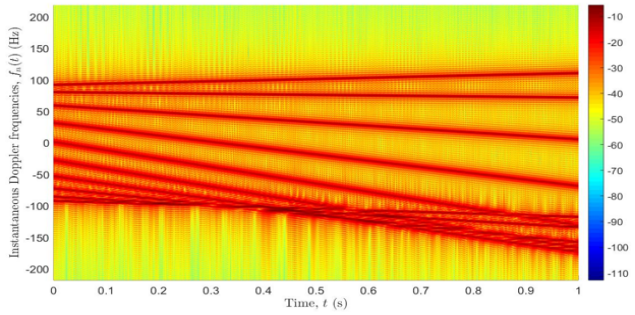

(c)

Fig. 18: (a) Spectrogram $S_{xx}(f,t)$ for Path I, (b) Spectrogram $S_{xx}(f,t)$ for Path II, and (c) Spectrogram $S_{xx}(f,t)$ for Path III.

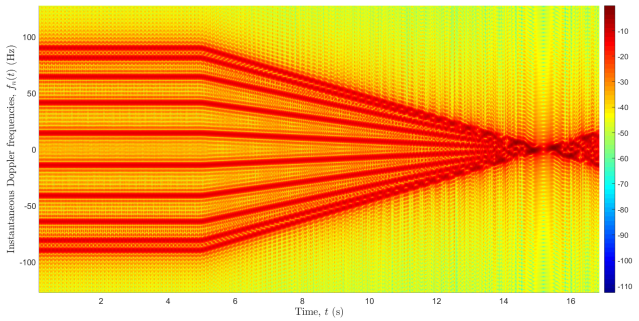

Fig. 19: Spectrogram $S_{xx}(f,t)$ of process $\mu(t)$ when the brakes are applied at a constant speed.

have considered the average spectrogram of 100 rounds with random phases. Figure 20 shows the graph of the resulting time variant average Doppler shift of the reference and simulation model as described in (21) and (23), respectively. Analogously, Fig. 21 illustrates the time-variant average Doppler spread of reference and simulation model.

We note from the inspection of Fig. 20 and 21 that our theoretical models line up sufficiently with the simulation results. Again, good agreement between the approximation and simulation results is observed for Path III. However, contrary to expectations, mismatches are observed at some points between the reference model and the simulation results for Path I and II.

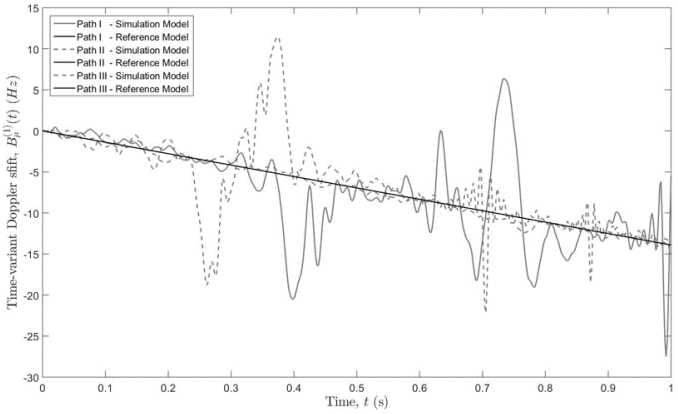

Fig. 20: Time-variant average Doppler shift $B_f^{(1)}(t)$ for process $\mu(t)$ obtained by the reference model and the simulation model.

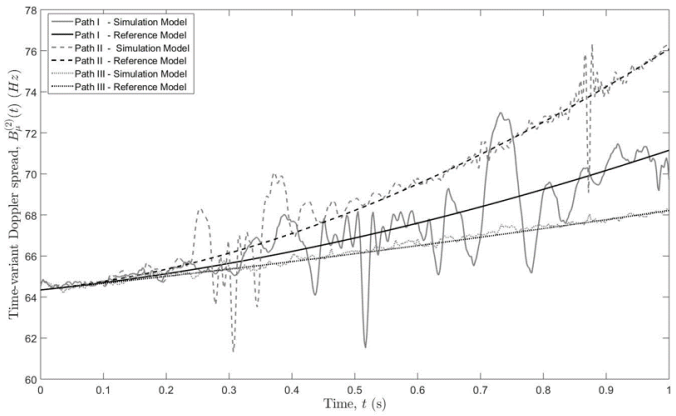

Fig. 21: Time-variant average Doppler spread $B_f^{(2)}(t)$ for process $\mu(t)$ obtained by the reference model and the simulation model.

VI. Conclusion

In this paper, I have studied the effect on non-stationary mobile-to-base station channels under variations of the mobile velocity. It has been demonstrated that the effect of the mobile velocity variations results in a non-stationary multipath channel. Time-varying spectral information has been analysed for different scenarios using the spectrogram. The analysis was extended to observe the changes in the spectrogram with different types of window functions and window lengths. Further, it is demonstrated that the spectrogram can be improved by taking the average over the phases and selecting an optimal window length. The average spectrogram implies the use of multiple antennas to reduce unwanted frequency interferences.

I have also investigated and plotted the spectrogram for a new scenario in which a moving vehicle brakes when at a constant speed. There, we observed a considerable Doppler shift caused by the sudden deceleration of the vehicle.

Further, it is shown that the reference model of time-variant average Doppler shift and time-variant average Doppler spread, is realisable by the simulation model. Hence, we identified that the window length is a decisive factor to improve the agreement between the reference model and the simulation model.

This study can be extended by incorporating a mobile-to-mobile time-variant channel model. Furthermore, a new research topic could be to optimise the window length such that the time-variant average Doppler shift, computed by taking the sum of all power-weighted Doppler shifts normalised to the total received power of the multipath components, equals the Doppler shift computed from the spectrogram.

Acknowledgement

The author would like to thank Prof. Matthias Pätzold of the University of Agder, who in spite of being extraordinarily busy with his duties, took time out to hear, guide and keep the research work on the correct direction.

Special thank to Mrs. Katharina Pätzold and Mr. Meisam Naderi, for taking time to help on coding and drafting the report using Latex and Matlab software.

References

[1] A. Paier, J. Karedal, N. Czink, C. Dumard, T. Zemen, F. Tufvesson, A. Molisch and C. Mecklenbräuker, "Characterization of Vehicle-to-Vehicle radio channels from measurements at 5.2 GHz", *Wireless Personal Communications*, vol. 50, no. 1, pp. 19-32, 2008.

[2] A. Borhani and M. Pätzold, "A novel non-stationary channel model utilizing Brownian random paths", *REV Journal on Electronics and Communications*, vol. 4, no. 1-2, 2014.

[3] M. Pätzold and A. Borhani, "A non-stationary multipath fading channel model incorporating the effect of velocity variations of the mobile station," *2014 IEEE Wireless Communications and Networking Conference (WCNC), Istanbul*, 2014, pp. 182-187.

[4] R. Iqbal and TD. Abhayapala. "Impact of mobile acceleration on the statistics of Rayleigh fading channel." *Proc. 8th Australian Communication Theory Workshop, AusCTW*, 2007.

[5] F. J. Harris, "On the use of windows for harmonic analysis with the discrete Fourier transform," *in Proceedings of the IEEE*, vol. 66, no. 1, pp. 51-83, Jan. 1978.

[6] L. Stankovic, "Auto-term representation by the reduced interference distributions: a procedure for kernel design," *in IEEE Transactions on Signal Processing*, vol.44, no. 6, pp. 1557-1563, Jun 1996.

[7] Q. Yin, L. Shen, M. Lu, X. Wang and Z. Liu, "Selection of optimal window size using STFT for quantitative SNR analysis of LFM signal," *Journal of Systems Engineering and Electronics*, vol. 24, no. 1, pp. 26-35, Feb. 2013.

[8] M. Pätzold, Mobile Radio Channels, 2nd ed. Chichester, West Sussex, U.K.: Wiley, 2012, pp. 62-65,439-440.

[9] M. Pätzold, B. O. Hogstad and N. Youssef, "Modelling, analysis, and simulation of MIMO mobile-to-mobile fading channels," *in IEEE Transactions on Wireless Communications*, vol. 7, no. 2, pp. 510-520, February 2008.